"ACOUSTIC PARAMAGNETIC RESONANCE SPECTRA OF Cr^{2+} IN MgO AND CaO"

by Ian John Shellard BSc

Thesis submitted to the University of Nottingham

for the degree of Doctor of Philosophy

November 1978.

CONTENTS

LIST OF FIGURES

APPENDIX B

AB 1 Current Voltage characteristic for a typical p-n junction. (schematic).

AB 2 Schematic representation of an operating IMPATT diode.

AB 3 (a) Voltage across an operating IMPATT diode.

(b) Build up of charge across the avalance region of an operating IMPATT diode.

(c) Current induced in an electrical circuit to which an IMPATT diode is connected.

AB 4 Schematic circuit representation of the IMPATT diode as an oscillator and its external circuit.

AB 5 Hewlett-Packard pulse amplifier circuit.

AB 6 Hewlett-Packard bias adder.

AB 7 Pulse amplifier circuit used in experiments.

AB 8 Waveguide bench used for IMPATT tests (schematic).

AB 9 Pulse amplifier circuit provided by Dr P Braddock, RSRE.

PLATE 1 : General view of apparatus

PLATE 2 : Cavity used in applied stress cryostat.

PLATE 3 : Polishing ring with glass feet and sample in place.

(All plates included in chapter 3)

ABSTRACT

The Acoustic Paramagnetic Resonance (APR) of the chromous ion in two cubic host lattices, MgO and CaO, has been investigated for phonons of frequency around 9.5 GHz and temperatures in the range 1.5K to 4.2K. An iron-cored electromagnet produced magnetic fields continuously variable from 0 to 2 Tesla, the direction of magnetic field could be varied through 90° in the same plane as the phonon direction. Experiments were performed in which a variable uniaxial stress could be applied to a crystal of Cr^{2+} in MgO, giving information about the effects of local lattice strain on the APR spectrum. A change in the g-value of one resonance line with applied stress was observed, and, from this, the value of the strain coupling constant could be obtained. The experimental results enabled values for the parameters 3Γ (Jahn-Teller tunnelling splitting) and K (spin-orbit splitting) to be obtained, which were compared with those obtained by other methods. Further experiments were performed on Cr^{2+} in CaO in which the direction of the applied magnetic field could be changed by rotating the sample crystal about the phonon direction, enabling the field to be aligned with the crystal <111> direction. The theoretical prediction (Fletcher (1971)) that strain broadening of the resonance lines should be reduced under these conditions was demonstrated. Experiments were performed at two separate frequencies and two separate temperatures, and the results used as data for a computer programme which gave the values of the various parameters of the system, and thus allowed a low-lying energy level diagram to be predicted. There were similarities between this diagram and the accepted energy-level diagram of Cr^{2+} in MgO, as would be expected. The differences were attributed to the difference in the lattice constants of the host materials.

ACKNOWLEDGEMENTS

I would like to thank the many people whose help and encouragement have made the publication of this thesis possible. In particular, thanks are due to:-

Professor E R Andrew, Dean of the Faculty of Pure Science and former Head of the Department of Physics and Professor K W H Stevens, Head of the Department of Physics for the use of the departmental facilities.

Dr V W Rampton for his supervision, advice and moral support.

Dr C A Bates, Dr J R Fletcher, Mr R Wardlow and Miss C Maynard for the great help they have given me with the theoretical aspects of the work, and Dr P J King and Dr A A Ghazi for the many useful discussions on the experimental side.

Mr K Williams, Mr P Webster and their workshop staff, especially Mr D Kerr, for their assistance.

Mr W B Roys for much experimental advice.

Miss J Morris who prepared the typescript.

The S.R.C for the provision of a maintenance grant throughout the three years during which the experiments were performed.

CHAPTER ONE

INTRODUCTION AND REVIEW

1.1 Introduction

Since the early 1960's, Acoustic Paramagnetic Resonance (APR) Techniques have been used to investigate the low-lying energy levels of a number of paramagnetic impurities in crystalline hosts. The excitation mechanism employed in this technique is that of modulating the electric potential of the surrounding crystalline field at the electrons of the paramagnetic ion by means of a coherent, monochromatic microwave frequency acoustic wave. This modulation couples directly to the orbital angular momentum of the electron which in turn couples to the spin magnetic moment by means of spin-orbit coupling. As a result excitation by resonant absorbtion from the acoustic wave can be considered as taking place, provided the lifetime of the excited state is long when compared to the period of the exciting wave. Such a process can yield information about both the low-lying energy levels of the paramagnetic ion and the spin-phonon interaction. Comparisons may be drawn between results obtained by thermal spin-lattice relaxation measurements, and in fact, the method of excitation employed in APR is the exact converse of the direct spin-phonon relaxation process. The essential difference between APR and many of the other phonon investigation techniques in common use, such as thermal conductivity or specific heat measurements, is that these methods generally make use of the natural thermal phonons of the lattice, which are necessarily of broad-band frequency spectrum and are incoherent, whereas APR (in common with some other modern phonon spectroscopic techniques) makes use of externally generated, coherent, monochromatic phonons which are injected into the lattice. The shortening of the mean free

path of these phonons by interaction with the natural thermal phonons of the lattice is reduced by the use of low temperature techniques. A discussion of the methods of generation of phonons in use today is included in section I (2). Many experimental similarities exist between the techniques of APR and electron paramagnetic resonance (EPR). The method of excitation of the spin-system is, however, completely different. Whilst APR employs the modulation of the crystal field, and indirect coupling to the spin system, EPR employs an electromagnetic wave as an exciting energy, the magnetic vectors of which couple directly to the magnetic moments of the spins. This important difference has far-reaching implications into the information available from each technique: A Kramer's Ion, with an unpaired electron, introduced into a crystal lattice will not usually couple strongly to the lattice, whilst a non-Kramer's Ion, which has all its electrons paired, is usually much more strongly coupled. Since the excitation process of APR depends upon the interaction between the lattice and the orbital angular momentum of the ion, APR resonances will usually be observed for non-Kramer's Ions, whilst the inhomogenous broadening of EPR lines caused by the splitting of levels as a result of random lattice strains may make EPR techniques difficult to use. Conversely, an ion which is not strongly coupled to the lattice will not exhibit APR, but may be observable by EPR. In addition to this, large lattice strains (distortions) may cause splittings of the $\Delta Ms = \pm 1$ levels greater than the quantum energies available from conventional electromagnetic generators. APR techniques can sometimes be used in this situation to observe the $\Delta Ms = \pm 2$ transitions, which are of low probability for electromagnetically excited changes in the spin system. An obvious application of this difference between the techniques is that the same ion in the same lattice but in a different valence state may be readily observable

by one method but not by the other. Useful information can, therefore, be obtained by a comparison of the results of investigation of the same specimen by both EPR and APR. Ions which exhibit a degenerate ground state are likely to be more strongly coupled to the lattice than those of singlet ground states, and may also exhibit Jahn-Teller distortions, causing a lifting of the ground state degeneracy and a lowering of the overall system energy. Both the systems investigated during the course of this thesis, Cr^{2+} in MgO and Cr^{2+}in CaO are non-Kramers ions, exhibiting strong coupling to the lattice and undergoing a dynamic Jahn-Teller effect.

The method most commonly used for APR and used during these investigations, is the conventional pulse echo system, employing phonons of frequency around 10^{10} Hz, i.e. X-band microwave frequencies. The reasons for this choice are:

1. The apparatus necessary to build such a spectrometer is readily available, being used also for X-band ESR investigations;
2. The pulsing technique has the advantage over continuous wave experiments that higher phonon powers are available from low consumption generators, giving better signal to noise ratios. Modern detection techniques can provide continuous monitoring of the echo height, removing the advantage of [illegible] which existed in the past.
3. The magnetic fields necessary to split low-lying levels by the amounts necessary for resonant absorption at these phonon energies are relatively low (~2T), such that conventional electromagnets, or small superconducting magnets, can be used.
4. The degree of sample preparation required is readily obtainable using commercial optical preparation equipment.

5. The transducers used to produce the phonons are readily available commercially, and have many advantages over other generation techniques, discussed in section 1.2.

There are, however, a number of drawbacks to this method of investigation:

1. Samples are necessarily large, homogeneous, single crystals, mechanically strong enough to permit preparation processes without damage.

2. The quanta available are small by comparison with those produced by thermal conductivity and specific heat measurements.

3. There is a large power loss in the transducer stage. Acoustic power in the transducer is about an order of 10^4 down on incident power on generation, and a similar reduction in power occurs on detection. This effect is worsened by the difficulty encountered in producing a good, acoustically transparent, bond between the transducer and the sample.

Modern methods of phonon generation have enabled frequencies well above 10^{10} Hz to be obtained. These are discussed in section 1.2, along with their disadvantages when considered in connection with conventional APR techniques. Any increase in frequency obtainable from the present method, (frequencies of 10^{13} Hz were obtained by Weis (1976)) have to be considered in relation to the increased difficulties of sample preparation, and the larger magnetic fields required for resonant absorption to take place.

1.2 Generation of Microwave Ultrasound

1.2 (i) Introduction

In this section a brief review of the more common methods of phonon generation is given and their relative merits discussed.

A major reason for the confinement of APR, as a practicable technique, to the last twenty years has been the difficulty of obtaining phonons of sufficiently high powers in the microwave frequency range. A number of techniques have been tried to overcome this problem, some relevant only to specific experimental situations, others of a more general nature. In the work described in this thesis, the phonons were produced by means of the piezoelectric effect at the end face of an X-cut quartz rod placed in the high electric field region of a resonant microwave cavity. There were two important experimental criteria governing the choice of this system, over and above the advantages explained in section 1.2 (vi), below, these being:

(i) In the case of the work done on Cr^{2+} in MgO, a static uniaxial, stress was applied to the sample by means of a system of levers. The use of a quartz rod transducer bonded to the sample allows the pressure system to be sited away from the waveguide, facilitating the design, construction and use of the cryostat.

(ii) Both the systems investigated during the course of this research contain traces of Cr^{3+} and other paramagnetic ions exhibiting strong ESR absorption at X-band frequencies. The use of a quartz rod enables the sample to be maintained away from the cavity, ensuring no ESR absorptions take place.

1.2 (ii) Resonant Plate Generation

This is the oldest method of high frequency sound generation, usually employing a thin plate of quartz, place between a pair of

flat, parallel electrodes driven by an A.C generator. The system is straight forward to construct, and good powers can be obtained from the fundamental mode of vibration of the plate up to a frequency of about 10^8 Hz. Systems of this type are in wide use for generation in the 10MHz→100MHz region. Attempts have been made to extend the frequency range obtainable from this method into the GHz region. Two main systems have been employed:

Ringo (1947) and Sokolov (1950) were able to generate frequencies in excess of 1GHz by means of a quartz plate of thickness 3.8×10^{-4}m. Plates of this thickness are difficult to make and very fragile in operation, so their use is not general.

Slater (1946) proposed that it would be possible to reach higher frequencies by putting the quartz plate over the end of a resonant microwave cavity driven at the required frequency. This would allow higher driving powers to be used at GHz frequencies. The system was tested by Stewart and Stewart (1963), utilising a higher harmonic of a less thin resonant plate, and detecting the resonance by the resultant change in the Q-factor of the cavity. The disadvantage of such a method is that the power conversion of electromagnetic energy into ultrasound in the higher harmonic modes is very low compared with that of the fundamental. Nevertheless, a frequency of 10GHz was obtained.

1.2 (iii) Evaporated Piezoelectric Films

By special evaporating conditions, a thin film of Cadmium Sulphide can be grown onto the end face of a sample, such that the C-axis of the CdS crystals is perpendicular to the end face of the sample. A transducer grown in this way has several advantages over both the resonating quartz plate and non-resonant rod methods: Firstly, the necessity to form a good acoustic bond between the sample and the generator is overcome during the evaporation process, removing the experimental problems inherant

in mechanically bonding these systems, and secondly a more efficient transfer of energy is obtained, single layer films giving double the efficiency of a quartz transducer. This situation can be further improved by the use of double layers separated by layers of silicon, all layers of thickness $\lambda/2$. Attempts have been made to use piezoelectric semiconductor p-n junctions evaporated onto the sample end face, giving the advantage that, since the depletion layer thickness is dependent on the bias voltage, the system can be electrically tuned onto resonance.

1.2 (iv) Magnetostrictive Generation

A thin film of a ferromagnetic metal is grown onto the polished end face of the sample, and this film is placedin the high magnetic field region of a microwave resonant cavity. An external steady magnetic field is applied such that, by choice of angle between the field and the film, either transverse or longitudinal phonons can be generated by magnetostrictive coupling of the resulting spin waves. The advantage of obtaining both longitudinal and transverse phonons is offset by the large external fields necessary to obtain frequencies in the regions of 10^{n} GHz. Nevertheless, the method has been successfully used at 1GHz by Bommel and Dransfeld (1959) and more widely at lower frequencies.

The efficiency of generation of this method is only fractionally better than 10^{-4}, and thus no real advantages over piezoelectric generation can be obtained in this area.

1.2 (v) Superconducting Tunnel Junctions

The use of superconducting tunnel junctions is the most recent generation system, and makes possible variable frequency phonon spectroscopy, which is rapidly growing in both power and extent as

a research tool. Onto each end of a polished specimen is evaporated a junction of a metal "sandwiching" an oxide layer. The metal is chosen such that it goes superconducting in the laboratory range of temperatures. At the time of writing, the method was still in any an early state, and various authors prefer to use various different types of metal for the junction. Those in common use are tin/tin oxide/tin, and aluminium/aluminium oxide (King et al, Kinder), and lead/bismuth. Similarly the conditions of evaporation and junction profiles for best generation or detection are by no means fixed, and many experimental parameters that can be varied during growth processes are under investigation. The advantages of this system over other methods are many: Firstly variable frequency spectroscopy is carried out over a wide range of energies, passing 100 cm^{-1}. The frequencies that can be generated in this way are of order 10^{13}Hz, far beyond those obtainable using conventional piezoelectric systems. The degree of sample preparation necessary is lower than that of the transmission/echo system, since the use of separate generation and detectors on opposite ends of the sample removes the need to polish the end faces parallel (the finish of surfaces is, however, a more serious problem that with conventional samples). The disadvantages of the system are that no static external magnetic fields above the critical field of the superconducting films can be used, since generation will cease. Thus no experiments involving Zeeman-split levels are possible. At the present time, the degree of reproducibility of junction production is low, because of the high number of parameters to be considered during growth, making prolonged spectroscopic research more difficult. Furthermore both very low temperatures (in the region of 800 mK) and high cooling powers are required to both drive the junctions superconducting,

and to overcome the incident heating powers, heat leaks and so on, necessitating the use of extensive pumping apparatus. Despite these problems this author is confident that this method of phonon generation/detection will increase in importance as the experimental difficulties are overcome, and will rapidly become one of the most widespread research tools in use in solid state physics.

1.2 (vi) Non-Resonant Quartz Rods

Although this method relies on piezoelectric generation, it has been left to last because of its importance to this thesis: all experiments reported here made use of phonons generated by this method. Despite certain advantages of the thin film and resonant plate methods of piezoelectric generations, the rod system continues in widespread use. One of the major reasons for this is that one transducer treated with care, may be used for a large number of experiments before decay of the surface polish limits the usefulness. The rods are available commercially prepared to optical standards, and, despite their expense, can be used in a wide range of experiments and with a wide range of samples. In addition to this, the rod system was necessarily used for these experiments for the reasons discussed in section 1.2 (i) above.

Baranski (1958) used a block of polished quartz of thickness 1.5cm situated in a re-entrant cavity to generate phonons of frequency 2GHz. Later experiments showed that the phonons were generated at the end faces of the block. Bommel and Dransfeld extended this work; firstly with a 9mm quartz cube with all 6 faces optically polished, producing phonons of frequency 2GHz, of either longitudinal or transverse type depending on which face of the cube was placed into the high electric field region of the cavity (1958); and , secondly, by using a cylindrical quartz rod, with both end faces

polished, in conjunction with a two cavity system, to generate phonons of frequency 4GHz. Jacobsen (1959) used a similar two-cavity system to obtain phonons at a frequency approaching 10GHz. The cavity design utilised by Jacobsen in this experiment is now in general use. In this Department, Rowell and Rampton (1963) made use of a single cavity, of similar design to the Jacobsen cavity, in pulse echo type experiments. This same cavity design, with only minor modifications, has been employed in the experiments reported here, and in the work of Rampton (1965). Marshall (1967), Brabin-Smith (1969) and Atkinson (1976). The limits of frequency obtainable from this type of system are determined by two factors:

(a) The relative dimensions of cavity and rod: The standard diameter of rods used for these experiments is 2.9mm. To produce rods of significantly smaller diameter is a difficult technical process, yet a single order of magnitude increase in the frequency (~ 100GHz) will require a cavity which is completely filled by the rod (Jacobsen and Ilukor, 1966).

(b) The end face flatness and parallelism necessary for good echos is a function of the frequency. The flatness of the end face must be of the order of the phonon wavelength. For a quartz rod and a 10GHz phonon this flatness is of order 5000 Å, thus standard optical polishing techniques and the use of optical flat for reference is adequate. At 100GHz, however, the wave-length is reduced to 500Å, making the polishing process far more complex.

It would seem, therefore, that the advantages of this technique lies on its versatility and comparative simplicity when used in experiments up to and aroung 10GHz. At higher frequencies, however, the technique is more difficult to employ, and alternative systems have to be sought for.

1.2 (vii) Summary

Each of the techniques outlined previously present certain advantages to the experimentor when used in a suitable experiment. In this work a non-resonant quartz rod of length 12mm and diameter 2.8mm with end faces optically polished flat and parallel was used to produce phonons of frequency ∿10GHz, in a pulse-echo type of experiment, for the reasons explained in sections 1.2 (i) and 1.2 (vii) above.

CHAPTER TWO

THE JAHN-TELLER EFFECT

2.1 Introduction

The interpretation of the results presented in chapters 4 and 5 of this thesis requires that the Jahn-Teller effect be taken into account. A brief description of this effect is thus given here. The theory sections of chapters 4 and 5 carry on from this chapter in applying the effect to the particular system under discussion. The description given here is based on that of Ham (1967), since section 4.3. discusses Ham's interpretation of the APR of Cr^{2+} in MgO in detail. Reference was made to the review of Bates (1978).

No discussion of crystal field (ligand) theory is included as the application of this to APR is discussed in the theses of Marshall (1967) and Brabin-Smith (1969).

2.2 The Static Jahn-Teller effect

For an ion to undergo a Jahn-Teller effect it must be in an electronic state which has orbital degeneracy in a crystalline field of high symmetry. The static Jahn-Teller effect may be described as a distortion of the crystalline environment to produce a lower symmetry than that of the original environment. The degeneracy is also lifted. The basic Jahn-Teller theorem was proven by Jahn and Teller in 1937 and may be stated:

"If a molecule or a crystalline defect has orbital electronic degeneracy when the nucleii are in a symmetrical configuration, then the molecule or defect is unstable with respect to at least one asymmetric displacement which lifts the degeneracy." (Ham 1967).

Suppose a degenerate orbital state in a symmetric environment has an energy Eo, then, according to the Jahn-Teller theory, there exists

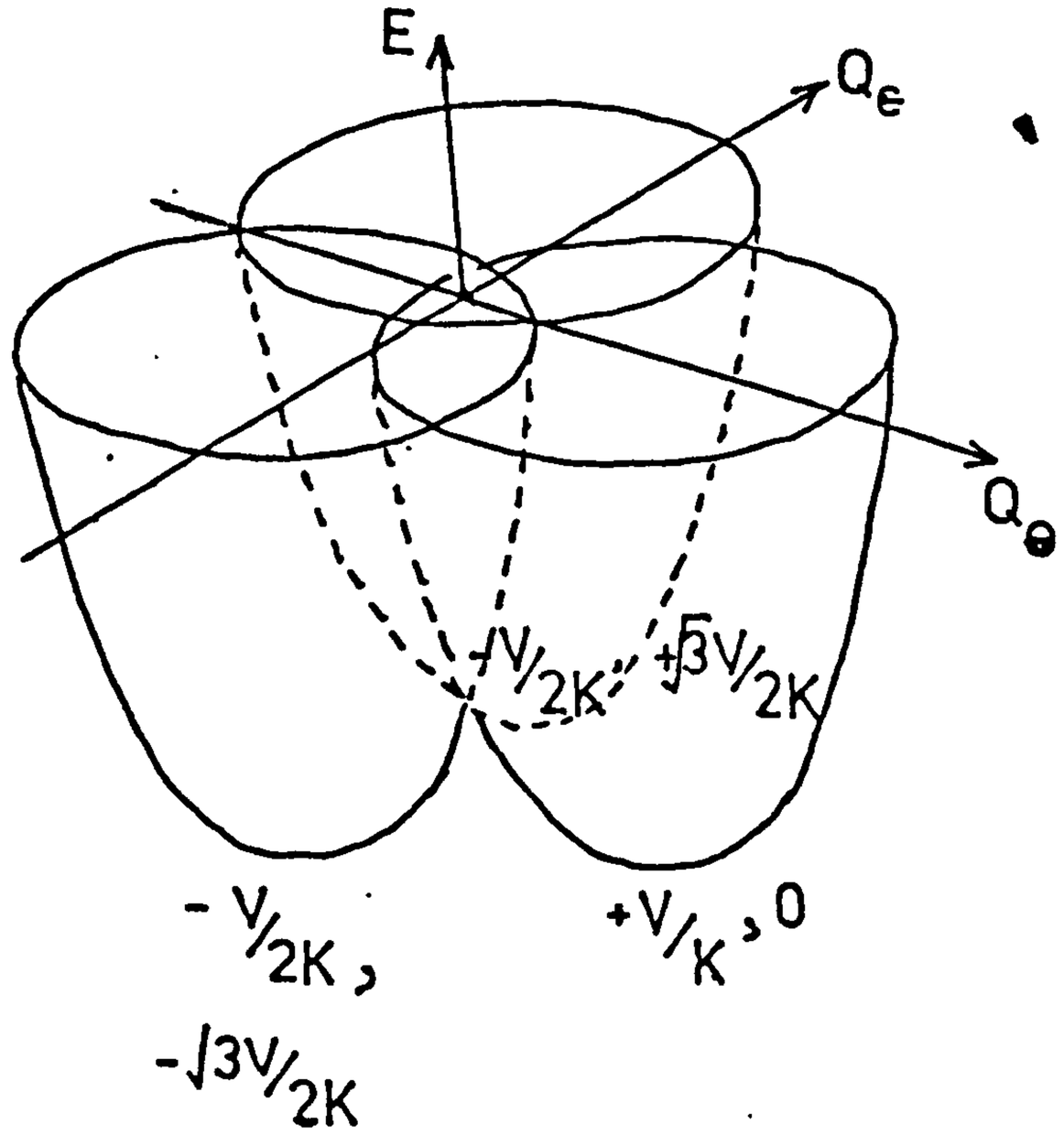

FIG.2.2.(ii). Energy surfaces of the electronic eigenstates of a Γ_4 triplet orbital state as a function of the static distortion modes Q_θ and Q_ϵ.

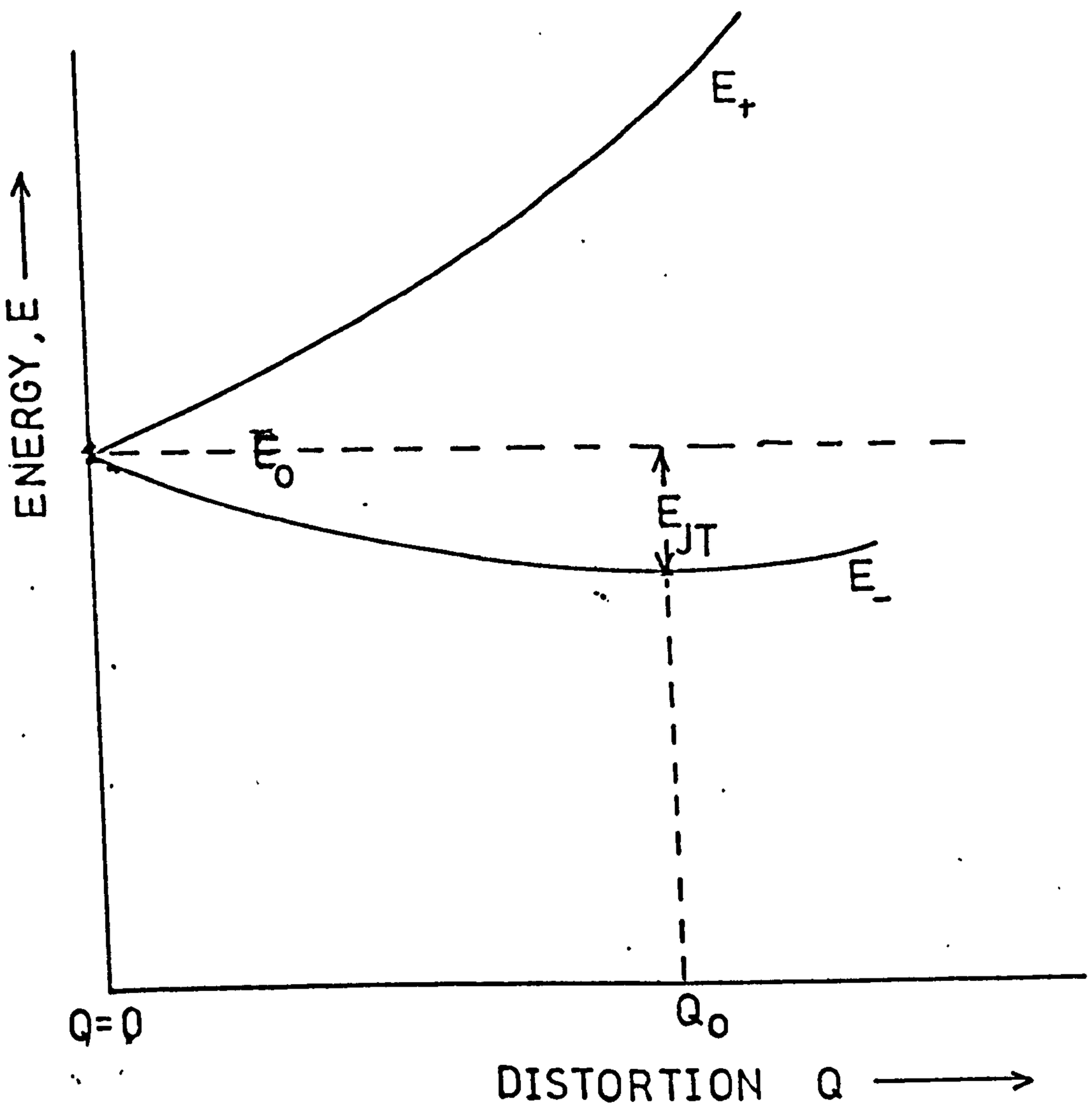

FIG 2.2.(i). Distortion lifting of the degeneracy of an electronic state (1st order).

at least one distortion which will lift the degeneracy in such a way that the lowest split state has an energy E_-, less that Eo. The elastic energy associated with a pure distortion, Q, is proportional to Q^2, hence some value of Q will be attained at which the difference $(Eo - E_-)$ is a maximum. Let us call this point Qo, and $(Eo - E_-)$ is then called E_{JT} the Jahn-Teller stabilisation energy. The new configuration made up of the original symmetry plus the distortion Qo is a stable state. (Figure 2.2. (i)). It should be noted that other stable states may be obtained for different distortions, Qo', or for negative Q, and hence the stable state defined by Qo may be unstable with respect to these other states of equilibrium.

The example of a triplet level Γ_4 in an environment which exhibits cubic symmetry is considered, (similar to the problem of Cr^{2+} in MgO). The three associated wavefunctions ψ_{11}, ψ_2, ψ_3 are identified by Ham (1967) as x, y, and z. The Hamiltonian of the system is:

$$\mathcal{H} = E_0 U + V(\varepsilon_\theta Q_\theta + \varepsilon_\epsilon Q_\epsilon) + \frac{K}{2}(Q_\theta^2 + Q_\epsilon^2)U \quad \ldots\ldots 2.2.1.$$

where U is the unit operator

V is the strain (or Jahn-Teller) coupling constant

K is the Kinetic energy constant.

$K/_2\ (Q\theta^2 + Q^2\varepsilon)$ is the elastic energy term.

$E\theta$ and $E\varepsilon$ are matrices which are diagonal with respect to ψ_1, ψ_2, ψ_3 ... eigenstates of $\mathcal{H}$. The energies of the eigenstates are given by:

$$\left.\begin{aligned} E_1 &= E_0 + V(\tfrac{1}{2}Q_\theta - \tfrac{\sqrt{3}}{2}Q_\epsilon) + \tfrac{1}{2}K(Q_\theta^2 + Q_\epsilon^2) \\ E_2 &= E_0 + V(\tfrac{1}{2}Q_\theta + \tfrac{\sqrt{3}}{2}Q_\epsilon) + \tfrac{1}{2}K(Q_\theta^2 + Q_\epsilon^2) \\ E_3 &= E_0 - VQ_\theta + \tfrac{K}{2}(Q_\theta^2 + Q_\epsilon^2) \end{aligned}\right\} \quad \ldots\ldots 2.2.2.$$

The representations of E_1, E_2, E_3 as energy surfaces in Q-space are three paraboloids (corresponding to ψ_1, ψ_2, ψ_3) with vertices given by

ψ	Q_θ	Q_ϵ
1	$-V/2K$	$\sqrt{3}V/2K$
2	$-V/2K$	$-\sqrt{3}V/2K$
3	V/K	0

These points define three distortions giving positions of stable equilibrium for this system. Substituting from these values into the equations 2.2.2. gives the energy difference, E_{JT}.

$$E_{JT} = V^2/2K \qquad 2.2.3$$

The forms of the distortions $Q\theta$ and $Q\epsilon$, and the wavefunctions ψ_1, ψ_2, ψ_3, as defined by Ham (1967), show that the positions of stable equilibrium correspond to tetragonal distortions along the $x(\psi_1)$, $y(\psi_2)$ and $z(\psi_3)$ axes. (The nature of the distortion, compression or elongation, is determined by the sign of V). The original state ($Q\theta = Q\epsilon = 0$) is unstable with respect to any of the distorted states of Figure 2.2 (ii) as a result of the degeneracy of the triplet in the cubic lattice and of the linear dependence of the splitting of the triplet on $Q\theta$ and $Q\epsilon$.

There are three stable positions, corresponding to ψ_1, ψ_2, ψ_3, each with no remaining orbital degeneracy and which are all equivalent.

It would be expected, then, that each impurity complex in the lattice would spontaneously distort to one or another of these stable positions, and remain there. The choice of equilibrium position (in the absence of any constraint) would be random.

2.3 The Dynamic Jahn-Teller Effect

In the above discussion, it was assumed that the distortions, Q, were a fixed parameter of the system, which did not vary. In most cases, however, this is not so. The lattice ions have a kinetic behaviour resulting from their interaction with the Q's, and thus the coupling between the Q's and the electrons must be considered for a general case. Such a combination is described by a vibronic (vibrational and electronic) Hamiltonian. The example used in section 2.2, that of a Γ_4 triplet in a cubic host lattice, is also considered in this section. The distortions, $Q\theta$, $Q\varepsilon$, must now be considered as distortion modes of the lattice. Although, in the general case, the coupling of the ion to the complete spectrum of phonon modes should be considered, it is usual to consider only one pair of modes (here $Q\theta$, $Q\varepsilon$) which are assumed to be normal modes of the ligand cluster, described by a well-defined angular frequency w. Momentum operators $P\theta$, $P\varepsilon$, associated with $Q\theta$, $Q\varepsilon$ can be defined, and a kinetic energy operator for the modes $\frac{1}{2\mu}(P^2\theta + P^2\varepsilon)$ obtained. μ is the effective mass of the modes, and hence K in equation 2.2.1 may be replaced by μw^2. The resulting vibronic Hamiltonian is then

$$\mathcal{H}_{vib} = EoU + V\{EoQ\theta + E\varepsilon Q\varepsilon\} + \frac{1}{2\mu}\{P\theta^2 + P\varepsilon^2 + \mu w^2(Q\theta^2 + Q\varepsilon^2)\}U \quad \ldots . \; 2.3.1$$

The eigenstates of 2.3.1 give the energy levels of the coupled (vibronic) system.

The matrices $E\theta$ and $E\varepsilon$ are diagonal with respect to the wave-

functions ψ_1, ψ_2, ψ_3, as noted in section 2.2, and hence $\mathcal{H}_{vib}$ does not couple these states. An exact solution can thus be obtained for each of the states ψ_1, ψ_2, ψ_3, separately. Such a solution will be a vibronic eigenstate, Ψ, which may be considered as a product of one ψ state with a vibrational function, Φ, depending on $Q\theta$, $Q\varepsilon$ and the chosen ψ.

i.e. $\Psi_1 = \psi_1 \Phi_1$ etc.

The solution show that the Φs are simple two-dimensional harmonic oscillator functions in the energy wells of Figure 2.2 (ii). The energy levels of $\mathcal{H}_{vib}$ are thus

$$E_{i(n)} = Eo - (V^2/2\mu\omega^2) + (n\theta + n\varepsilon + 1)\hbar\omega$$

where i = 1, 2, 3 relating to ψ_1, ψ_2, ψ_3,

n = o or a positive integer.

It follows that E is independent of i, i.e. the energy is the same for each wavefunction ψ.

The ground state energy is given by the case $n\theta = n\varepsilon = o$,

i.e. $E_{i(o)} = Eo - (V^2/2\mu\omega^2)$

This is threefold degenerate as E(o) is independent of which ψ is chosen, and is made up of the lowest state in each of the three wells of Figure 2.2 (ii). By obtaining the exact wavefunctions of the vibronic ground states, Ham is able to show that these solutions are mutually orthogonal, and that they transform as the group Γ_4 of the cube that ψ_1, ψ_2, ψ_3, belong to in the absence of a Jahn-Teller effect. Hence the degeneracy of the vibronic ground-state of $\mathcal{H}_{vib}$ is exactly that of the original symmetric system. Ham also shows that, if the Jahn-Teller coupling coefficient V is zero (i.e. no Jahn-Teller effect) the solutions reduce to those of the non-Jahn-Teller system. The implication of this result is that the change from a non-Jahn-Teller to a Jahn-Teller system is not spontaneous and discreet, as suggested

by the analysis of section 2.2., but continuous. This may be interpreted by considering the vibrational functions Φ as having a finite spread in Q-space, so that the solutions Ψ_1 Ψ_2 , and Ψ_3 of equation 2.3.1 may overlap. Another way of expressing this overlap is to consider that a single complex may spontaneously move from one solution Ψ to another, whereas in the case of the static Jahn-Teller effect each complex exhibited one distortion only, although the choice of (energetically equivalent) distortion was random. Hence, the degeneracy of the original electronic state is not lifted, but the vibronic solutions may be distinguished by the fact that a different vibrational function Φ is associated with each electronic wavefunction ψ.

CHAPTER 3

APPARATUS

3.1 Introduction

See Figure 3.1(i)

The spectrometer used was a conventional pulse-echo type X-band APR unit. The machine varied little from that used originially in this department by Rampton (1965) and in detail only from that used by Brabin-Smith (1969). The reader is referred to the Thesis of Brabin-Smith (1969) for further details of the apparatus.

3.2 Preparation of Samples

3.2(i) MgO

Samples of chromium-doped MgO were prepared from single crystals provided by Professor L J Challis, grown by Mr J H Burrows of Bristol University in 1965. The samples were pale green coloured in the as received state.

3.2(ii) Alignment and Grinding

The crystals were aligned by X-ray diffraction. They were mounted on a goniometer giving three degrees of freedom and then placed into an X-ray diffractometer using copper K_α X-rays at about 35KV. Using the low-geared goniometer controls and a sensitive scintillation counter detector, alignment along the <100>, <010>, and <001> directions to better than 1^o was easily possible. The goniometer could be locked in position and then firmly mounted on the magnetic bed-plate chuck of an accurate surface grinder, enabling surfaces to be prepared accurately parallel to the required directions.

3.2(iii) Polishing

It was necessary for the samples to have an end parallelism of better that 1′ of an arc, and flatness over the end surface of better than 5000 Å for good echos to be obtained at 10GHz. These conditions

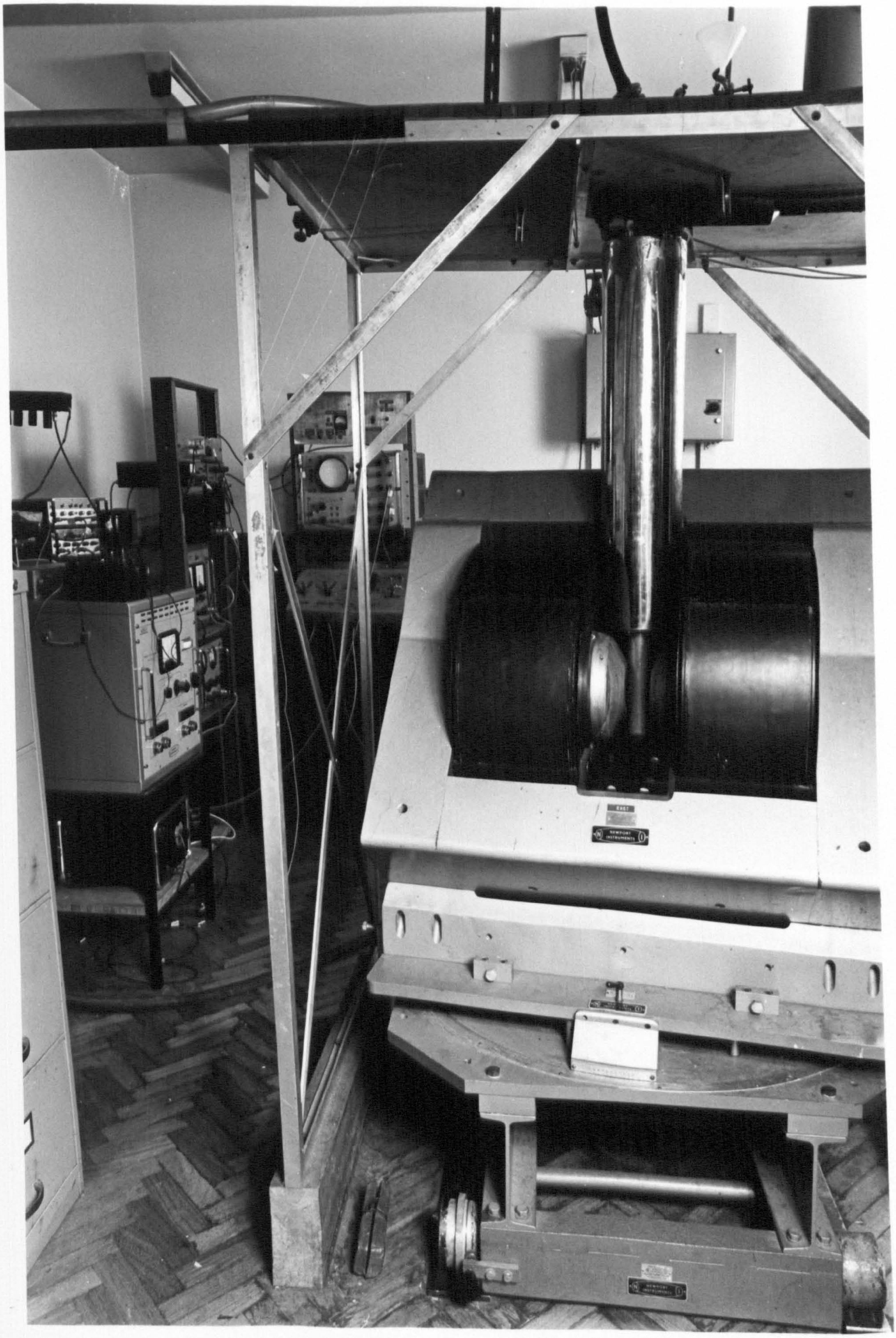

PLATE 1. General view of Apparatus.

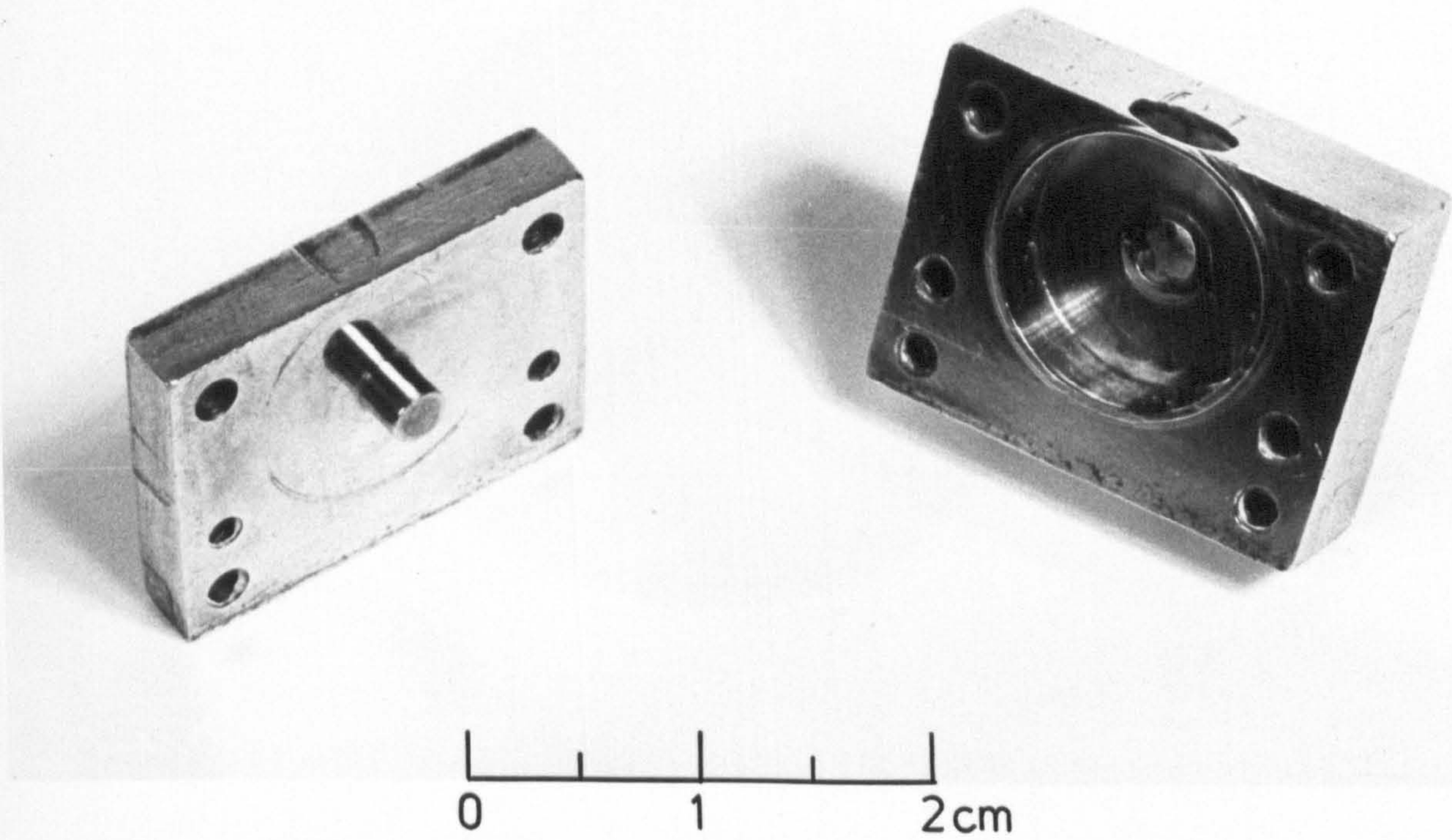

PLATE 2. Cavity used in stress experiments.

PLATE 3 . Specimen located in polishing ring, with glass feet.

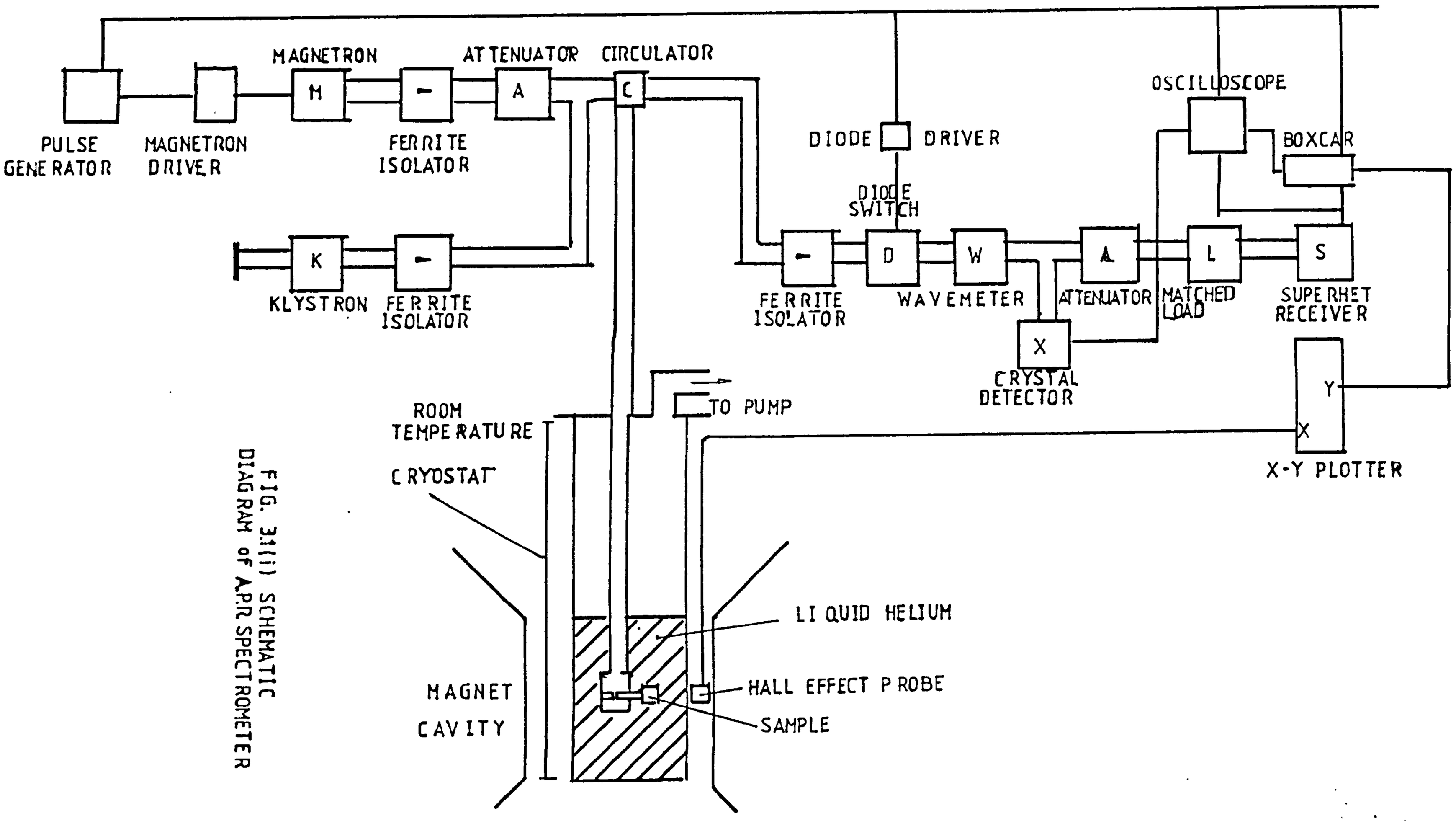

FIG. 3.1(i) SCHEMATIC DIAGRAM OF A.P.R. SPECTROMETER

were achieved using a Metals Research 'Multipol' polishing machine utilising soft-solder laps. The polishing materials found best for MgO (by experiment) were water soluble Hyprez diamond pastes of grain size 6μm and $^{1}/_{4}$μm. The sample was mounted in the centre of a brass ring (see Figure (plate) 3(2)(i)), surrounded by three sets of glass feet, the purpose of which was twofold : to balance the brass ring preventing the sample from rocking on the lap and to give a wider polished area to test for the necessary flatness and parallelism. Using a mild-steel jig, the brass ring could be attached to the magnetic chuck of the surface grinder and the sample and feet ground to a basic flatness. An accuracy of about ± 12μm in the thickness of each pair of feet could be obtained in this way. This could be improved to about ± 3μm by the use of graded carborundum papers. The sample was then transferred to the polisher and polished with the 6μm paste until a scratch free surface with the thickness of the feet accurate to ± 0.5μm was obtained. Final polishing with the 0.25μm paste gave a finish which was flat to one fringe of sodium light when placed against an optical flat, and with the thicknesses of the feet accurate to ± 0.1μm. This was judged to correspond to the required conditions.

3.2(iv) Calcium Oxide

The samples of Calcium oxide were obtained from Dr B Henderson of Keele University, now Professor Henderson, Trinity College, University of Dublin. The colour ranged from pink through orange to green and black. Sample preparation followed on identical procedure to that of MgO samples, except that care had to be taken to avoid contact between the strongly hydroscopic CaO and water. For this reason, the surface grinder was manually lubricated with light liquid paraffin during grinding (in place of its own water based lubricant) and oil-soluble Hyprez pastes were used in the polishing states. All CaO

samples were kept over phosphorus pentoxide in a vacuum dessicator. Samples 1 (pink), 2 (orange), 3 (purple), 4 (green) and 6 (pink) were aligned along the <100>, as for MgO, whilst sample 5 (pink) was aligned along the <110>.

3.2(v) Quartz Transducers

Several experiments reported in this thesis were performed using transducers produced in this department. Quartz plates were cut, and from these rectangular blocks with long sides parallel to the C-axis of the quartz were prepared by Dr V W Rampton, using the alignment and grinding techniques described above. These were turned down into cylinders of diameter 2.9mm by Mr I Cutts of the departmental workshop. Rods of suitable length were cut from the cylinders, and the ends optically polished by the above-described method to the same standards as the samples. Several damaged commercially made transducers were also re-polished in this way, using 6μm Hyprez diamond paste, and then a mixture of 0 3μm alumina powder suspended in Teepol cleaning fluid The success rate of transducers produced this way was not high, but three rods were produced which compared reasonably with those supplied by Messrs Gdoch and Housego.

3.3 Bonding Between Samples and Transducer

A number of different bonding materials and techniques were tested and utilised during the course of this work. Originally a 'Nonak' grease bond was prepared under finger pressure. This gave a sufficiently thin layer for good acoustic transmission. Attempts to form a bond of Araldite AV/HV 100 (conventional tube epoxy) in a similar fashion failed to give reproducibility. Similar results were obtained for tube 'Rapid Araldite', although the reproducibility was better. A simple press was constructed, which improved the results of araldite

BONDING MATERIAL	PREPARATION	CURING	PRESSING METHOD		
			HAND	PRESS 1	PRESS 2
NONAK GREASE	NONE, DOES NOT CURE		1:2 typical	1:2 typical	1 : 8 best (B)
ARALDITE AY/HV 100	50 % Epoxy resin 50 % hardener (by volume)	24 hours at room temp.	1 : 0·5 best	1: 1 best	1: 1·5 best
	80 % resin 20 % hardener mixed at 80 °C	2 hours at 60 °C 22 hours at room temp.	1·· 1·5 best	1 NOT TESTED	1 : 2 typical
ARALDITE " RAPID EPOXY "	50 % resin, 50 % hardener mixed at room temp	24 hours room temp.	1 : 0·5 best	1 : 1 best	NOT TESTED
	50 % resin, 50 % hardener 80 °C mixture	2 hours at 60 °C 22 hours at room temp.	1: 1 best	1 : 1·5 best	NOT TESTED

NOTES:
1. Results are quoted as Size of bond echo (1) vs Size of first sample echo
2. Where a "best" result is quoted, this is an indication of poor bond reproducibility, except for (B), where one experiment only was performed, as NONAK grease contains too much water to be used with the CaO samples in use at this time.

TABLE 3.3(ii). BONDING DATA

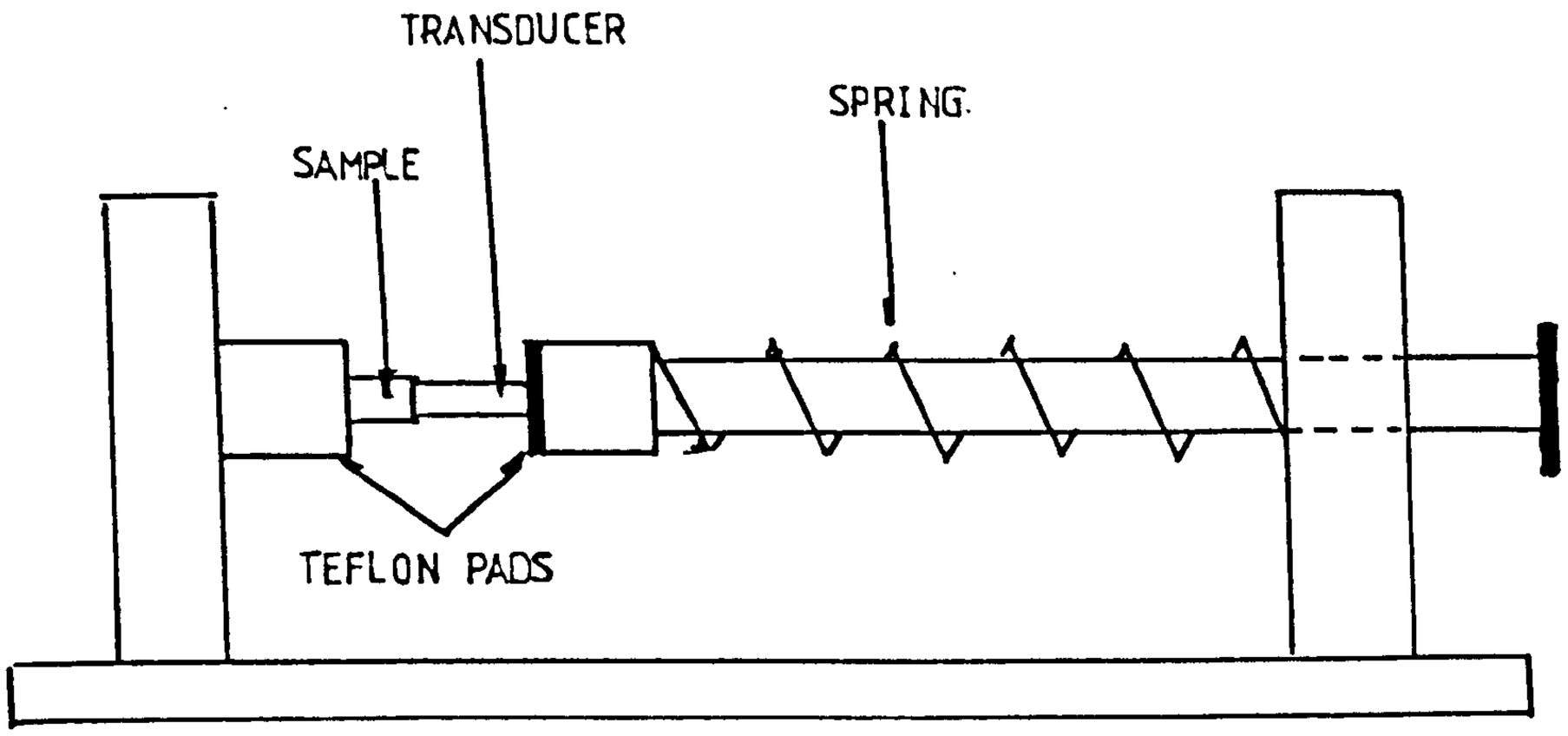

FIG 3.3 (i) BONDING PRESSES : SPRING PRESS (above)
: SHOT (new) PRESS (below)

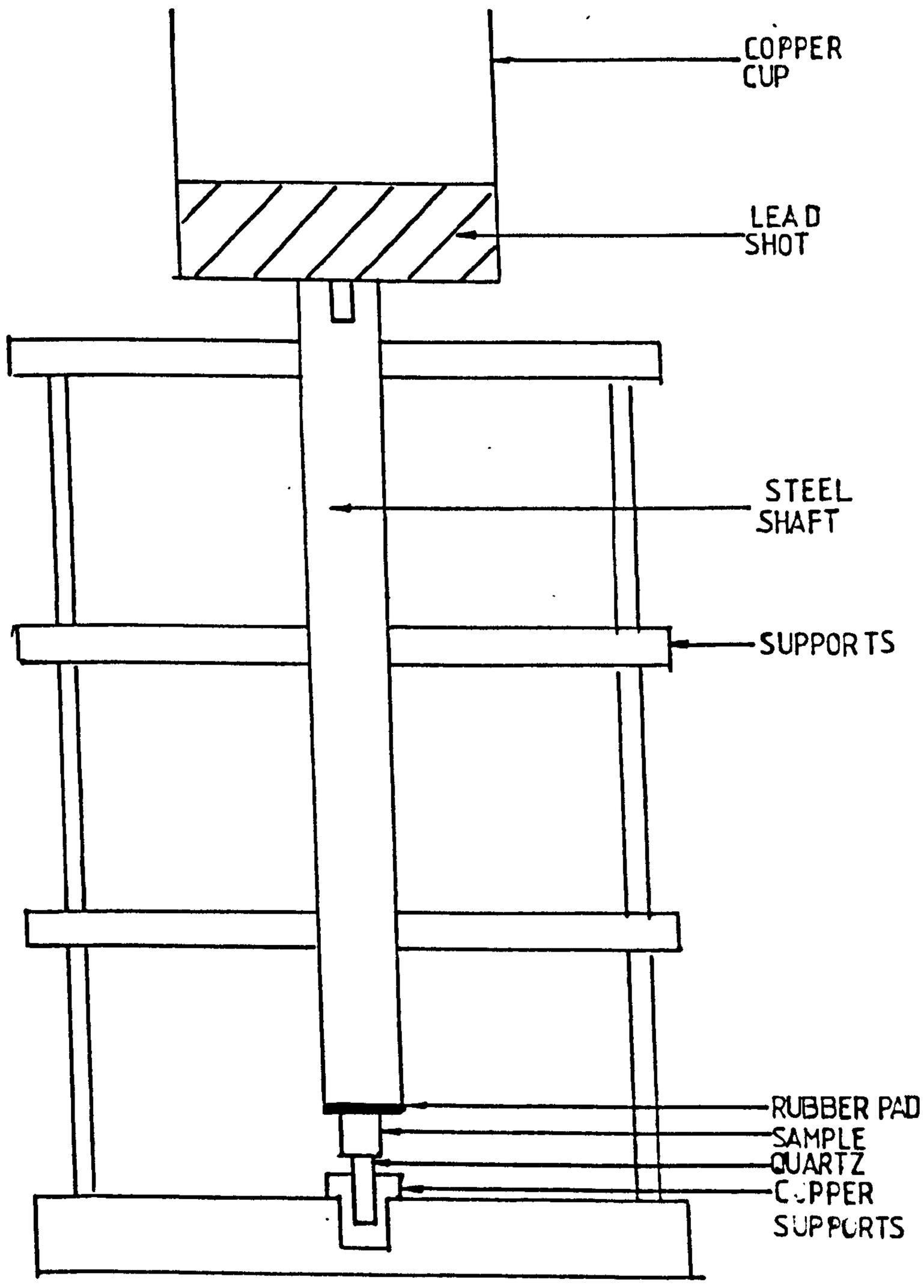

bonding (Figure 3.3(i)A). Further improvements were obtained by using an 80% AV100 20% HV100 mixture (in place of the usual 50-50 mixture), by heating the resin and hardner to 80°C before mixing and by curing for two hours at 60°C before curing for a further 24 hours at room temperature. All CaO samples were bonded using araldite AV/HV100 prepared as above, since the high water content of the Nonak grease caused a deterioration in CaO sample surface polish. MgO samples were generally bonded using Nonak, although later experiments utilised heated 'Rapid' Araldite bonds. A crystal press (built in the third year project rooms under Dr P J King), (Figure 3.3(i)B), was used during the 60°C curing, whilst the room temperature cooling was carried out in the dessicator, with no applied pressure.

The quality of bonds was tested using a 110 MHz pulse-echo machine working at room temperature. Transducer quality could be tested on the same device, and could be judged on both the size of the size of the first transducer echo and the number of transducer echos, prior to bonding. Bond quality could then be judged on the acoustic transparaency of the bond, i.e. by the relative sizes of the bond and sample echos after the bond was fully cured. Typical results for the various bonding types are shown in Table 3.3(i).

3.4 Generators

3.4(i) Klystron

The Klystron used was a Mullard 2K25, powered by a Solartron Klystron Power Supply. A band of power is produced from the Klystron by adjustment of the supply, such that a frequency sweep of about 100 MHz is obtained. The centre of this band can be tuned by an adjustment of the Klystron itself. The range this produced was typically 8.5 to 10.5 GHz. The cavity resonance is by comparison narrow (typically 20 MHz). Measurement of the cavity resonant frequency

FIG. 3.4 (i). MAGNETRON DRIVER CIRCUIT

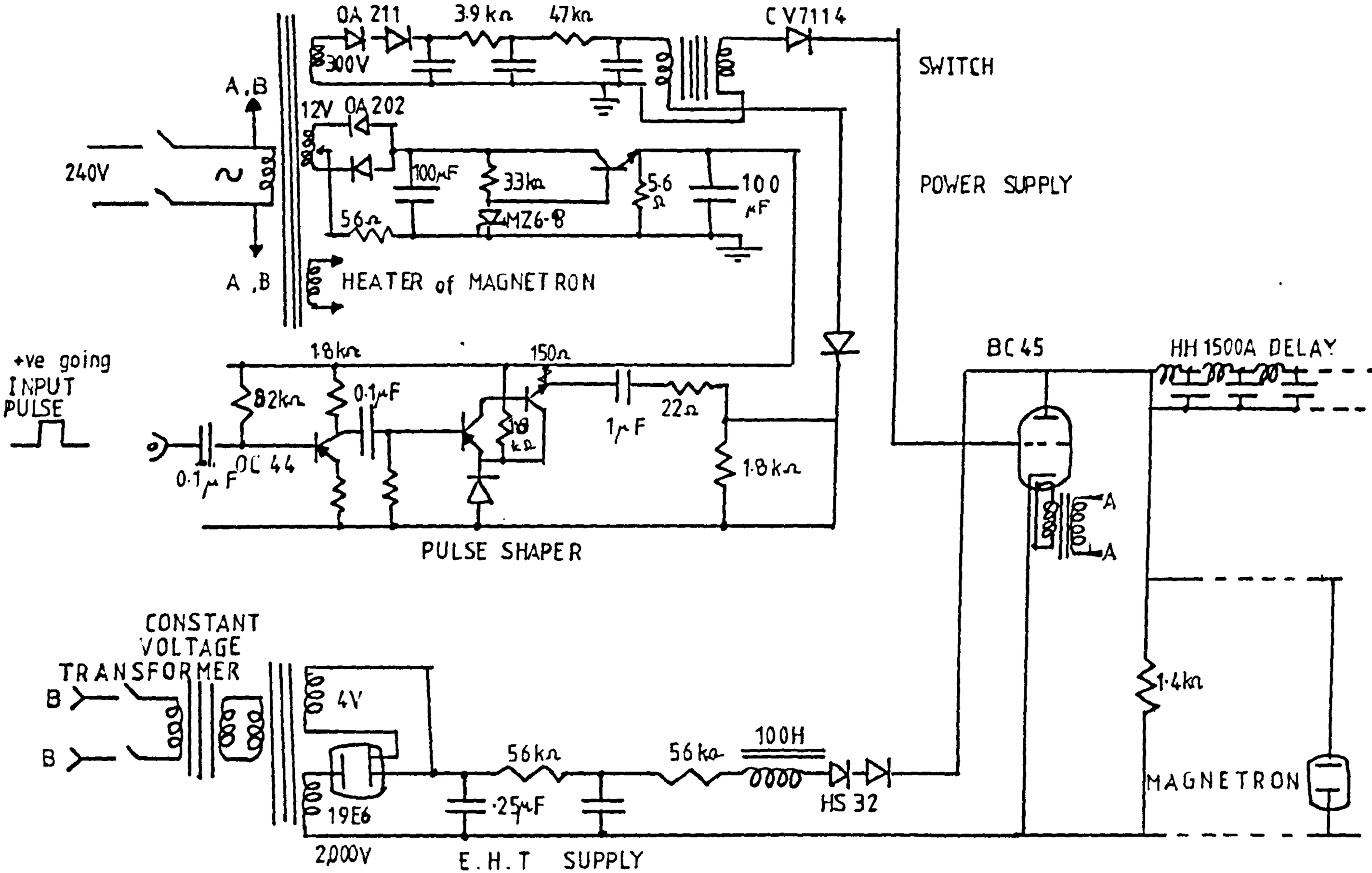

can be made by means of a calibrated cylindrical wavemeter. Klystron power was typically 20mW, continuous wave.

3.4(ii) Magnetron

The magnetron used was a Mullard type JPT9-02. The device was driven by a Dawe pulse generator type 412B, producing pulses of duration 0.5μsecs, pulse repeat frequency 1000 Hz. A magnetron driver built in this department was used to amplify these pulses to the 1KV necessary for the magnetron. Details of this driver are given by Brabin-Smith (1969) and a circuit diagram is included as Figure 3.4(i). The magnetron produced pulses of microwave power of about 20 watts, of duration around 0.8μsecs at the base, 0.4μsecs at half-height. The pulse power arriving at the cavity is reduced by a 3dB attenuation in the Microwave Instruments directional coupler, giving about 12 watts at the cavity. The magnetrons are typically tunable from 9.1 GHz to 9.6 GHz.

3.4(iii) Solid-State Generators

A series of experiments were carried out on a type of solid-state generator utilising Hewlett-Packard Impatt diodes. These devices, in the correct resonant cavity, can produce pulse powers of up to 10 watts, tunable over a wider range than a typical magnetron, and at duty cycles as high as 25%. A full description of the experiments carried out on these devices, together with a brief description of the theory of the Impatt diode, is included in Appendix B. The results obtained were fairly encouraging,and it is hoped that in the near future solid-state generators based on both these devices and upon Gunn diode systems will be in use in APR experiments in this department.

3.5 Detection

3.5(i) Receiver and Crystal Detector

During setting up procedure a crystal detector was used in conjunction with a Hewlett-Packard Type HP175A oscilloscope to display a trace representing microwave level against frequency. This allowed the cavity resonance to be located and monitored during the cooling process. The broad band response of the crystal enabled wide ranges of Klystron tunings to be made without the necessity for any detector tuning. This is particularly advantageous when 4.2K is reached, as the cavity resonance changes by some 100 MHz at this point. During the experiment itself a low noise superheterodyne receiver was used. The instrument utilised in these experiments was a Decca Type MW78 receiver of bandwidth 14 MHz, intermediate frequency 30 MHz and sensitivity 10^{-12} watts for a 2:1 signal to noise ratio (manufacturer's specification). The local oscillator used was a type 2K25 klystron feeding a crystal mixer. Previous experiments (Brabin-Smith 1969) have shown the response law of the total receiver system to be

$$\text{echo height} \propto \text{power}^{4/3} \quad (\text{input power} < 2 \times 10^{-6}\ \text{w}).$$

3.5(ii) The Boxcar System

The detected signal from the superhet receiver was fed into a Brookdeal boxcar system. This device consists of two parts, a variable delay, variable pulse width, gate generator type 425A and a DC level voltmeter/averager type 415. The gate generator is triggered by the same pulse generator used to trigger the oscilloscope and the magnetron, the Dawe 412B. A gate of known width can then be produced, which can be delayed to a set time behind the trigger pulse, or can be swept automatically over a range of delays. In practice the gate is manually set such that it co-incides with the arrival of one particular sample echo in the train following the trigger pulse. This is acheived by

observing the echo train on channel A of the oscilloscope and the output of the gate generator on channel B. The gate delay can then be varied until the traces of the gate and the desired echo co-incide in position. Both the output of the superhet and the output of the gate generator are connected to the DC averager. The gate serves as a reference input, and switches the averager on and off. Since the gate co-incides with the echo of interest, the averager/voltmeter will only measure the value of the maximum size of this particular echo. The number of pulses over which the averaging is carried out is varied by means of a time constant control, the criteria for averaging time being set by the speed of the magnetic field sweep and the pulse repeat frequency. In practice a slow sweep is used to allow long averaging times, to reduce noice on the trace due to random changes in echo size from pulse to pulse. The output of the voltmeter/averager is fed direclty to the Y input of a Bryons type 26000 A3 XY recorder.

3.6(i) Waveguide Components

The waveguide components are listed in Figure 3.1(i). They are all commercial X-band equipment. High conductivity copper rectangular waveguide was used, except in the cryostat, where thermal considerations made the use of stainless steel preferable.

3.6(ii) The Protecting Diodes

The exception to the above was the diode protection system. This unit was based on the design of Millet (1958). The diodes are biased in such a way that there is 40 dB of attenuation in the line during the magnetron firing. This is achieved using the diode driver circuit shown in Figure 3.6(i). The driver is triggered using the same pulse generator that triggers the magnetron, the oscilloscope and the boxcar system.

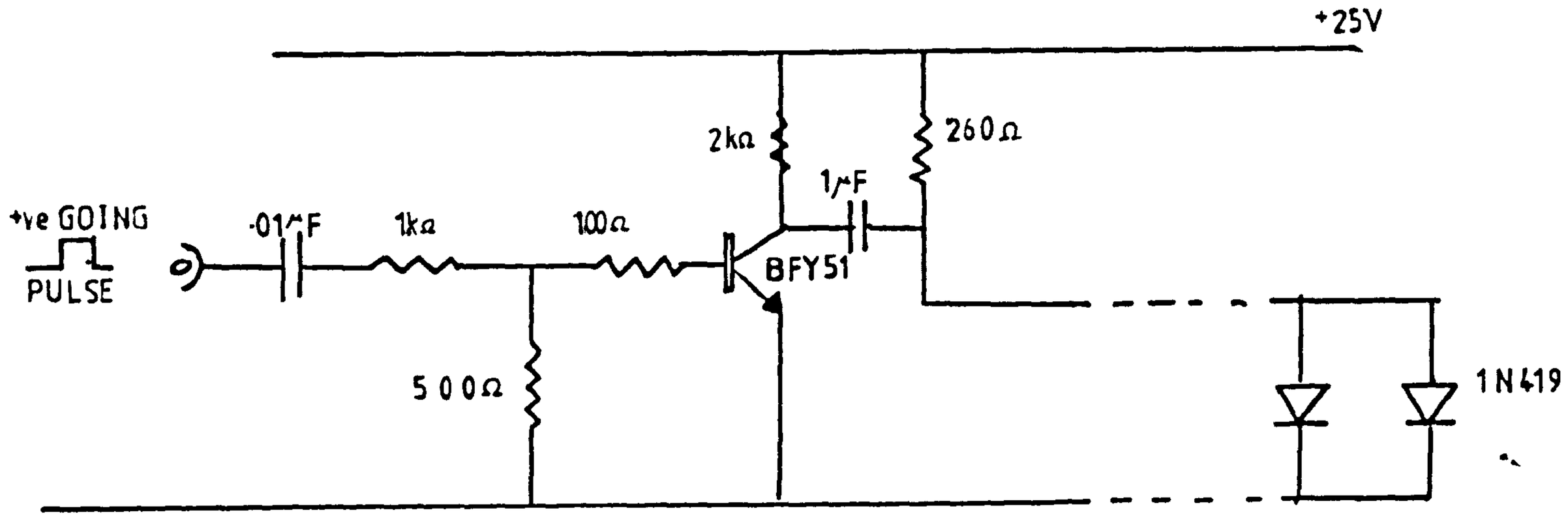

FIG. 3.6(i): DIODE DRIVER CIRCUIT

3.7 The Cryostats and Cavities

3.7(i) The External Stress Cryostat used for MgO Work

The cryostat designed for external stress work, Figure 3.7(i), plate 3.4; had several special features. A 'table' extends from the cavity wall to support the sample rigidly when the stress is applied. The stainless steel waveguide is connected to the non-cryogenic copper parts by a flexible rubber junction, the purpose of which is to allow any difference in thermal contraction between the waveguide and the stress application tubes to be taken up in vertical motion of the waveguide rather than by a bending motion, which, in addition to the possibility of causing a touch between the helium and nitrogen jackets of ther dewar (section 3 (8)), could also invalidate the readings of external stress by causing friction due to bending in the concentric stainless steel pressure tubes. The stress is applied to the sample by means of a stainless steel plug resting on the sample, free to pivot through small angles about a horizontal axis in such a way that the stress is applied to the whole surface area of the sample evenly, even if a missalignment occurs. In addition to this the surface area of the plug is larger that than of the sample, which also allows the surface stress distribution to be kept even. The plug sits inside the inner of two concentric stainless steel tubes, the other end of which is connected to the lever system by which the stress is applied. The outer tube is fixed firmly to the cryostat top-plate at one and and to a stainless steel yoke which fits firmly round the sample table at the other end. Two lever systems were used during the course of the experiments to enable variable stress to be applied. The first allowed a number of large masses to be hung from a fixed point on the lever, whilst the second allowed a fixed mass to be moved along a calibrated lever-bar.

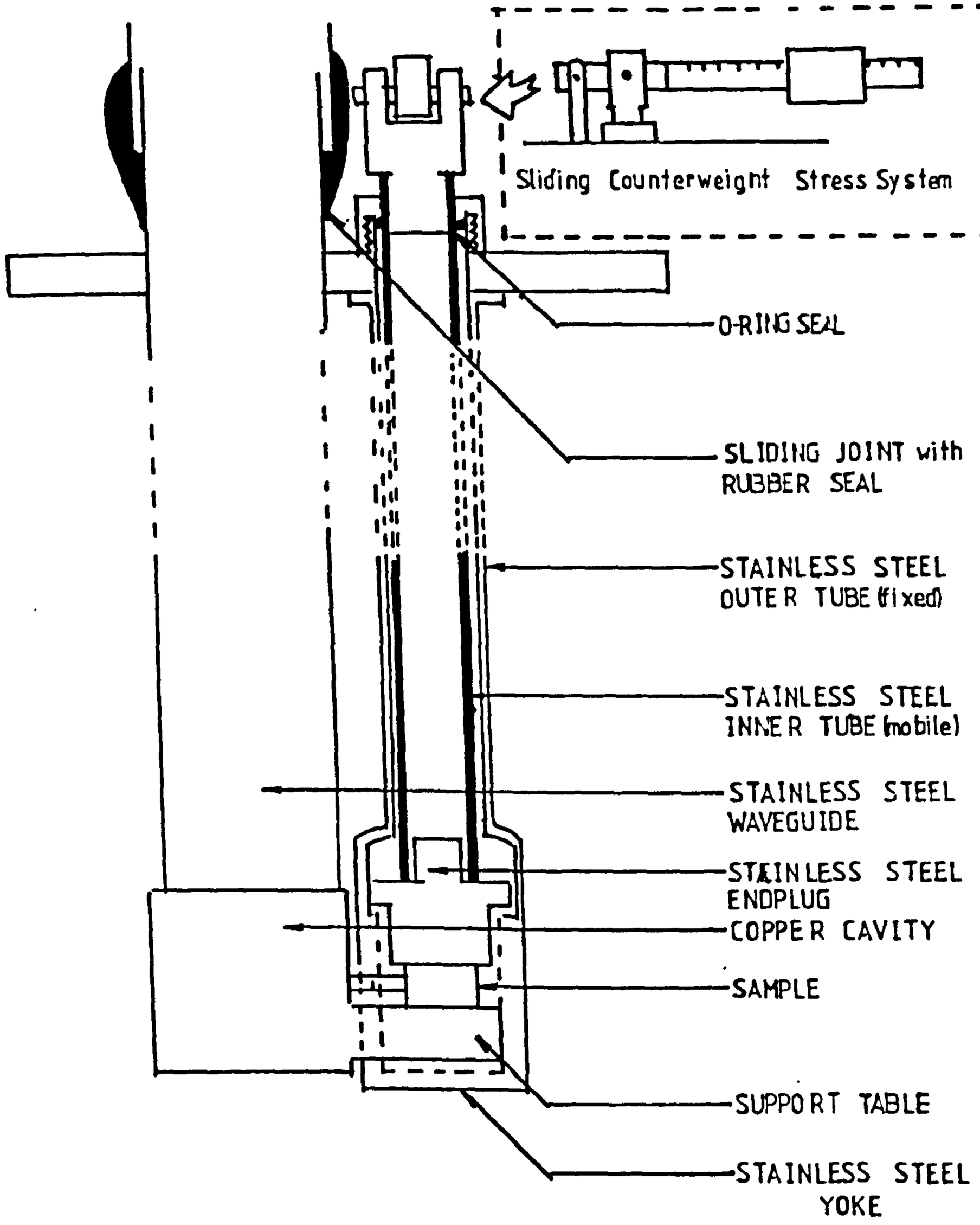

FIG. 3.7(i). STRESS CRYOSTAT & AXIS DEFINITION

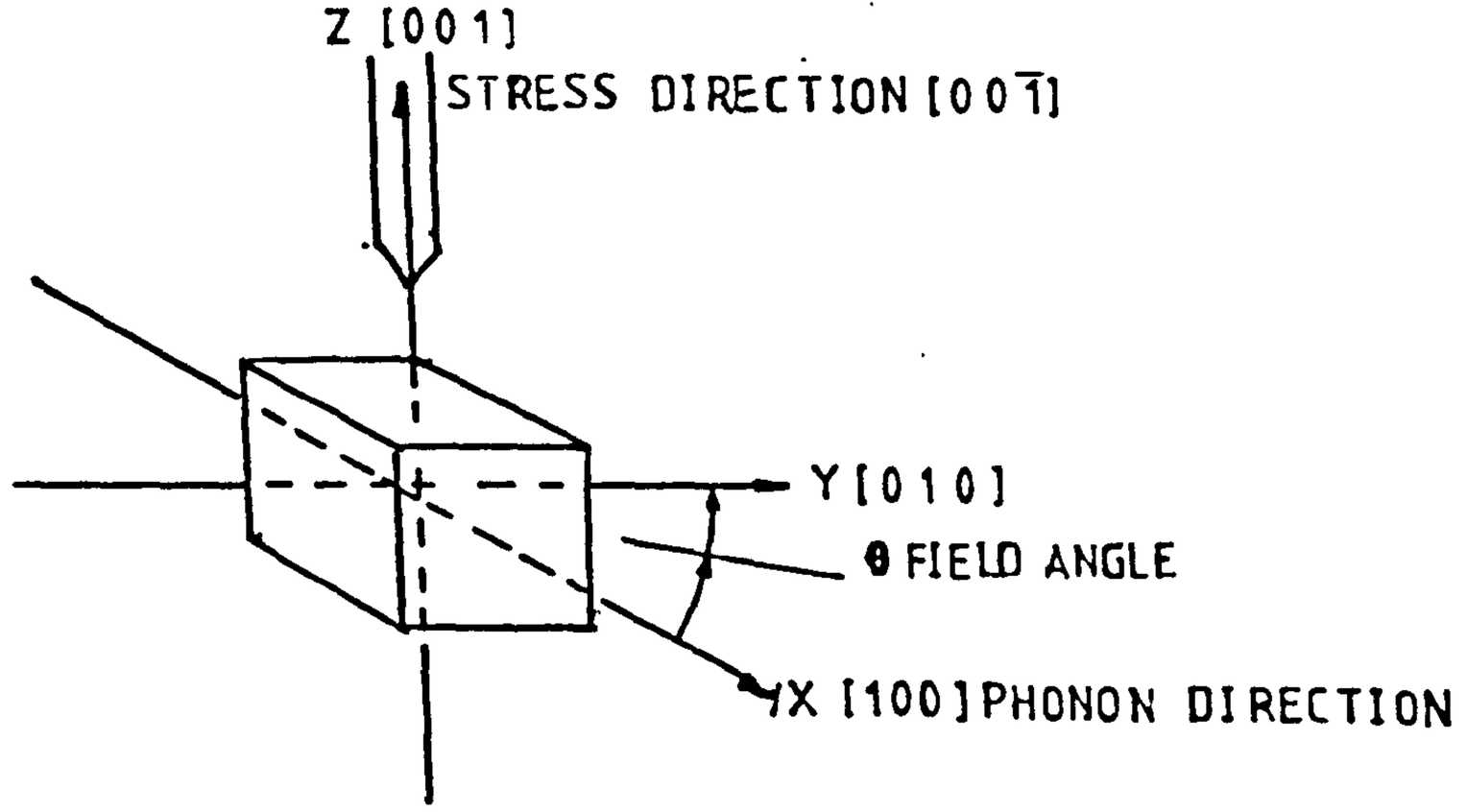

3.7(ii) The Rotating Sample Cryostat

A laboratory frame of reference was defined such that direction x was parallel with the phonon direction, the y-axis was horizontal in the laboratory and orthogonal to the phonon direction, and the z-axis was vertical in the laboratory, and orthogonal to the x-y plane. A cryostat was used which enabled the sample to be rotated in the y-z plane about the x-axis. The angle of rotation was called ϕ. The magnetic field direction could be rotated about the z-axis in the x-y plane; the angle of rotation was called θ. The cryostat and axis definition is shown in Figure 3.7(ii). The importance of these movements was to enable the magnetic field to be aligned with the <111> direction of the crystal to examine effects predicted by Fletcher (1971) described in Chapted 5.3. The cryostat has been described by Brabin-Smith (1969) and Atkinson (1976). A worm wheel is fixed to the quartz transducer using 'Evostick' impact adhesive. The worm wheel is rotated by a worm attached to a shaft which can be rotated from outside the dewar. By appropriate choice of the gear ratios, an external meter could read the rotation of the sample directly, in degrees.

3.7(iii) The Cavity

The cavities used in both sets of experiments were of the same design (Figure 3.7(iii)) All cavity dimensions are given on the figure. Critical coupling can be acheived by filing of the coupling iris. Moreno, 1948, gives a formula for the resonant wavelength of the cavity considered as a coaxial line terminated by a capacitance:

$$\lambda o = 2\pi \left(\frac{La^2 E}{2d} \log_e \frac{b}{a} \right)^{\frac{1}{2}}$$

E = the dielectric constant, all other terms defined in Figure 3.7(iii). In practice this formula does not totally apply, and the cavity has to be tuned up by moving the transducer in and out of the

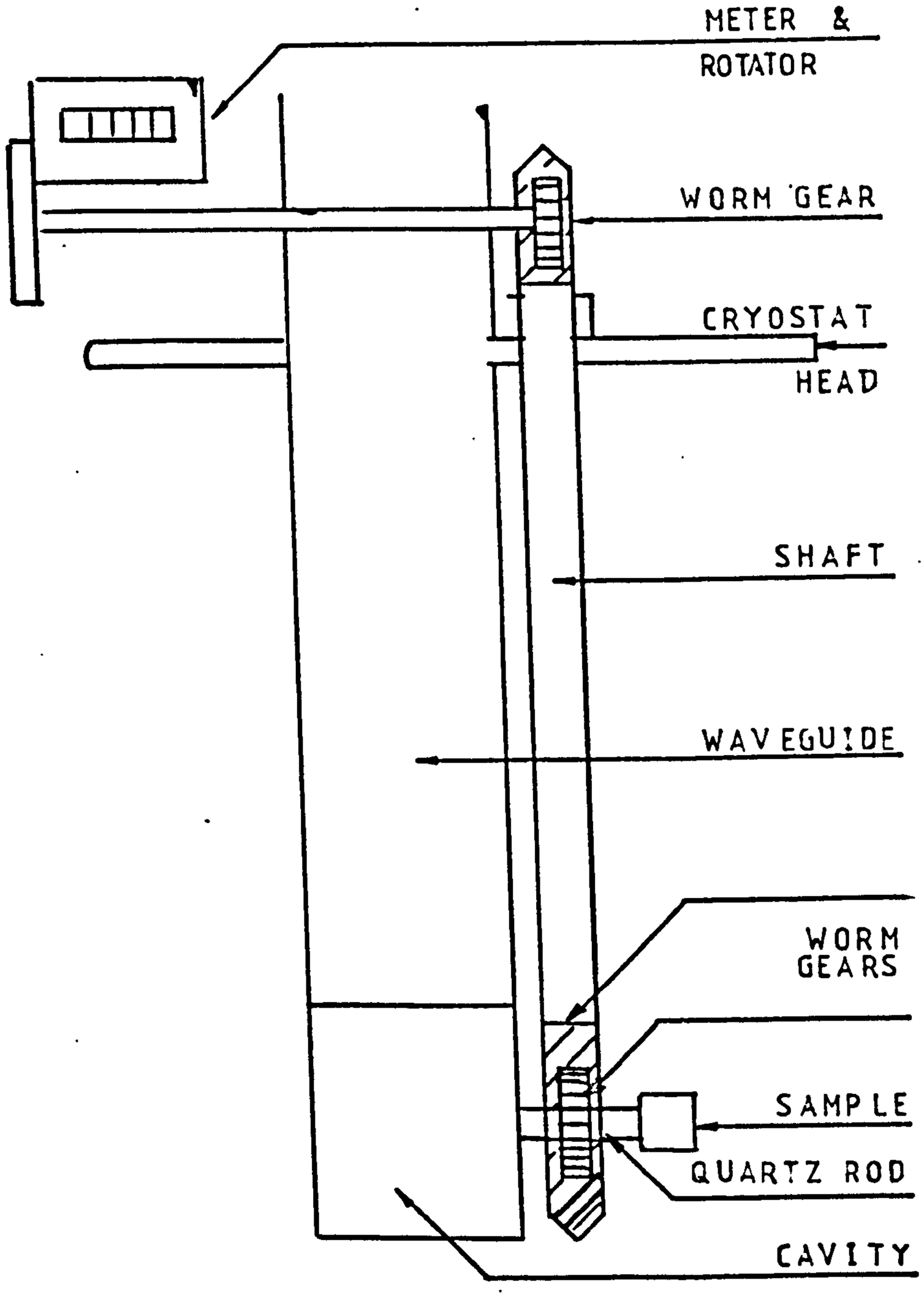

FIG. 3.7.(iii) ROTATION CRYOSTAT & AXIS DEFINITION

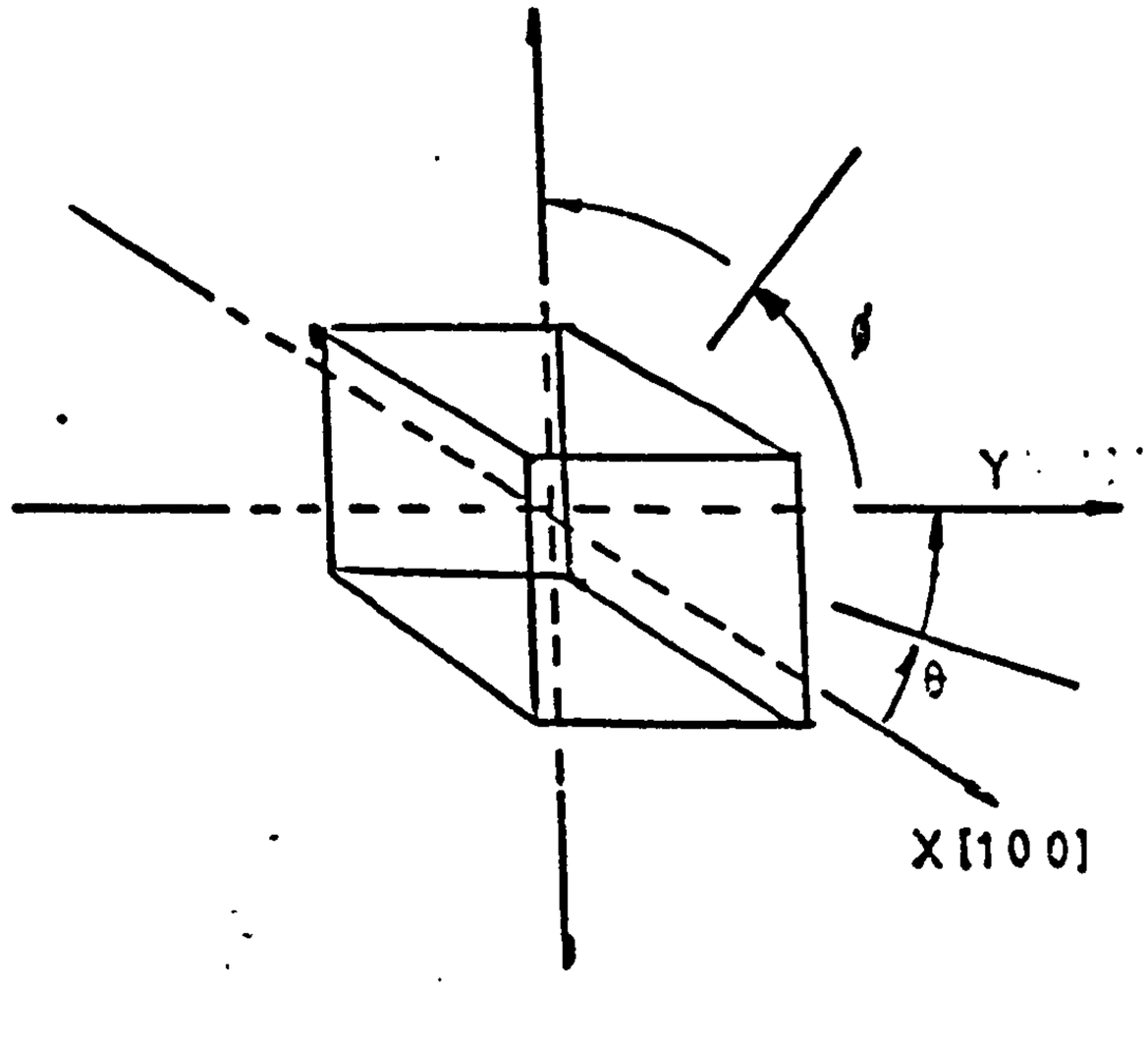

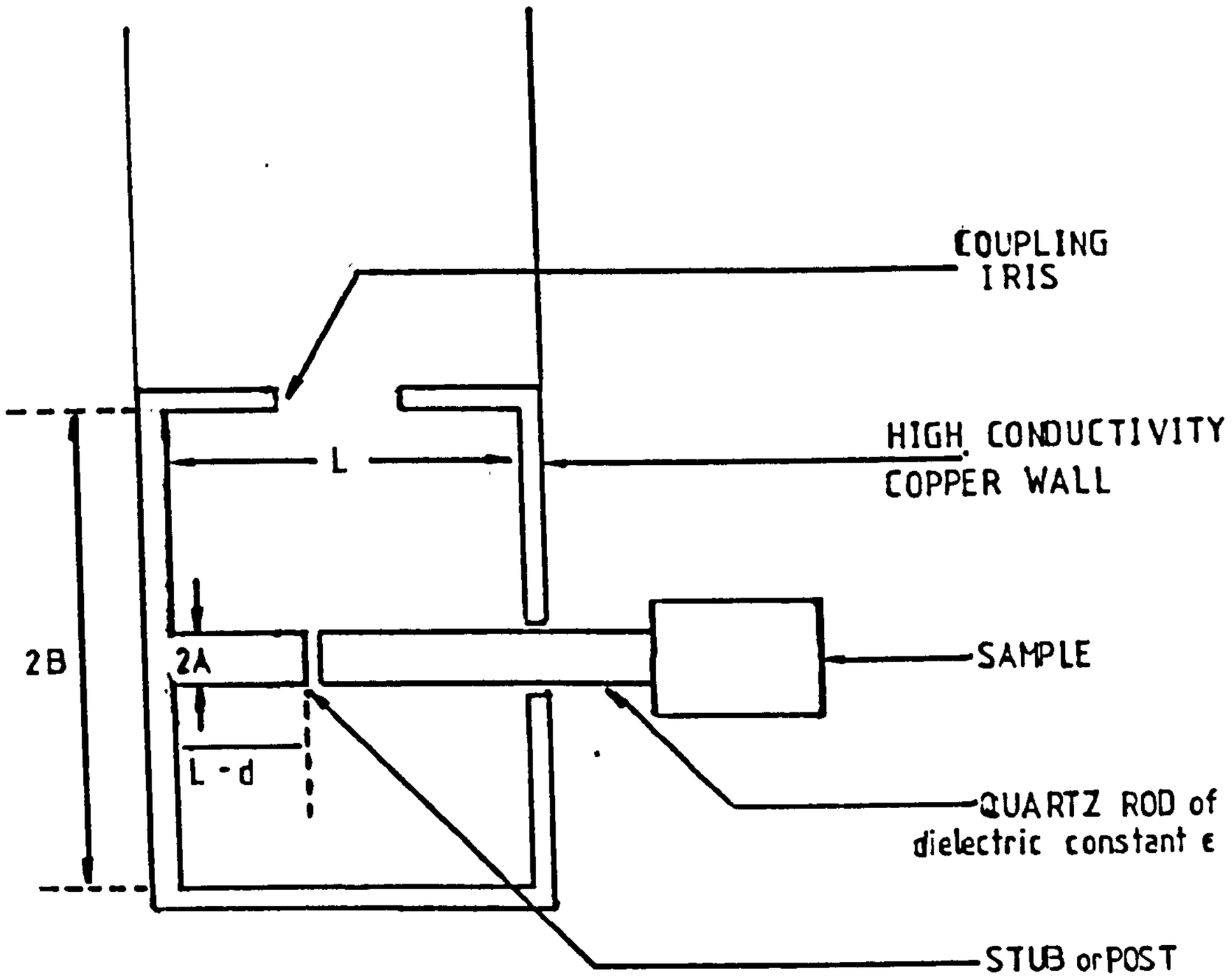

◆ DIMENSIONS ◆

2A	:	Stub Diameter :	3 mm
2B	:	Cavity Internal Diameter	13·3 mm
L - d	:	Stub Length	2·71 mm
L	:	Cavity Depth	4·15 mm

FIG. 3.7 (iii). CROSS-SECTION THROUGH CYLINDRICAL RE-ENTRANT CAVITY, WITH DIMENSIONS

the cavity very slightly until the desired frequency is obtained. Usually a room temperature frequency of about 200 MHz higher than the desired experimental frequency was obtained to take account of the change in E, and change in size, when the cavity becomes full of helium on cooling. Normally a room temperature frequency of about 9.6 GHz was chosen.

3.8 The Cryogenic Equipment

The dewar system was supplied by Thor Cryogenics Ltd (Figure 3.8(i)). The walls were of stainless steel, except for the detachable tails, which were made of brass. The outside wall was nickel plated. The vacuum spaces contained superinsulation. The nitrogen jacket contains about 2 litres of liquid when full. All cryostats were fitted with two or more radiation baffles of thin copper or stainless steel sheet. The transfer lines were doubled walled German Silver, evacuated between the walls, outside the cryostat, and single wall German Silver inside. By pumping on the liquid helium in this system with an Edwards ED220 rotary pump through a 1.5 inch line, temperatures in the range 1.4 K to 4.2 K could be achieved, the temperature was obtained by measuring the helium vapour pressure with mercury and vacuum-pump oil manometers.

3.9 The Magnet

The magnet used was a Newport, 11 inch type F, which produced fields from zero to 2.2 T with a 5 cm pole gap. The homogeneity of the field was specified as 3 parts in 10^6 over a 1.5 cm^3 volume central between the pole pieces. The magnet was powered by a Newport type C904 b 20 kw supply and sweep unit. Field strength was measured using an AE1 Hall Effect Probe Mark III A. This device was driven by a constant current power supply, circuit

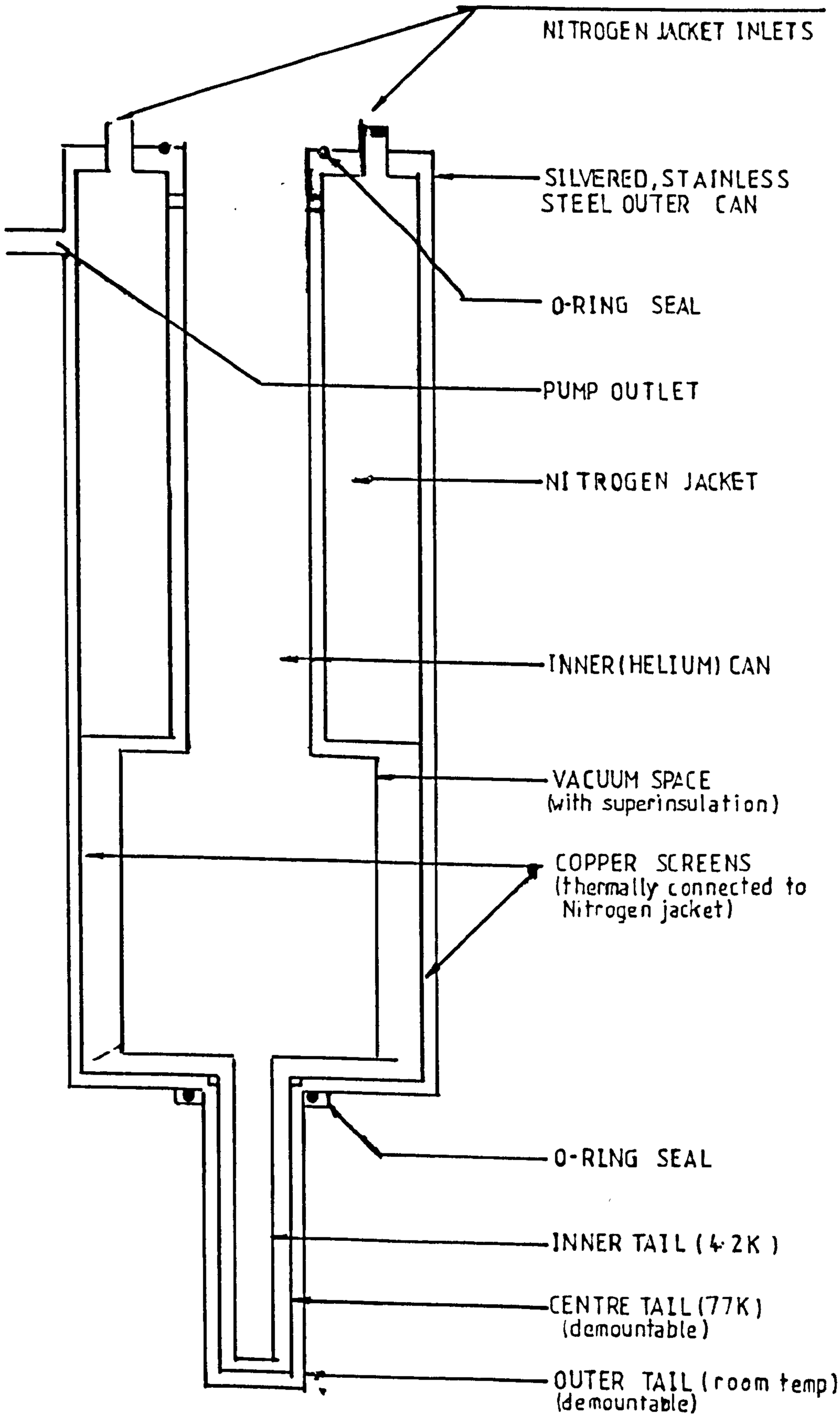

FIG. 3.8 (i) DEWAR SYSTEM

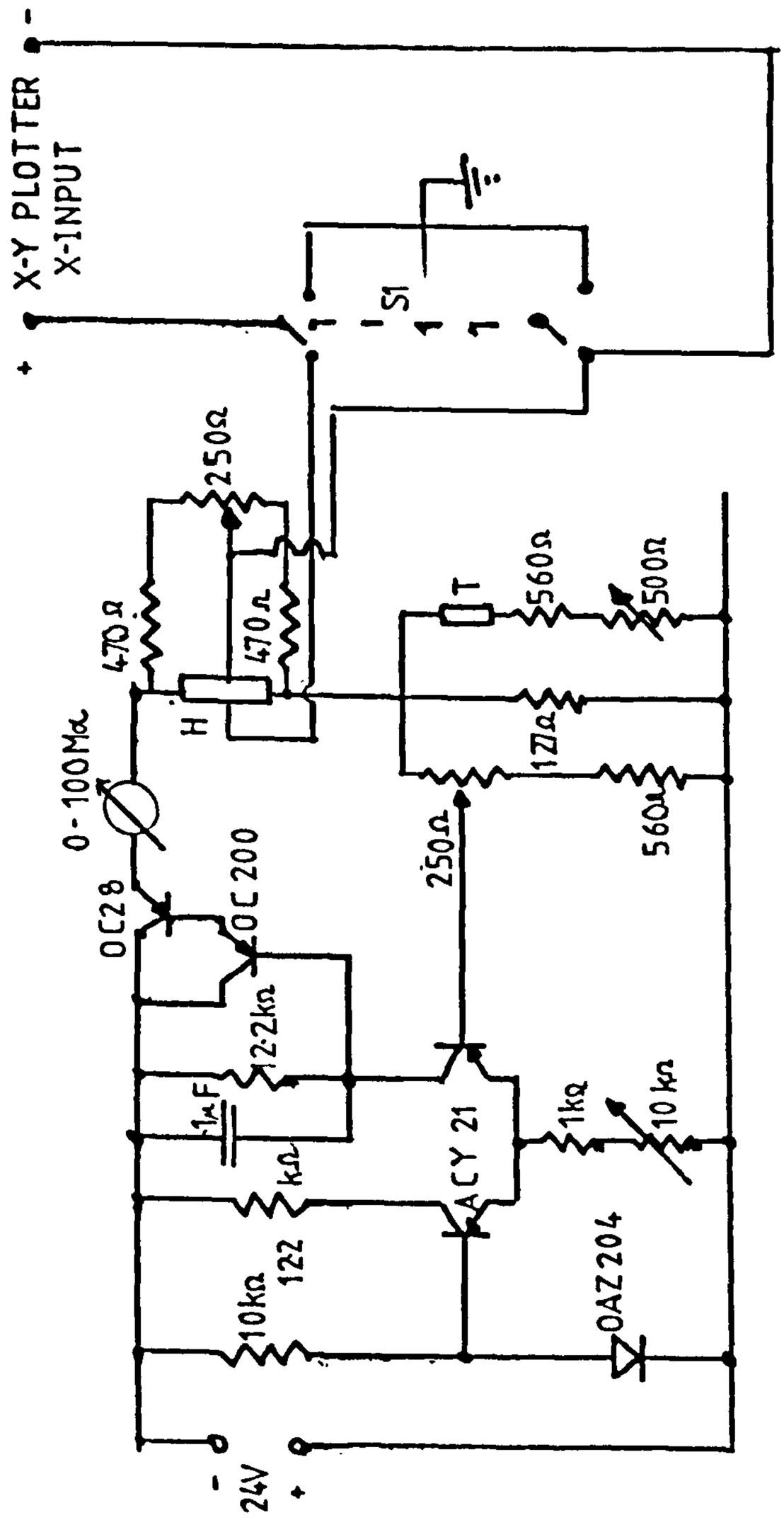

H = HALL PROBE
T = THERMISTOR

FIG. 3.9(i) HALL PROBE SUPPLY

given in Figure 3.9(i). At regular intervals throughout the period of this work, field calibration was checked using a Rawson moving coil Gaussmeter. It should be noted that for a period of time the Hall probe output calibration changed, and at a later date changed back. The reason for this was not known, but since calibration reproducibility was accurate in both cases, the changed calibration was used without changing the probe or its driver.

3.10 The ESR Spectrometer

A simple room-temperature ESR spectrometer operating at X-band frequencies was constructed. A schematic diagram is given in Figure 3.10(i). Magnetic fields from zero up to about 1 T could be obtained using a Newport iron-cored electromagnet, type E, with 7 inch pole pieces. The generator used was a Standard Laboratories 300 A stabilised klystron, which could be locked onto the chosen frequency. Critical coupling was achieved by moving a dielectric filling in a narrow, cut-off, waveguide. A bypass system, around the circulator, enabled the crystal detector to be biased with power from the klystron.

The spectrometer was used to investigate the presence of Cr^{3+} in the CaO samples, which is not detectable, in low concentrations, by APR. It was hoped to show some correlation between the Cr^{3+} and Cr^{2+} concentrations in the various samples.

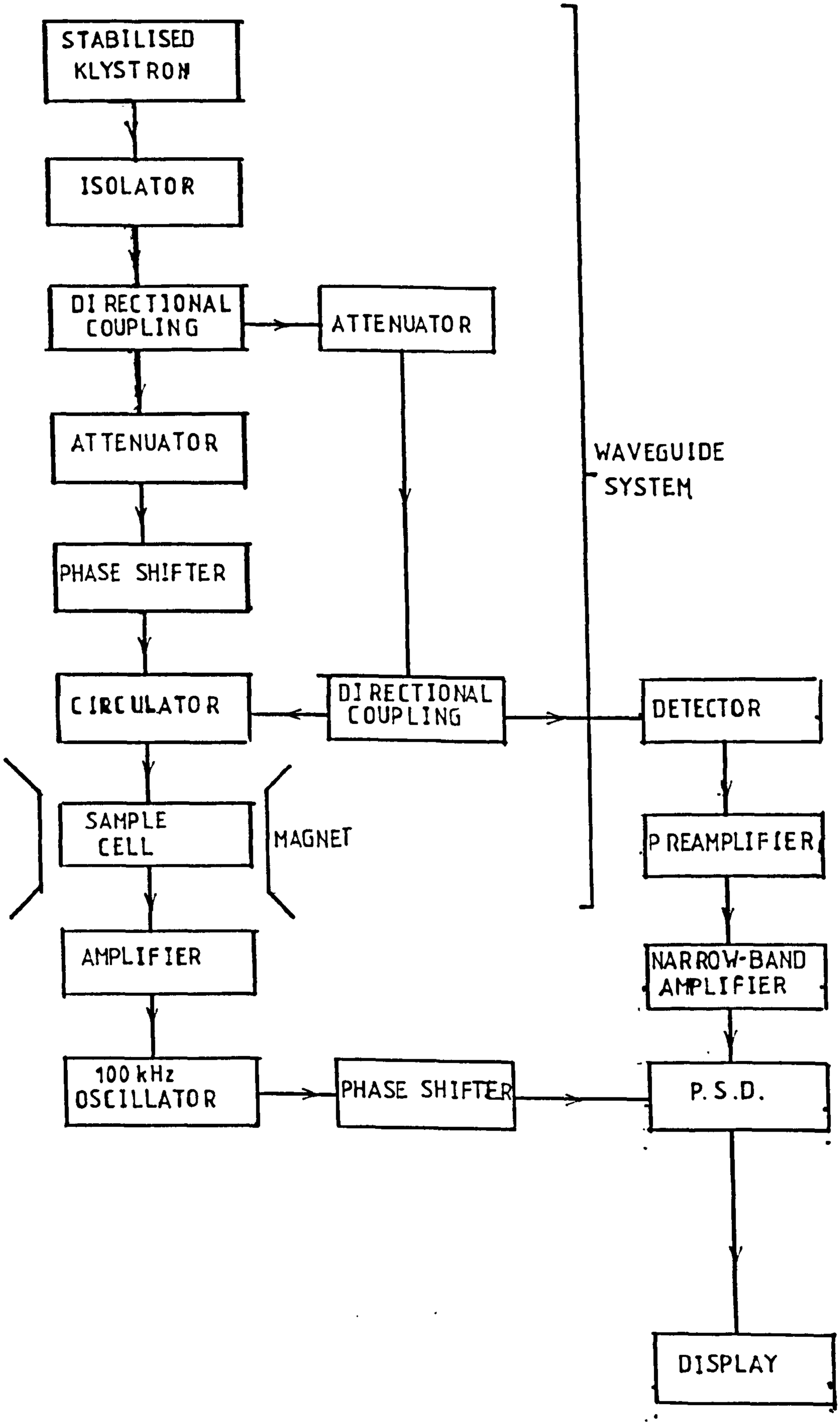

FIG. 3.10.(i). E.S.R. SPECTROMETER, SCHEMATIC.

CHAPTER 4

THE CHROMOUS ION IN MgO

4.1 Introduction

MgO is a cubic crystal system widely used as a host material for paramagnetic resonance experiments. Chromium ions replace the magnesium ions in the centre of an octahedron of oxygen ions. Preferentially it is the trivalent Cr^{3+} ion which performs this replacement, but lower concentrations of Cr^{2+} occur. Various techniques can be employed to change the relative concentrations of the chromic and chromous ions. In this work, annealing in selected atmospheric conditions was chosen as a valence changing mechanism. Work on the effect of annealing has been performed by Marshall (1967), Anderson et al (1975), and King and Oates (1974 Private communication). A description of this technique is given in section 4.5 below, together with a short discussion of the results obtained and some unusual features which were observed.

This replacement of the Mg^{2+} ion by the chromous ion introduces distortions into the lattice. The form of the distortions and their relevance to the spectrum observed is discussed in section 4.3 below, the theory section. To a first approximation, however, the spectrum may be considered to arise from ions undergoing tetragonal distortion aligned with the <100>, <010> or <001> crystal axes. The ions undergo a dynamic Jahn-Teller effect.

The earlier work of Marshall and Rampton (1968) (see section 4.2(i)) led to interpretations by Fletcher and Stevens (1969) and Ham (1971). Both used the cluster model but Fletcher and Stevens concluded that the ions underwent strictly tetragonal distortions, whereas Ham allows random lattice strains, and shows how ions in

sites of near tetragonal symmetry are the only ones contributing to the APR absorption. Both interpretations account quantitatively for the results of Marshall and Rampton. A brief description of Ham's theory and the differences between the two interpretations is included in section 4.3 below, however, the theory of Ham is used in he analysis of results performed in this chapter. It must be said that the present results do not heavily influence a preference for either of the sets of assumptions on which the two interpretations are based. They do, however, suggest a further line of enquiry which may enable the clarification of the situation, such that a single interpretation could be produced.

The experiments carried out on this system are presented as outlined below. For the main part experimental results are given in chronological order, and some explanation of the logical connection between an experiment and its antecedent is given.

First experiments: Initially samples were prepared from the single crystal magnesium oxide in the 'as received' state. Such crystals have undergone no annealing processes and the concentrations of Cr^{2+} and Cr^{3+} result purely from the growing process.

Acoustic absorption at 4.2 K is very great, and no sample echos are seen. A large thermal relaxation peak centred on 6 K (King et al 1976) accounts for this. Cooling to 2 K enabled the effect of this peak to be reduced and sample echos were produced. A fairly complex spectrum was observed under these conditions.

Heat treatments: To simplify the spectra being observed, and to make experiments possible at 4.2 K, the samples were annealed under specific conditions of

atmosphere and temperature. Control anneals in air were carried out at the same time.

Experiments were performed on the annealed samples to determine the annealing conditions which optimised the chromous spectrum for experiments at 4.2K.

Further experiemnts: The best sample resulting from the annealing process was subjected to varying external stresses applied in two ways. Initially, a number of fixed masses could be hung from a fixed point on a lever system, giving fairly large changes in stress between one reading and the next. This system was adapted to enable a single fixed mass to be slid along a lever, giving a range of continuously variable stresses. From the results obtained calculations could be made, based on the Ham theory, of the shift in the spectroscopic splitting factor, g, of the transition levels and, ultimately, of the ratio of strain coupling to spin-orbit coupling constants. These results were compared with those obtained by other workers using different experimental techniques.

The chapter is presented under the following scheme:

4.2 A discussion of the previous work on Cr^{2+} in MgO, showing the reasons for the current experiments.

4.3 A brief description of the theory of Ham, and its implications.

4.4 Experiments on 'as received' samples.

4.5 Annealing treatments and their effects. A brief description of the ideas behind annealing.

4.6 Experiments on annealed samples, using both stressing systems.

4.7 Discussions and conclusions.

4.2 Previous Work on Cr^{2+} in MgO

(4.2(i))

The present line of research, that of considering the effects of an externally applied, uniaxial, static stress on the apr of Cr^{2+} in MgO was suggested by the results of Marshall (1967) and Marshall and Rampton (1968). It was postulated that random lattice strains were of small size, being due to crystal defects far removed from the impurity ion. The directions of these strains were also random. A large uniaxial strain should, therefore, have the effect of dominating the random lattice strains at a chromous ion site. It was predicted by Marshall that very few of the chromous ions contribute to the observed absorption, since only ions strained along the [100] directions should be included. When a large uniaxial stress is applied the resultant strain at an impurity site will be along the direction of application. If this direction is <100>, and the magnitude of the resultant strain is sufficient to dominate the random lattice strains, then such an ion will contribute to the observed resonance. Hence Marshall's expectations were that an externally applied stress lined up on the <100> direction should result in a large increase in the number of contributing ions, and thus in a much larger absorption peak. He chose to apply his stress by means of a brass clamp constraining the crystal in the required direction. Upon cooling to 4.2K the brass contracts far more than the MgO, and a large stress is produced. The magnitude of such a stress could not be accurately predicted, but it was arranged to be just less than that required to break the crystal, when at its maximum value. The results of such experiments did not follow the expectations. Marshall observed that an increase inthe area of the absorption peak of order 2 to 3 times was produced, and that this same result was obtained for different large values of stress.

Such a result is consistent with a situation where $^1/_3$ of the chromous ions are aligned with each [100] axis, suggesting a static Jahn-Teller effect constrained to that <100> axis along which the largest component of the random lattice strain is acting. The current theories (those of Ham (1971), and Fletcher and Stevens (1969)) have to allow for each ion to show symmetry about one of the [100] axes, whilst still being subject to a dynamic form of Jahn-Teller effect, as the unstrained Cr^{2+} in MgO spectrum observed by Marshall gives results which can only be fitted to a dynamic theoretical prediction. The present work allows for strains of much lower magnitude than those produced by the Marshall experiments but aligned along a similar crystal axis, to be employed. These strains are of the order of the magnitude of the random lattice strain component along the chosen direction. In such a situation the random strain distribution at an ion is not dominated by the impressed stress effect, but the centre of the distribution can be moved. A fuller description of this is given in section 4.3.

4.2(ii)

The work of King et al (1976), showed that Cr^{2+} in MgO exhibited a large thermal relaxation peak centred on 6K. The shape and magnitude of this peak was such that cooling to below 2K reduced the effect of acoustic absorption by non-resonant mechanisms to a sufficiently low level for phonons to travel through the sample and undergo detectable resonant absorption. King also investigated the effect of sample annealing on this peak and observed it to be much reduced by a hydrogen atmosphere anneal at 1300°C. Confirmation, of a qualitative nature, of King's results could be carried out by observing at what temperature phonons were able to travel through the sample and be reflected back, (i.e. at what temperature

sample echos appeared), and how further cooling affected the magnitude of these echos for samples under different annealing conditions

4.2(iii)

Lange (1976) fitted the theoretical energy levels of Cr^{2+} in MgO to the results of his experiments into the temperature dependence of the APR of Cr^{2+} in MgO. This fit gives values for the Jahn-Teller Tunneling splitting (3Γ) and spin-orbit splitting (K) appropriate to the system. A discussion of the values obtained, by Lange and by other workers, is included in section 4.3(ix), where the spread of values of these parameters measured experimentally, and the relevence of this tothe theoretical interpretation, is discussed. Lange's values showed that $3\Gamma >> K$, i.e. that the Jahn-Teller effect is well into the dynamic region, and that the energy level diagram thus produced was consistent with other experimental observations of Cr^{2+} in MgO. Further to this, Lange considered the anisotropy of direction, as had previously been considered by Marshall (1967). For longitudinal phonons the results of Marshall and Lange agree, with the exception that Lange gives the effective g_{11} as 1.3 whereas Marshall puts g_{11} in the range $0.9 \rightarrow 1.15$. This difference may be attributed to the strong local strain dependence of g_{11} (see section 4.3(vi)), and thus the strong sample dependence of g_{11}. Lange is able to interpret the observed anisotropy in terms of a combination of tetragonal and orthorhombic strains acting at the site, on the Ham model (section 4.3). The anisotropy observed when transverse mode phonons are used cannot, however, be interpreted in terms of such a strain combination, or in terms of a pure tetragonal (Fletcher and Stevens) strain. Lange concludes that the peak anisotropy observed for transverse

phonons results from a case where the tetragonal (e_θ) distortion at the site is less than the orthorhombic (e_ϵ) distortion.

The value of Lange's work to the present investigation lies both in the good agreement between the experimental results for longitudinal phonons obtained by Marshall (1967) and Lange, and in the calculation of values for 3Γ and K for cases where the impurity ion undergoes both compression ($\beta<o$) and extension ($\beta>o$) along the tetragonal axis, which may be compared with similar values obtained by other methods when attempting a theoretical interpretation of the present results.

4.3 Theoretical Interpretation of the APR Spectrum

As mentioned in section 4.1 above, this section will present a detailed account of the interpretation given by Ham (1971), including, in section 4.3(viii), below, Ham's own discussion of the fit of this interpretation to the 1968 results of Marshall and Rampton, and his choice of parameters in obtaining this fit. In section 4.3(ix), however, a range of values for these parameters obtained experimentally by a number of methods is given, and the implications of these results on the Ham interpretation is discussed. The interpretation due to Fletcher and Stevens (1969) is not given in detail, since it bears many points of similarity to that of Ham. Both interpretations rely on a cluster model, and both find that only ions undergoing tetragonal distortions can contribute to the APR spectrum. Ham (1971) points out that his interpretation may be considered as an extension to that of Fletcher and Stevens, in that he includes into the model non-tetragonal (orthorhombic) strains, and is able to account for the apparent selection of the tetragonally distorted sites by the longitudinal phonon. The major differences between the models are the choice of strictly

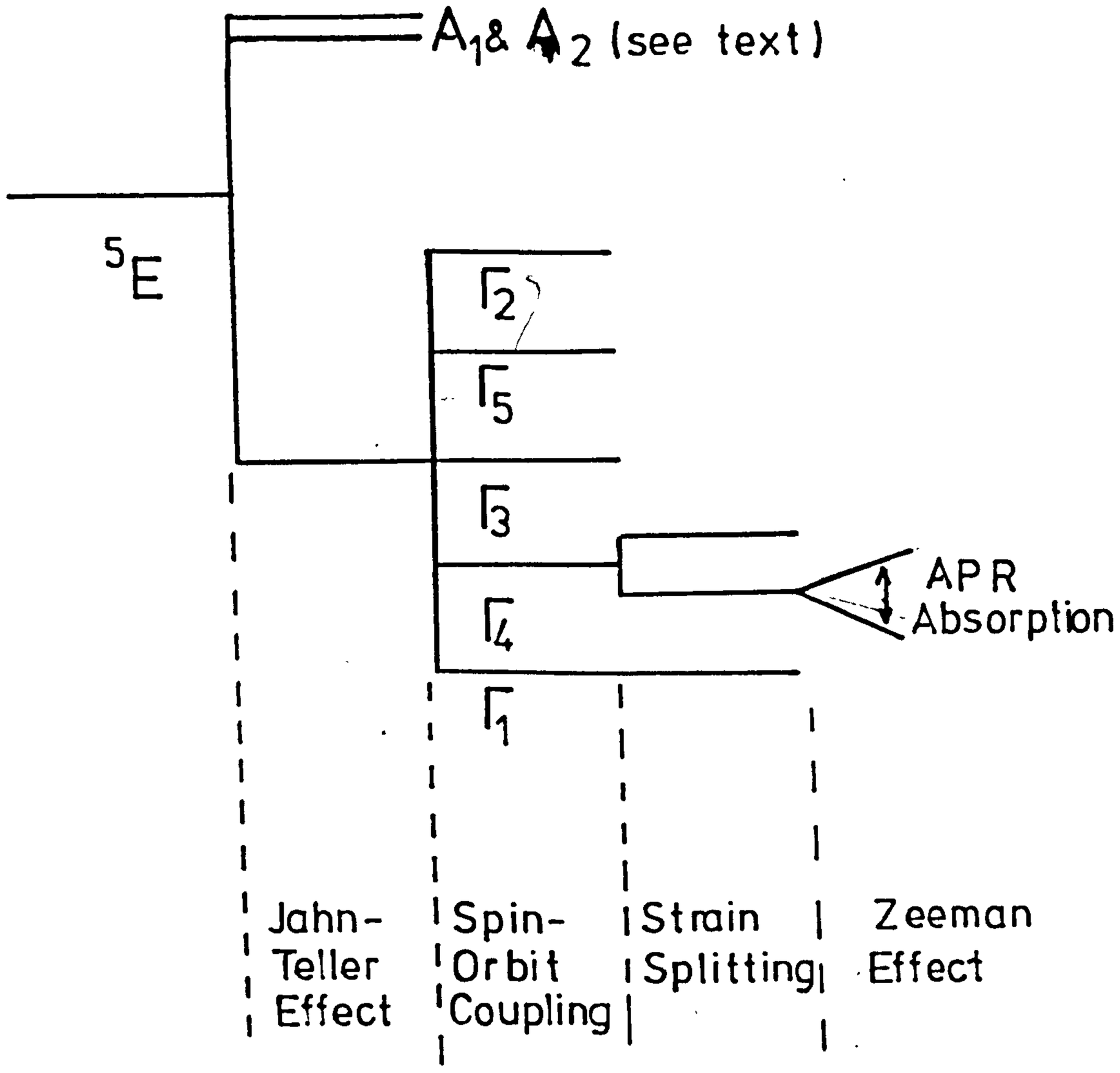

FIG 4.3.(i) LOW-LYING ENERGY LEVELS OF Cr^{2+} IN MgO [Schematic]

tetragonal strains (Fletcher and Stevens) as opposed to random strains (Ham) and the choice of values for the various parameters. Section 4.3(ix), in which the choice of parameters is considered, also contains a comparison of the choices of parameters made by Fletcher and Stevens, and Ham.

4.3(i) Basic Hamiltonian

Ham (1971) uses the model of an orbital electronic doublet state belonging to he irreducible representation E of the rotation group O of the cube, coupling with a pair of vibrational modes $Q\theta$, Q_ε also belonging to E. Although this model is a simplification of the actual situation (where the coupling between the ion and the crystal is via the entire range of lattice phonons as well as to any local vibration modes), it has been extensively justified by Ham in previous papers (referred to in Ham 1971) given the assumptions that spin-orbit levels close to the ground state are considered and that the strongly coupling phonons have energies appreciably higher than the excitation energies of the spin-orbit levels. It is noted that, for strong coupling, $Q\theta$ and Q_ε effectively produce displacements of the impurity ion ligands. The cluster mode produced is a linear combination of normal crystal modes, the strong Jahn-Teller coupling has the effect of selecting this combination such that the J-T coupling is maximised. This situation corresponds to the strong coupling, cluster model used by Fletcher and Stevens (1969).

The basic Hamiltonian of this model is

$$\mathcal{H} = \mathcal{H}_0 + \mathcal{H}_{JT} + \mathcal{H}_W$$

where:

$$\mathcal{H}_0 = \tfrac{1}{2}(2\mu)^{-1}[P_\theta^2 + P_\varepsilon^2 + (\mu\omega)^2(Q_\theta^2 + Q_\varepsilon^2)]$$

describes the elastic and kinetic energies of the vibrational modes

$$\mathcal{H}_{JT} \; (= V(Q_\theta U_\theta + Q_\epsilon U_\epsilon))$$

describes the linear J-T coupling of the electronic orbital doublet From this term a value for the linear Jahn-Teller energy can be obtained. This value is $E_{JT} = V^2/2\mu\omega^2$, where V is the Jahn-Teller coupling constant. If we consider Q-space such that $Q\theta = \rho \cos\Theta$ and $Q_\varepsilon = \rho \sin\Theta$, then E_{JT} describes a circle in Q-space of radius $\rho = |V|/\mu\omega = \rho_o$.

$\mathcal{H}_\omega$ describes the higher-order coupling which operates in cubic symmetry. Treated as a small perturbation on $\mathcal{H}_{JT}$, the effect of $\mathcal{H}_w$ is to change the energy of the basic Hamiltonian in a way which depends on the sign of V. This removes the rotational symmetry which existed for linear coupling as a function of θ, and, instead, selects three minimum energy ion figurations from the infinite number possible for linear coupling.

The ground state of the vibronic Hamiltonian is a ^5E-state. The linear J-T coupling gives a first excited state which is an accidentally degenerate doublet $(A_1 + A_2)$, where the energy of this level, Δ_1, is given, by Ham (1971), in a reference to an earlier paper, by $\hbar\omega\,(4E_{JT}/\hbar\omega)^{-1}$. $\mathcal{H}_w$ has the effect of lifting the degeneracy of the $(A_1 + A_2)$ state, such that the lower resulting singlet approaches the ground state doublet assymptotically as $\mathcal{H}_w$ increases, which of the resulting singlets has the lower energy is determined by the relative signs of V and $\mathcal{H}_w$. If $\mathcal{H}_w$ is defined as $-\beta\cos 3\theta$, where $\beta = -(\mp Vq\rho_o^2 + Vc\rho_o^3)$ for $V \lessgtr 0$, then for V and β of the same A_1 is the lower and for V and β of opposite sign A_2 is the lower (Vq and Vc are coupling constants for the higher order coupling).

4.3(ii) Spin-Orbit Coupling

The effect of spin-orbit coupling is to lift the spin-degeneracy of the orbital doublet ground state, resulting in five equally spaced levels, the separation of the levels being K. The effect of the Jahn-Teller coupling, ignoring spin-orbit coupling to the first excited state, is to reduce the separation of five levels to K', where $K' = qK$ (q is a constant). If the separation of the first excited level from the ground state (defined as 3Γ) is not large compared with the spin-orbit splitting (4K), then spin-orbit coupling to the excited states must be considered. The effect of this is to introduce two new spin-orbit levels (provided only the lower excited singlet interacts), the particular levels being introduced depending upon which excited singlet is lower. Such a situation is similar to that of the strong-coupling, cluster model of Fletcher and Stevens. As the spin-orbit splitting, K', tends to become larger that 3Γ (i.e. $3\Gamma/K' \to o$), then the situation tends to be than of a Static Jahn-Teller effect. In this case phonons cannot induce transitions between the spin-levels to a first approximation, and, thus, the APR absorption would be very small.

4.3(iii) Zeeman Splitting

An applied magnetic field can only split the Γ_4 and Γ_5 triplet levels resulting from spin-orbit coupling, the Γ_1 and Γ_2 singlets and Γ_3 doublet being unaffected to first order. The resulting splitting is given by

$$\mathcal{H}_{gH} = g\mu_B(\underline{g}'.\underline{H})$$

where μ_B is the Bohr Magneton, $\underline{H}$ is the applied field, g is the g-value of the particular triplet and $\underline{g}'$ is an effective spin operator, of magnitude 1, operating within the particular triplet.

These g-values can be related to the spin-orbit level splittings by considering the general form of a Zeeman interaction for a ^5E state, i.e.

$$\mathcal{H}_H = g_1/\mu_B (\underline{S}.\underline{H})\vartheta + \frac{1}{2} g_2/\mu_B ([3S_z H_z - (\underline{S}.\underline{H})]U_\theta + \sqrt{3}[S_x H_x - S_y H_y]U_\epsilon)$$

where g_1 and g_2 are given to first order from the spin-orbit interaction by

$$g_1 = 2 - 4\lambda/\Delta$$

$$g_2 = -4\lambda/\Delta$$

λ is the spin-orbit coupling constant,

Δ is the cubic-field splitting.

If the lower excited singlet is A_1, then for

$$\Gamma_4 \quad : g = \frac{1}{2} g_1 - q g_2$$

$$\Gamma_5(\text{lower}): g = \frac{1}{2} g_1 (1 - 3\sin^2\beta_1) + q g_2 \cos^2\beta_1 - r g_2 \sin\beta_1 \cos\beta_1$$

$$\Gamma_5(\text{upper}): g = -g_1 (1 - 3/2 \sin^2\beta_1) + q g_2 \sin^2\beta_1 + r g_2 \sin\beta_1 \cos\beta_1$$

where

$$\tan 2\beta_1 = -2rK/(3\Gamma - K')$$

If the lower singlet is A_2, then for

$$\Gamma_5 \quad : g = \frac{1}{2} g_1 + q g_2$$

$$\Gamma_4(\text{lower}): g = \frac{1}{2} g_1 (1 - 3\sin^2\beta_2) - q g_2 \cos^2\beta_2 - r g_2 \sin\beta_2 \cos\beta_2$$

$$\Gamma_4(\text{upper}): g = -g (1 - 3/2 \sin^2\beta_2) - q g_2 \sin^2\beta_2 + r g_2 \sin\beta_2 \cos\beta_2$$

where

$$\tan 2\beta_2 = -2rK/(3\Gamma + K')$$

These expressions for the g-values of the triplet-levels agree with those obtained by Fletcher and Stevens.

4.3(iv) Strain Splitting

We define the strain in the crystal in terms of strains along the crystal directions x, y, and z. Thus strains e_{xx}, e_{xy}, e_{yy}, e_{xz}, e_{yz}, e_{zz} are produced. Of these, only the strains which act along the crystal directions can affect an E-state doublet, since these transform as E, thus only e_{xx}, e_{yy} and e_{zz} need be considered. In terms of the directions θ and ε defined for Q, then

$$e_\theta = e_{zz} - \frac{1}{2}(e_{xx} + e_{yy})$$

$$e_\varepsilon = \frac{3}{2}(e_{xx} - e_{yy})$$

The strain Hamiltonian can then be written

$$\mathcal{H}_S = V_2(e_\theta U_\theta + e_\varepsilon U_\varepsilon)$$

where V_2 is the strain coupling constant.

There are two ways of considering the effect of strain on the system: firstly, the Hamiltonian due to strain can be considered as directly altering the energy levels of the vibronic Hamiltonian (due to crystal distortions), or secondly as moving the equilibrium position of the modes $Q\theta$, $Q\varepsilon$ from $Q_o\theta = Q_o\varepsilon = 0$ to new values of $Q_o\theta = De_\theta$, $Q_o\varepsilon = De_\varepsilon$, where D is some constant. It can be shown that if $V_2 = DV$ (where V is the JT coupling constant), then these two systems are equivalent. In terms of the Γ_4 and Γ_5 triplets in which we are interested

$$\mathcal{H}_S(\Gamma_i) = V_S[E'_\theta e_\theta + E'_\varepsilon e'_\varepsilon]$$

where E'θ and E'ε are operators defined in terms of the triplet wavefunctions. This leads to strain coupling constants Vs, for the

A_1 singlet lower, Γ_4 : $V_S = -qV_2$

(lower) Γ_5 : $V_S = qV_2\cos^2\beta_1 + 2rV_2\sin\beta_1\cos\beta_1$

(upper) Γ_5 : $V_S = qV_2\sin^2\beta_1 - 2rV_2\sin\beta_1\cos\beta_1$

and for the A_2 singlet lower:

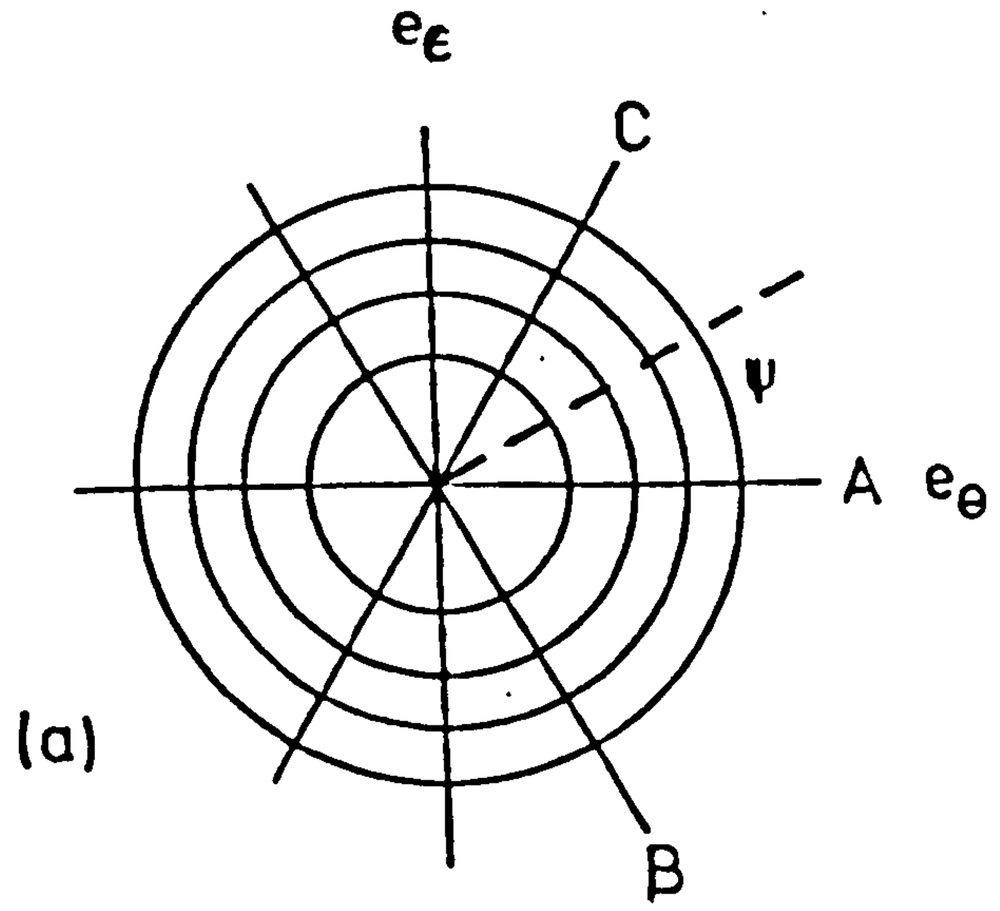

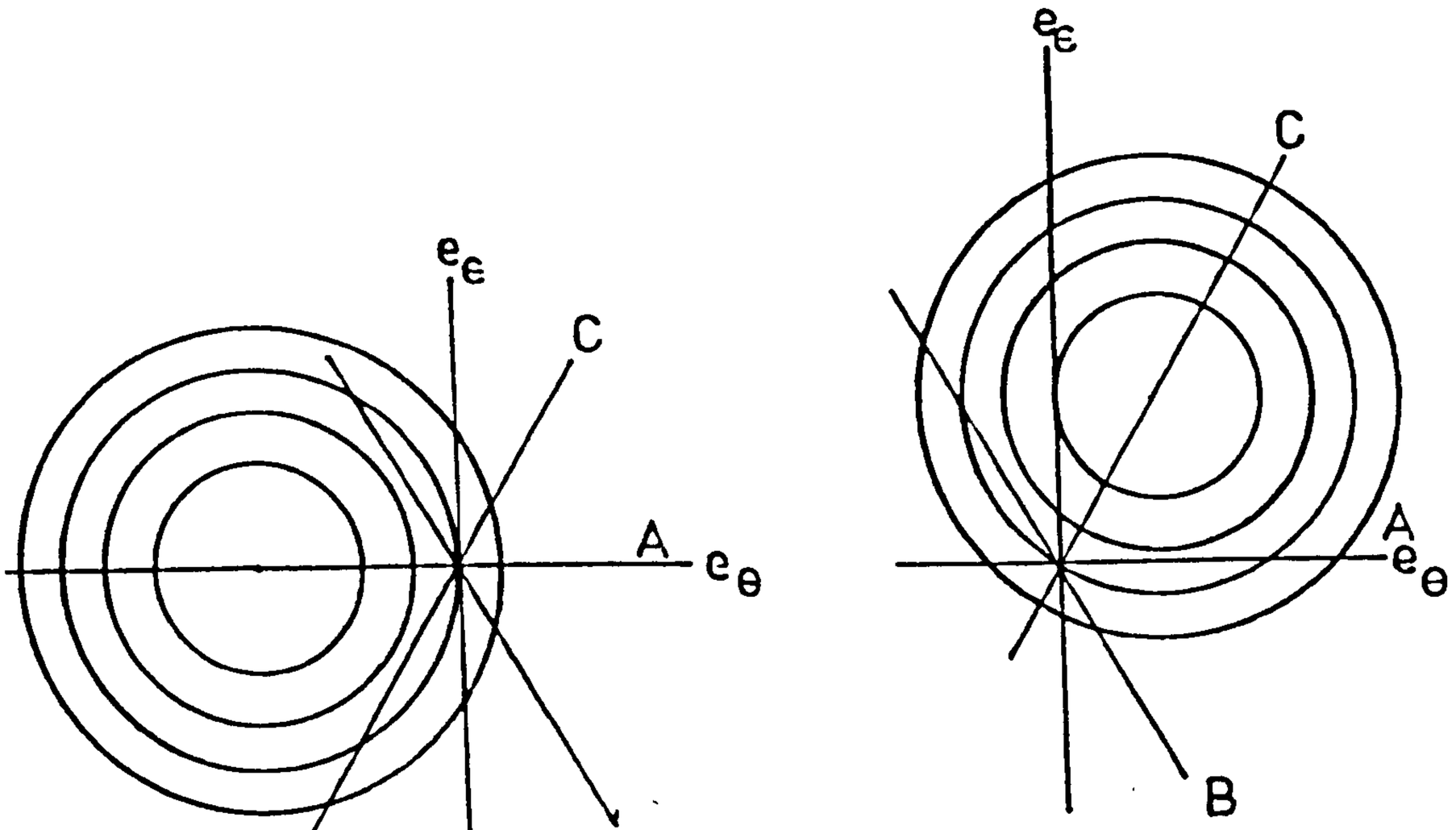

FIG 4.3.(ii). Contours of equal probability for a random local strain distribution at a Cr^{2+} site in MgO

(a) No externally applied stress

(b) Random strain + uniform compression along [001]

(c) Random strain + uniform compression along [010]

Lines A B & C are the loci of points with tetragonal local strain symmetry with respect to the [001], [100] and [010] axes, respectively. (After HAM, 1971)

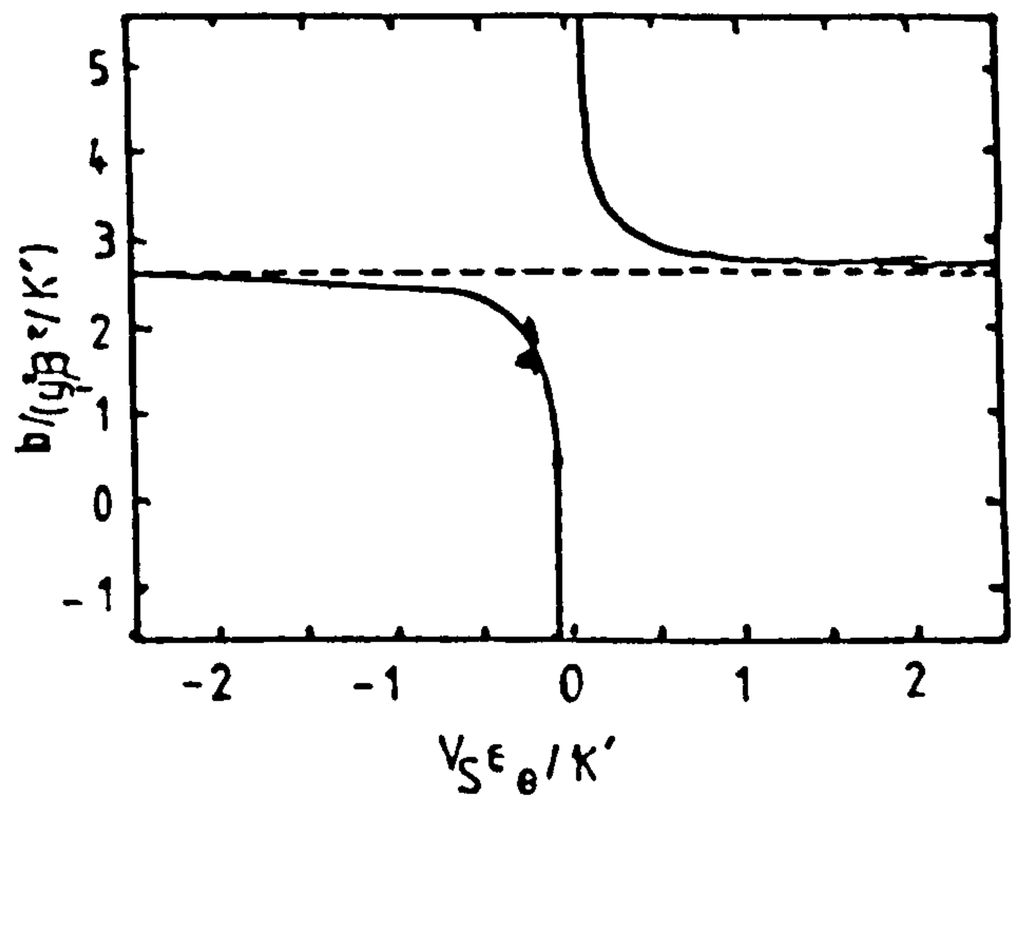

(a)

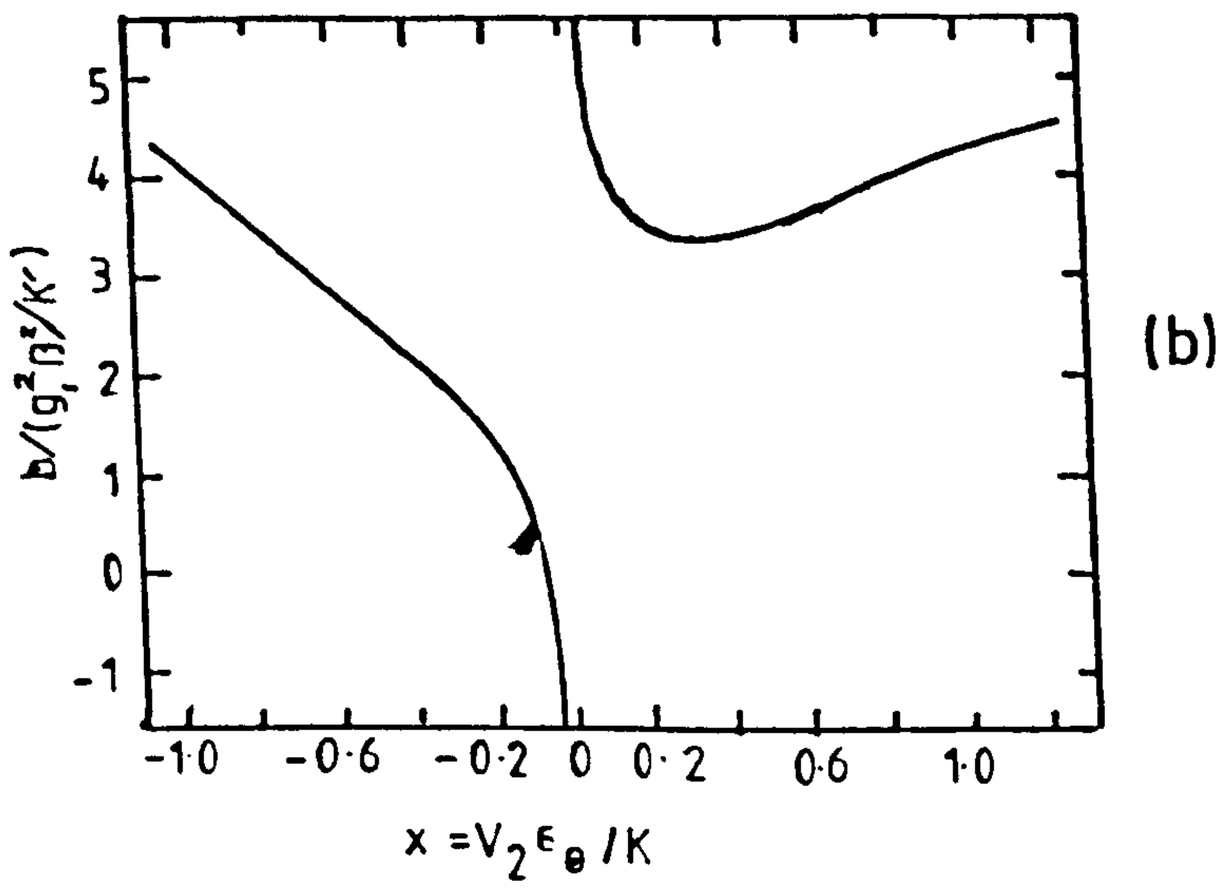

(b)

FIG 4.3(iii). Value of the parameter b for the lowest Γ_4 triplet level of the ^5E state of Cr^{2+} in MgO as a function of tetragonal strain.
(a) Neglecting, and (b) Including, strain mixing of the spin-orbit levels. (After Ham, 1971)

$$\Gamma_5(\text{lower}):\quad V_s = -qV_2\cos^2\beta_2 + 2rV_2\sin\beta_2\cos\beta_2$$

$$\Gamma_4(\text{upper}):\quad V_s = -qV_2\sin^2\beta_1 - 2rV_2\sin\beta_2\cos\beta_2$$

4.3(v) General Expectations for the APR Spectrum

As a start to considering what sort of APR spectrum may be expected to result from the energy system described above, certain assumptions may be made. Firstly, one can assume that the probability distribution of e_θ, e_ε is of the form of Figure 4.3(ii), if there is no externally applied stress and if e_θ, e_ε are taken to vary at random over the chromium sites. Although there is no reason for this distribution to be independent of angle in the plane of the diagram (defined as ψ, where $e_\theta = (e_\theta^2 + e_\varepsilon^2)^{1/2}\cos\psi$, $e_\varepsilon = (e_\theta^2 + e_\varepsilon^2)^{1/2}\sin\psi$), symmetry considerations limit the distribution to being invariant under 3-fold axial rotation (i.e. $\pm\,{}^2/_3\,\bar{\pi}$) and symmetric in reflection about the e_0 axis ($\psi \rightarrow -\psi$). Secondly, one may assume that the typical strain splitting of a Γ_4 or Γ_5 triplet is large c.f. the typical APR phonon energy of $\sim$0.3 cm^{-1}, implying that phonons can only induce transitions in triplets subject to strains smaller than the norm. For the purposes of this discussion we will also assume that no strain coupling between the different spin-orbit levels occurs. (This assumption will later be removed). It is important to note that only ions for which the values of e_θ, e_ε are close to the lines A, B and C)Figure 4.3(ii)), such that the separation of two of the levels are the triplet are separated by order of $h\nu$, will resonant absorption be possible. These ions are only a small proportion of the total impurity concentration, since e_θ, e_ε are typically random. If e_θ, e_ε do lie near to A, B or C, then the

site distortion is nearly tetragonal (whereas for typical e_θ, e_ε orthorhombic symmetry exists), and for typical e_θ, e_ε the separation of the triplet levels is greater than $h\nu$, making resonance impossible. If e_θ, e_ε are in sets A, B, C, and close to zero then all three triplet levels fall close together. Due to the random nature of e_θ, e_ε, such ions constitute a negligibly small faction of the total impurity concentration. Since absorption is stated to occur between the Zeeman-split states of the doublet, and the line shape of the absorption is highly anisotropic, a consideration of the effect of magnetic fields on the states of the doublet must be carried out. Let us consider ions which lie close to the line A (Figure 4.3(ii)), i.e. those for which e_θ is typically large compared with e_ε. Considering the equation

$$\mathcal{H}_{s[\Gamma_i]} = V_s[\mathcal{E}'_\theta e_\theta + \mathcal{E}'_\epsilon e_\epsilon]$$

then, $\mathcal{E}'_\epsilon e_\theta$ can be considered as negligable. The separation of the singlet $\Gamma_4 z$ from the average energy of the doublet $\Gamma_4 x$, $\Gamma_4 y$ can be shown to be

$$W = -\frac{3}{2} V_s e_\theta$$

We have to consider linear Zeeman splitting of the doublet $\Gamma_4 x$, $\Gamma_4 y$, the coupling, in H^2, allowed by cubic symmetry between the Γ_4 triplet and the other spin-orbit levels of the ^5E state, and the coupling between the doublet and the $\Gamma_4 z$ level, considered as a perturbation.

In the production of the effective Hamiltonian of this system, Ham considers only those terms which affect the splitting of the doublet neglecting those which move the centre of energy of the system.

$$\mathcal{H}_{eff} = g\mu_\beta \sigma_2 H_z + [a(H_x^2 - H_y^2) - \tfrac{1}{2}\sqrt{3} V_s e_\epsilon]\sigma_3 + b\sigma_1 H_x H_y$$

(linear Zeeman) (coupling to other S-O levels) (coupling to $\Gamma_4 z$)

where

$$\sigma_1 = |\Gamma_4 x\rangle\langle\Gamma_4 y| + |\Gamma_4 y\rangle\langle\Gamma_4 x|$$

$$\sigma_2 = -i|\Gamma_4 x\rangle\langle\Gamma_4 y| + i|\Gamma_4 y\rangle\langle\Gamma_4 x|$$

$$\sigma_3 = |\Gamma_4 x\rangle\langle\Gamma_4 y| - |\Gamma_4 y\rangle\langle\Gamma_4 x|$$

and $a = \frac{1}{2}(g^2\mu_B^2/W) + \frac{3}{2}a'$ (a' constant)

$b = (g^2\mu_B^2/W) + b'$ (b' constant)

(a' and b' are constants related to the H^2 coupling)

This Hamiltonian has eigenvalues

$$\Delta_E = [(\sqrt{3}V_s e_\epsilon - 2a(H_x^2 - H_y^2))^2 + 4g^2\mu_B^2 H_z^2 + 4bH_x^2 H_y^2]^{1/2}$$

The minimum value of ΔE as a function of e_ϵ is thus

$$\Delta E_{min} = [4g^2\mu_B^2 H_z^2 + 4bH_x^2 H_y^2]^{1/2}$$

for the condition

$$\sqrt{3}V_s e_\epsilon = 2a(H_x^2 - H_y^2)$$

In the system of APR experiments, a longitudinal phonon of energy $h\nu$ along the [100] axis is used, causing a strain modulation at the impurity ion sites of

$$\left.\begin{aligned} \delta e_\theta &= S\cos(2\pi\nu t) \\ \delta e_\epsilon &= -\sqrt{3}S\cos(2\pi\nu t) \end{aligned}\right\} \text{--------A}$$

For zero magnetic field the phonon cannot induce transitions between $\Gamma_4 x$ and $\Gamma_4 y$, since the matrix elements of the perturbations 'A' with respect to the strain Hamiltonian $\mathcal{H}_S$ are diagonal only, but as field is applied the states are mixed through the σ_1 and σ_2 terms of $\mathcal{H}_{eff}$, and transitions are possible if the resonance condition $h\nu = \Delta E$ is satisfied.

The diagonal matrix elements of 'A' with respect to $\mathcal{H}_S$ are

$$\left.\begin{aligned} \langle\Gamma_4 x|\mathcal{H}_S|\Gamma_4 x\rangle &= 2V_s S\cos(2\pi\nu t) \\ \langle\Gamma_4 y|\mathcal{H}_S|\Gamma_4 y\rangle &= -V_s S\cos(2\pi\nu t) \end{aligned}\right\} \text{-------B}$$

Ham calculates the square of the acoustic matrix elements, B, between the eigenstates of $\mathcal{H}_{eff}$, and obtains a result proportional to

$$M^2 = V_S^2 S^2 (g^2 \mu_B^2 H_Z^2 + b^2 H_X^2 H_Y^2) / (\Delta E)^2$$

For fixed ΔE this value increases as H^2 or H^4. Thus the absorption increases with increasing H. A further contributing factor to the absorption lineshape is the probability per unit energy that ΔE satisfies the resonance condition. Ham uses this factor to weight M^2 and concludes that the resonance absorption is of the form

$$G(H,\nu) = \int_c \frac{M^2 p(e_\theta, e_\varepsilon) dS_e}{|\mathrm{grad}_e \Delta E|}$$

(where C = line $\Delta E = h\nu$ in the $(e_\theta, e_\varepsilon)$ plane).

$\mathrm{Grad}_e \Delta E$ is the gradient of ΔE with respect to e_θ, e_ε. Neglecting the dependence (via a and b) of ΔE on e_θ in the expression for ΔE (above) we obtain

$$\left[\frac{1}{|\mathrm{grad}_e \Delta E|}\right]_{\Delta E = h\nu} = \frac{\Delta E}{\sqrt{3}\,|V_S|\,(h^2\nu^2 - 4g^2\mu_B^2 H_Z^2 - 4b^2 H_X^2 H_Y^2)^{1/2}}$$

for $h\nu > \Delta E$ min.

Via the ΔE term, this factor also contributes to increasing the absorption with H, until ΔE min becomes greater than $h\nu$, when no further absorption is possible and a high-field edge occurs. This occurs for

$$h\nu = (4g^2\mu_B^2 H_Z^2 - 4b^2 H_X^2 H_Y^2)^{1/2}$$

In this treatment the dependence of ΔE on e_θ (via the energy denominator W in the parameter b) was neglected. Taking this into account the conclusion is that the full absorption spectrum is a

summation of many lines, each with a high field edge at a different field value, dependent upon the variation of e_θ within the range of the random strain distribution. If, however, the range of values of e_θ for which resonant absorption can take place is small, as in this case, then the broadening of the line calculated above is small, and a sharp high field edge still occurs.

We may conclude that the line shape contained is only weakly dependent on the form of the strain distribution provided that the parameter 'b' is not strongly dependent upon e_θ, and that the spread of zero-field splittings of the $|\Gamma_4 x\rangle$ and $|\Gamma_4 y\rangle$ levels (due to the spread of e_ε) is such that the only separations of comparable size to $h\nu$ correspond to values of e_ε lying close to the centre of the strain distribution, where $p(e_\theta, e_\varepsilon)$ is not strongly dependent on e_ε.

It remains to consider what absorption peaks may be expected from ions in sets B and C (Figure 4.3(ii)). In the case of set B, under the experimental conditions, no peaks occur since the set has its tetragonal axis along [100] and thus a longitudinal phonon along [100] affects $|\Gamma_4 y\rangle$ and $|\Gamma_4 z\rangle$ identically. For set C (axis along [010]) the absorption should be identical to that of set A with the roles of Hx, Hy, Hz suitably changed. This results in a peak at

$$h\nu = (4g^2\mu_B^2 H_y^2 + 4b^2 H_x^2 H_z^2)^{1/2}$$

To conclude a general analysis it is necessary to obtain values of a' and b'. For low magnetic fields, transitions only occur between the levels of the Γ_4 and Γ_5 triplets, since the Γ_1 Γ_2 &. Γ_3 levels are non-magnetic and are not mixed with the Γ_4 Γ_5 levels by the strain. At low temperatures only the lower triplet will be populated so it is for this level that the parameters should be calculated. We neglect coupling of the ^5E state to the A_1 or A_2 via spin-orbit coupling, giving (for the lower Γ_4 triplet)

$$a' = g_1^2/\mu_B^2 \left[\frac{2}{3\Delta_{\Gamma_4\Gamma_1}} - \frac{2}{3\Delta_{\Gamma_3\Gamma_4}} + \frac{1}{4\Delta_{\Gamma_5\Gamma_4}} \right]$$

where $\Delta_{\Gamma_i\Gamma_j} = E(\Gamma_i) - E(\Gamma_j)$

$$b' = g_1^2/\mu_B^2 \left[\frac{2}{\Delta_{\Gamma_4\Gamma_1}} + \frac{1}{\Delta_{\Gamma_3\Gamma_4}} - \frac{3}{4\Delta_{\Gamma_5\Gamma_4}} \right]$$

Note that for the case $3\Gamma \gg 4K$, $\Delta_{\Gamma_i\Gamma_j}$ is a constant if i, and j are adjacent levels, = qK = K'.

Hence for $3\Gamma \gg 4K$

$$a' = g_1^2/\mu_B^2 / 8K'$$

$$b' = 21 g_1^2/\mu_B^2 / 8K'$$

Similarly for the lowest Γ_5 triplet

$$a' = -g_1^2/\mu_B^2 \left[\frac{2}{3\Delta_{\Gamma_2\Gamma_5}} - \frac{2}{3\Delta_{\Gamma_5\Gamma_3}} + \frac{1}{4\Delta_{\Gamma_5\Gamma_4}} \right]$$

$$b = -g_1^2/\mu_B^2 \left[\frac{2}{\Delta_{\Gamma_2\Gamma_5}} + \frac{1}{\Delta_{\Gamma_5\Gamma_3}} - \frac{3}{4\Delta_{\Gamma_5\Gamma_4}} \right]$$

or for $3\Gamma \gg 4K$

$$a' = -g_1^2/\mu_B^2 / 8K'$$

$$b' = -21 g_1^2/\mu_B^2 / 8K'$$

4.3(vi) Effect of Strain Mixing on the APR Spectrum

In the above discussion, the mixing of the different spin-orbit levels by strain has been neglected. For the case of Cr^{2+} in MgO the estimation of the separation of the spin-orbit levels is $2cm^{-1}$ compared with an estimated strain-splitting of $1cm^{-1}$, so it

is necessary to take level mixing by strain into account.

The effect of this mixing is to cause the parameters a, b and g, in the above treatment, to depend on strain in a more complicated way than has been previously assumed.

Using the expression

$$\mathcal{H}_S = V_2 (e_\theta \dot{U}_\theta + e_\epsilon U_\epsilon) \qquad \text{(section 4.3(iv))}$$

and considering only those ions in set A, for which e_ε is near to zero, and may be neglected, Ham calculates a, b and g for the doublet derived from the lowest Γ_4 triplet level. Assuming that $3r \gg k'$ (such that coupling between the ^5E levels only need be considered), the expressions obtained for g is

$$g = g_1 (1+2x) [(2+x)^2 + 3x^2)^{-\frac{1}{2}}$$

where $x = q V_2 e_\theta / K \quad [= V_2 e_\theta / K \;]$ and g_2 is neglected.

The result for b is a complex function shown in Figure 4.3(iii). Clearly both g and b may be expected to vary significantly as a function of the strain. A peak which has position determined mainly by g and would be greatly broadened by a strain distribution giving x in the range $-\frac{1}{2}$ to $+\frac{1}{2}$, since this produces a range of g from 0 to ~1.5. Such a broadening may well mask the assymetry expected from the analysis of section 4.3(v). The effect of strain variation on b must be considered in two parts, $x > 0$ and $x < 0$. If $x < 0$, then ions corresponding to this should contribute to a broad absorption with no distinct edge (see Figure 4.3(iii)b). Since, however, for $x < 0$ the doublet derived from the lowest Γ_4 triplet lies above the remaining singlet, and has energy relative to the ground-state increasing with strain, then population of such a level is less likely at a few degrees Kelvin than the lower lying doublet corresponding to

$x > 0$. The Boltzman distribution, then, favours absorption occurring between the levels of a doublet corresponding to $x > 0$, which is both below the singlet and close to the ground state. For $x > 0$, b has a minimum value given by

$$b_{min} = 3 \cdot 4 [g_{\perp}^2 / \mu_B^2 / K']$$

Therefore, ions which have $x > 0$ and contributing to a peak mainly dependent on b should exhibit an absorption peak with a high-field edge at a field corresponding to b_{min}. The position of this edge will be independent of the shape of the strain distribution for $b > b_{min}$.

This peak is thus qualitatively of the form given in section 4.3(v), but with the high-field edge at a value given by b_{min}.

4.3(vii) Effect of Applied Uniaxial Stress

An applied uniaxial stress may be considered as producing a fixed uniaxial strain distribution superimposed directly onto the random strain distribution present in the lattice. The result of this is simply to displace the random distribution of Figure (ii) (a)) along a corresponding e_θ, e_ε axis. A compression along [001] (used in these experiments) moves the distribution in the way shown in Figure 4.3(ii) (b)), whilst a compression along [010] moves it to that shown in Figure 4.3(ii) (c)). The expected resonance spectrum is still obtained by the analysis given in sections 4.3(v) and 4.3(vi), except that the displaced distribution must now be considered in pace of the random distribution. The value of g for ions having $e_\varepsilon \underset{\sim}{\nu} 0$ (set A) changes with the value of e_θ (along line A), hence a uniaxial strain which moves the centre of the strain distribution with respect to line A will produce a change in g-value. A resonance absorption with its position mainly determined by g will thus shift with applied stress. The value of b_{min} is not, however, dependent

strongly on strain, so the position of the high-field edge should not change. As the strain distribution is smooth aroung the extremum and extends well beyond it, strains applied to move the distribution will not effect the intensity of the peak until they are larger than the mean value of the random strain, when the intensity of the peak will be decreased, corresponding to the distribution being shifted away from the extremum.

If a {001} uniaxial stress is applied and the random distribution changed to that of Figure 4.3(ii) (b)), then the diameter of the displaced distribution is still line A, but not lines B or C. The number of ions of sets B and C able to satisfy the resonance condition is thus reduced compared to those in set A, and thus the intensity of an absorption peak due to set B or set C will reduce with respect to those due to set A. The intensities are further affected by the way the applied stress affects the Boltzman factor for the contributing doublet in each set. If the population is reduced with applied stress, the intensity of the corresponding absorption peak is reduced, and vice versa.

An interesting point of comparison exists here between the theories of Ham and of Fletcher and Stevens. The latter assumed a stress distribution strictly tetragonal along lines A, B and C (Figure 4.3(ii) (a)). For such a case an applied stress along {001} would move the ions in sets B and C away from lines B and C such that their zero-field-splitting is greater than $h\nu$ and they cannot contribute to resonant absorption. The effect is to reduce the symmetry of these ions to orthorhombic and to increase the zero-field splitting. The treatment given in this section can therefore explain the change in APR spectrum even if the strain distribution is strictly tetragonal as assumed by Fletcher and Stevens and not

random as assumed by Ham. It should be noted, however, that our treatment would predict that the intensity of absorption peaks due to ions in sets B and C should be reduced far more quickly as a function of applied stress for tetragonal symmetry than for a random distribution.

4.3(viii) Application to the Marshall-Rampton Spectrum.

To test the validity of the above interpretation, the various predictions of the theory must be compared with the observations of Marshall and Rampton. The geometry of these experiments was identical to that of the present experiment, i.e

$$Hx = H \cos\theta$$
$$Hy = H \sin\theta \cos\phi$$
$$Hz = H \sin\theta \sin\phi$$

x = [100] = phonon propagatron direction.

Two resonance lines were observed, which were attributed to a transition within a doublet level for two sets of ions, one aligned along [001] and one along [010]. Temperature dependence experiments suggested that the doublet was a few cm^{-1} above the ground state singlet. One of the lines (called line C) showed a dependence on the angle of magnetic field:

$$H = h\nu / g_{\parallel} \mu_B \sin\theta \qquad (\phi = 0)$$

and the other (line U)

$$H = H'' / (\sin 2\theta)^{1/2}$$

where H'' = resonant field minimum of line U.

The spectrum observed in the present experiments bears a close resemblance to that observed by Marshall and Rampton. Before any interpretation of present data using Ham's model can be made, it is therefore important to see how well this model can explain the previous spectrum.

Comparing line C with the prediction for angular dependence of the absorption due to ions in set C (section 4.3(v)), we obtain good

agreement for $g = g_{11}/2$.

Line U agrees with the prediction for set A if $|b| = h\nu/(H'')^2$.

The line-shape, as predicted by the theory, is asymmetric with a sharp edge on the high-field side. This again agrees with the theory of section 4.3(v). Line U exhibits a much sharper high-field edge than line C. Since line C has a mainly g-dependent position, whilst that of line U is mainly b-dependent, the broadening of line C on the high-field side is consistent with the predictions of section 4.3(vi). This fact, in addition to the variation of the position of line C from sample to sample, indicates the strong strain dependence of g predicted in section 4.3(vi). The value of g_{11} obtained from the dependence on magnetic field angle of line C varied, over the range of samples, from 1.9 to 2.3. This predicts a g value for the triplet of 0.95 to 1.15. This agrees well with the prediction g = 1 for the lowest Γ_4 triplet (section 4.3(iii)). If the A_1 singlet is lower the value $g \sim 1$ ($g_2 \sim 0$) is obtained for all values of $3\Gamma/K$, whilst if the A_2 singlet is lower $g \sim 1$ is obtained for $3\Gamma/K \gg 2$.

It was observed that the position of line U was sample independent to $\pm$ 1%, giving an H'' value of 0.516T. It is predicted by the theory of section 4.3(vi) that if b has a broad extremum then the b-value will be nearly independent of local strain values. This prediction is borne out by the above observation. From the value of H'' (and hence of b) obtained, and using the expression for b_{min} given in section 4.3(vi) we can obtain an estimate for the spin-orbit splitting K'

$$K' \simeq 3{\cdot}4\,(g_{\perp}\mu_B H'')^2/h\nu = 2{\cdot}5\ \mathrm{cm}^{-1}$$

This value is thus an estimate of the separation between the spin-orbit levels in cubic-symmetry, if they are equally spaced, i.e. if $3\Gamma/K$ is large.

A further conclusion from this observation is that the value of x corresponding to b_{min} (x_{min} = 0.35) must fall within the strain distribution of all samples used in the experiments. From this it may be calculated that the typical strain splitting of the Γ_4 triplet is at least 1.2cm^{-1}. (Splitting $= \frac{3}{2}(qe_\theta V_2) = \frac{3}{2}K'x_{min}$)

The value of $K = 2.5cm^{-1}$ obtained by fitting Marshall and Rampton's data to Ham's theory agrees well with an approximate theoretical prediction of 2.1cm^{-1} and an experimental value of 2.24cm^{-1} obtained for Cr^{2+} in $CrSO_4 : 5H_2O$ (Griffith, 1961). Throughout the calculations it has been assumed that interaction between the ^5E states and the singlet A_1 or A_2 is negligable. There is no real reason to assume this. Ham cites the case of Cu^{2+} in MgO, a similar system to Cr^{2+} also undergoing a dynamic Jahn-Teller Effect, and giving a 3Γ value of about 10cm^{-1}. It is to be expected that the 3Γ value for Cr^{2+} in MgO should be of a similar or smaller size since the 3d orbitals of Cr^{2+} are more spacially extended than those of Cu^{2+}. If the effect of the singlet levels is considered, the estimate for K' should be slightly increased (still considering $3\Gamma / K >> 1$), as should the estimate of b' (and hence b_{min}).

Further experiments were performed by Marshall and Rampton to apply a uniaxial stress. When such a stress was applied along the [001](or Z) axis, line C became less intense, whilst line U very slightly intensified. This corresponds to the situation given in section 4.3(vii) and Figure 4.3(iii) (b)), where the distribution is moved along line A, reducing the number of set C ions capable of contributing to the resonance absorption, and hence the peak intensity. Line U increases, since U_2 is negative for Cr^{2+} and compression corresponds to $e_\theta < 0$, giving a positive value for x. Hence increasing strain

favours increasing population of the doublet. In an experiment applying stress along [010] (Y axis), line C increase in intensity and line U decreased. The g-shift of line C, in this case, and the fact that the line which is reduced in intensity stays at the same field is consistent with the model of Figure 4.3(iii). A further point to be noted from fitting the data is that the APR peak does not occur at $e_\varepsilon = 0$ (pure tetragonal distortion) but at a value of e_ε given by

$$\sqrt{3}V_s e_\varepsilon = 2a(H_x^2 - H_y^2) .$$

4.3(ix) Discussion.

The model described in detail above can be fitted to the experimental data of Marshall and Rampton (1968) very well by appropriate choice of parameters. As has been shown in section 4.3(viii), above, the line shape and g-value anisotropy of each of the APR absorption peaks can be quantitatively accounted for. The previous model of Fletcher and Stevens (1969), which varies from that of Ham primarily in the choice of strictly tetragonal strains, where Ham allows a random strain distribution, can also account quantitatively for the observed spectrum, given different choices of the parameters. Various experiments have been carried out on Cr^{2+} in MgO using many experiments methods. In addition to those of Marshall and Rampton, King and Oates, and Lange, described in section 4.2; Challis et al (1972) have investigated the system using thermal conductivity measurements, Patel and Wigmore (1977), using heat-pulses, Challis et al (1974) using Infra-red and Hasan, Murphy, King and Rampton (1978 private communication) using tunnel junctions. Each of these workers has fitted their results by appropriate choice of the parameters K and 3Γ. The values of K' (= $\frac{1}{3}$K) and 3Γ obtained by each of these experiments are shown in Table 4.3(i).

TABLE 4.3(i) VALUES OF THE PARAMETERS 3Γ and K'.

AUTHOR(S)	K′	3Γ
FLETCHER and STEVENS (1969)	$2\cdot02\,cm^{-1}$	$7\cdot6\,cm^{-1}$
HAM (1971)	$2\cdot5\,cm^{-1}$	"large"
CHALLIS et al (1972) (thermal conductivity)	$4\cdot0\,cm^{-1}$	$16\,cm^{-1}$
LANGE (1976) (A.P.R.)	$\beta<0$ $2\cdot4\,cm^{-1}$ $\beta>0$ $2\cdot2\,cm^{-1}$	$18\cdot5\,cm^{-1}$ $19\,cm^{-1}$
CHALLIS et al (1974) (infra red)	$4\cdot0\,cm^{-1}$	$16\,cm^{-1}$
PATEL and WIGMORE (1976) (heat pulses)	$2\cdot5\,cm^{-1}$	$32\,cm^{-1}$
HASAN et al (1978) (tunnel junctions)	$2\cdot4$ or $3\cdot7\rightarrow4\cdot2\,cm^{-1}$	

HAM	FLETCHER and STEVENS
$2q$	f_1
$2r$	$-f_2$
$K = 2K'$	D
3Γ	δ
$\underset{\sim}{U}_\theta$	$-2\underset{\sim}{T}_1$
$\underset{\sim}{U}_\epsilon$	$-2\underset{\sim}{T}_2$
V	$-\epsilon$ or $-C_1$
a	R
$(-\sqrt{3}/2)V_2$	aC_1
g_1	$2-4\mu$
g_2	4μ
$2g$	g_{11}
β_1	P_1
β_2	P_2
β	$-B$
μ	M_0
λ/Δ	μ

TABLE 4.3.(ii). EQUIVALENCE of SYMBOLS between the papers of HAM, and FLETCHER & STEVENS.

It may be seen that the resulting values fall into various fairly well defined sets

1. $K' = 2{\cdot}0$ to $2{\cdot}5\ cm^{-1}$

This value is supported by the greatest number of experimental fits. Ham's interpretation of the Marshall and Rampton data, and Fletcher and Stevens, both predict K' in this range, and the experiments of Lange, and Patel and Wigmore agree. Hasan, et al, are not able to discount this value although their results can be better interpretated by a larger value of K'.

(Note : Table 4.3(ii) shows the symbol equivalent of the Fletcher-Stevens and Ham papers. Most experimentalists have used the Fletcher-Stevens notation, but to remain consistent with sections 4.3(i) → (viii) the Ham notation is used here).

2. $K' = 3{\cdot}7$ to $4{\cdot}3\ cm^{-1}$

This value was first calculated by Challis, et al (1972). Hasan, et al, (1978) prefer to use K' in this range as a fit for their data, rather than to use the value of $2.4cm^{-1}$ which could give a fit. The only other data supporting this value is the Infra-red work of Challis et al (1974). No value is quoted in this paper but it is stated that the data does not contradict the K' = 4 estimate of the 1972 paper.

Lange (1976) points out, however, that his value of $2.2 \rightarrow 2.4cm^{-1}$ falls within the bounds established by Challis et al (1972). Most evidence would, therefore, seem to support the value of K' as falling between 2 and $2.5cm^{-1}$.

3. $3\Gamma = 7{\cdot}6\ cm^{-1}$

The Fletcher and Stevens fit of the Marshall and Rampton data gives a value for 3Γ of $7.6cm^{-1}$. Hence the ratio of 3Γ : K' is less that 4. This would imply that Ham is incorrect in assuming that the effect of the A_1 or A_2 singlet on the ^5E states is negligible.

This value is in agreement with the suggestion that 3Γ for Cr^{2+} in MgO should be slightly less than, but of the order of, that of Cu^{2+} in MgO, which is found to be about $10cm^{-1}$.

4. $3\Gamma = 16$ to $19\ cm^{-1}$.

This value has been obtained both by Challis, et al, (1972, 1974) and Lange. It is particularly interesting for two reasons:-

(i) Taken in conjunction with Challis' value of $K' = 4cm^{-1}$, the $3\Gamma / K'$ ratio of 4 is again obtained, in agreement with the Fletcher-Stevens model even though the actual values of 3Γ and K' are each about twice that estimated by Fletcher and Stevens from the Marshall-Rampton data. This supports the idea that the excited singlet must be considered, favours the Fletcher and Stevens choice of parameters (Ham says $3\Gamma / K' \gg 1$), but contradicts the Cu^{2+} in MgO value.

(ii) Taken in conjunction with Lange's value of $K' = 2.3cm^{-1}$, the $3\Gamma / K'$ ratio becomes about 8. This value inclines towards the Ham prediction of $3\Gamma / K' \gg 1$. It is interesting that Lange's value of $K' \underline{\sim} 2.3$ is close to both theoretical predictions, and that he obtains very similar sets of parameters both for $\beta < 0$ (compression) and $\beta > 0$ (extension).

5. $3\Gamma = 32\ cm^{-1}$

This value, obtained by Patel and Wigmore (1977), is particularly interesting in that, taken in conjunction with their value of $K' = 2.5cm^{-1}$, it shows remarkable agreement with Ham's predictions. The $3\Gamma / K'$ ration is of order 13, which would strongly support the suggestion that the A_1 or A_2 singlet had no effect on the ^5E states.

No experimentalist has, so far, been able to decide on the sign of β. Lange tries to fit his data with both cases, and finds a remarkable agreement between the parameters K' and 3Γ for each case. In his summary it is pointed out that the β < 0 (compression) case fits the data slightly better, agreeing with the Fletcher and Stevens model, but Lange is unable to reject the possibility of β > 0. Experiments carried out on related systems tend to prefer the Ham suggestion of β > 0 since this predicts the A_2 singlet as lower (Cu^{2+} : MgO), whereas Fletcher and Stevens predict the A_1 lower.

One interesting point that emerges is the prediction of the size of the strain splitting. Ham gives a value of $\sim 1cm^{-1}$, based on the Marshall-Rampton data. Lange, however, obtains a value of $0.2cm^{-1}$ for the strain splitting, and a value of the mean internal strain magnitude of 1×10^{-5}. Lange performs his calculation on the Marshall Rampton data and also obtains $0.2cm^{-1}$. This results from Lange's identification of the resonant absorptions taking place within the centre triplet of the split ^5E state, based upon his temperature dependence of APR results. It should be noted that Ham and Fletcher and Stevens predict that the absorptions occur within the lowest energy triplet of the split ^5E state, and the estimate of strain splitting = $1cm^{-1}$ is based upon this assumption.

Clearly it is not yet possible to decide on any set of parameters, or any value of β as being the generally recognised set. In the interpretation of the results in section 4.7 of this chapter it has been allowed, where possible, for various choices of parameters to be made,and for the predictions so produced to be compared.

4.4 Experiments on 'As Received Samples'

4.4(i) Introduction

A number of samples were prepared, as described in Chapter 2, from crystals of chromium doped MgO supplied by Professor L J Challis. The total chromium concentration within the samples was about 900 p p m. Experiments were carried out at temperatures below the lambda-point of the liquid helium, since at 4.2K the large thermal relaxation peak described in section 4.2(ii) prevented echos from being seen. The resonance spectrum was observed for various orientations of magnetic field, within the X-Y plane, and for zero applied stress, plus two values of uniaxially applied stress.

4.4(ii) Effect of Variation of Field Orientation

Figure 4.4(i) shows the spectrum obtained from sample Cr : MgO 1 for each of a number of values of field angle Θ , ranging from 0° to 90°. The spectrum is more complex than that obtained by Marshall and Rampton (1968), but lines corresponding to their 'U' and 'C' lines (see section 4.3) were identified, and these are labelled on the Figure. Figure 4.4(ii) shows the variation of the resonant field of these lines with field angle. It should be noted that it is the shape of these isofrequency curves for lines U and C that gave the lines their names. Lines F_1 and F_2 were identified from their g-values and the non-dependence of H_{res} on Θ as $\Delta ML = 1$ and $\Delta ML = 2$ transitions in the ferrous ion.

4.4(iii) Effect of Applied Stress

Stresses were applied by hanging masses from a lever system as described in Chapter 3, section 7 . Two values of mass were used, resulting in stresses in the $\{00\bar{1}\}$, (-z), direction on the sample of 3.4×10^6 kg/m^2 and 7×10^6 kg/m^2. The stresses correspond to strains in the lattice of $e_\theta = 8.34 \times 10^{-5}$ and 1.86×10^{-4} respect-

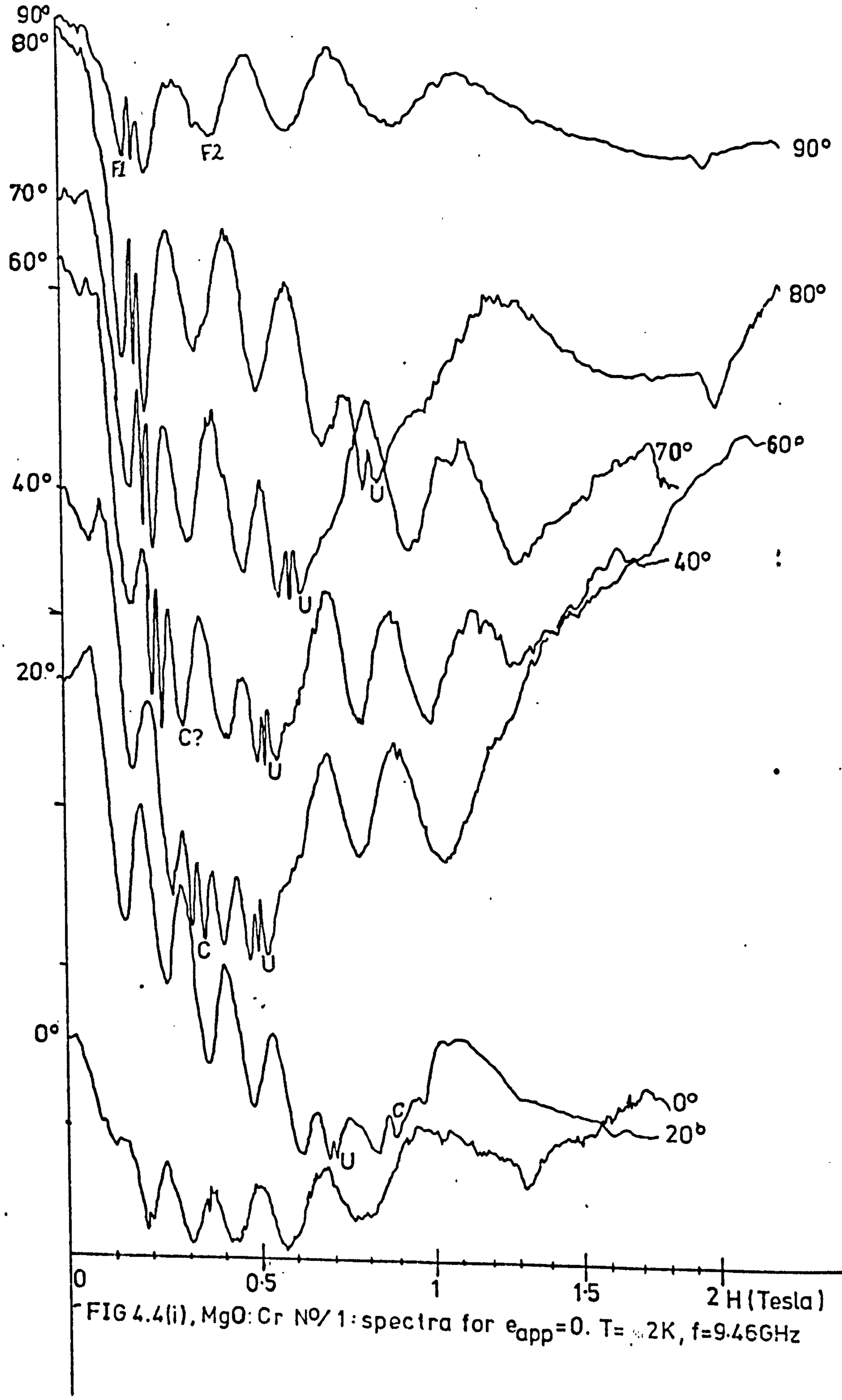

FIG 4.4(i), MgO: Cr N°/ 1 : spectra for e_{app}=0. T= 2K, f=9.46GHz

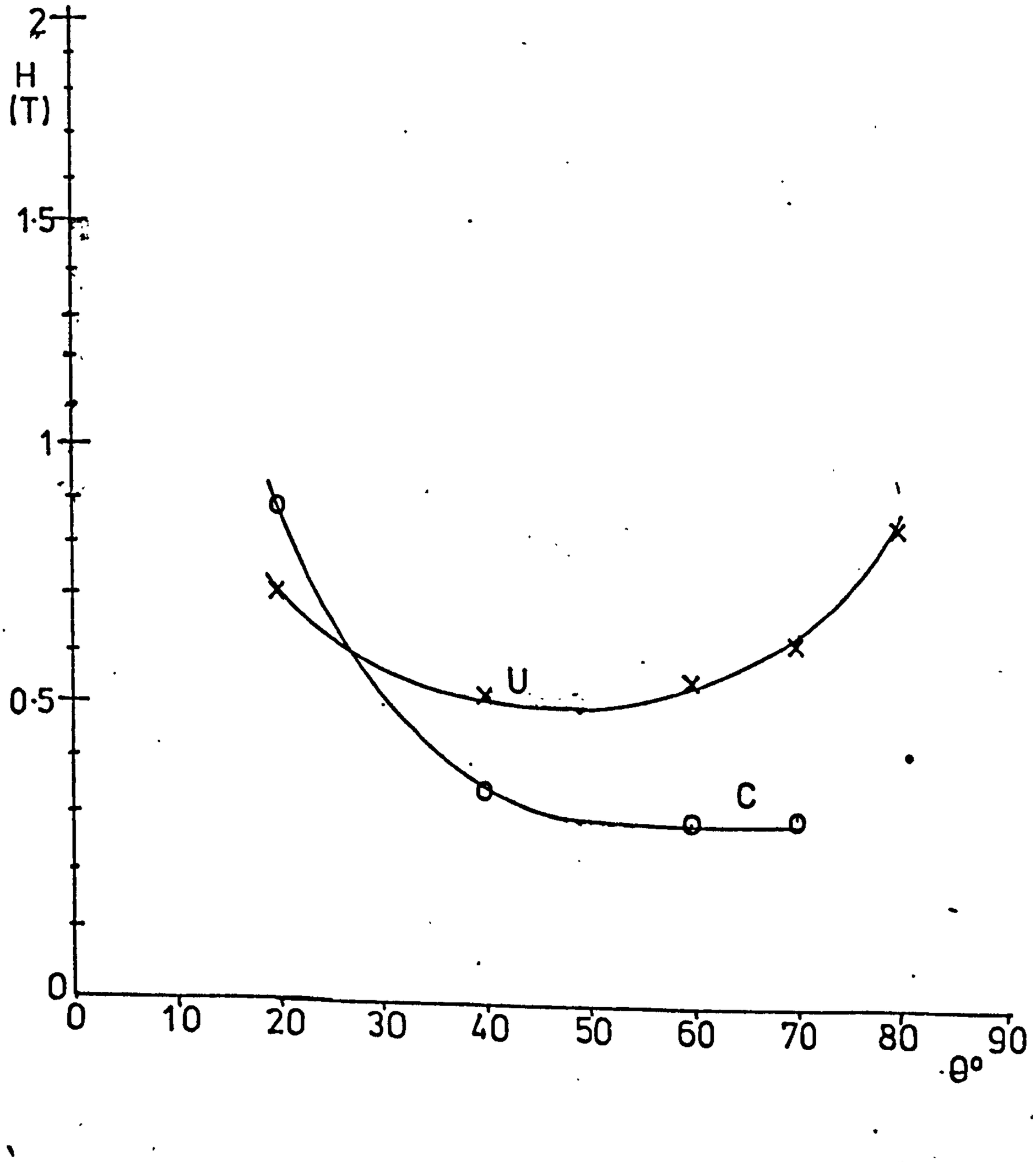

FIG. 4.4.(ii). Isofrequency curves of the lines labelled U and C on figure 4.4.(i).

ively. Figure 4.4.3 shows the variation in the spectrum, for field angle 60^{o}, for zero applied strain, 8.34×10^{-5} and 1.86×10^{-4}. The intensity of line U is seen to diminish, whilst line C exhibits a change of resonant field.

4.4(iv) Discussion.

The complexity of the observed spectrum, and the need to pump the helium to below 2.2K made experiments on as-received samples lengthy to perform and the results difficult to analyse. It was decided to anneal one of the samples such a way as to obtain a simpler spectrum.

4.5 Heat Treatments

(i) Introduction

Three samples of Cr : MgO in as-received state which gave identical spectra at 2.1K were chosen to undergo annealing. One sample Cr : MgO # 3, remained in as-received state; Cr : MgO # 2 was heated for 24 hours at 1300^{o}c in an atmosphere of 2% hydrogen, 98% nitrogen and the third sample, Cr : MgO # 1, was annealed for 24 hours at 1300^{o}c in a normal 'air' atmosphere. For each of the annealed samples, spectra were obtained and these were compared with that obtained from the as-received sample. Sample Cr : MgO # 1 was then hydrogen-annealed at 1300^{o}c for 2.5 hours.

4.5(ii) Simple Theory of Heat Treatment

An explanation of the action of annealing has been suggested by Anderson et al (1975). A hydrogen atmosphere is known to reduce the ion, whilst an oxygen atmosphere oxides it. Heating in an atmosphere of 2% hydrogen 98% argon (for safety reasons) is employed to reduce the ion, increasing the chromous concentration. Heating in air is employed for oxidation to increase the chromic concentration.

Combinations of annealing were employed to obtain the desired chromous concentration.

4.5(iii) Effect of Annealing on Cr : MgO Samples

It was found experimentally that for sample Cr : MgO #2 no sample echos were visible at 4.2K. These echos became visible when the temperature was reduced to below 2K. This result is consistent with the findings of King and Oates, (1974 private communitcation), who observed that hydrogen annealing increase the size of the relaxation peak centred on 6K, but that further annealing did not increase this peak further. This implies a maximum concentration of Cr^{2+} can be reached. The result is also consistent with the theory given above.

Sample Cr : MgO #1 exhibited large sample echos at 4.2K, but no chromous lines appeared in the spectrum. This is explained by a conversion of nearly all of the chromous ions to chromic, which does not exhibit APR. It is consistent with the findings of Oates, who observed that oxygen annealing removed the 6K peak. After hydrogen annealing at 1300°c for 2.5 hours, sample Cr : MgO #1 exhibited good sample echos at 4.2K and gave a Cr^{2+} spectrum very similar to that obtained by Marshall and Rampton (1968), i.e. lines U and C were clearly visible, as were F_1 and F_2, whilst most of the remaining features of the as-received sample spectrum were removed. This sample was used in all following experiments.

4.5(iv) Some Unusual Effects Concerning Annealing

Both Oates (1974 private communication) and this author observed a colour change in the samples upon oxygen annealing which has not been explained. Samples were originally of a pale green colour, but upon annealing, the colour darkened considerably, and a purple-ish

colour appeared in some samples. It was, at first, suspected that some impurity in the annealing boat or furnace had become introduced into the sample by diffusion, but further experiments disproved this suggestion. No further explanations were forthcoming, and the spectra resulting from these samples were very similar to those exhibited by previous samples treated in this way (Marshall, 1967) for which no such effect was noted.

A second effect was observed by this author which has also not been explained. After about one year of experimenting on sample Cr : MgO 1 it was observed that the chromous spectrum was decreased in intensity, and eventually disappeared completely, whilst sample echos were still clearly visible. Discussion with other workers (Dr P J King, Dr A A Ghazi, Dr V W Rampton) showed that annealing treatments were considered to be permanent. Ghazi, in particular, was able to exhibit samples which had undergone hydrogen annealing 18 months previously, and yet still clearly exhibited the same spectrum as immediately after the annealing. Experiments performed upon Cr : MgO 2 also showed an apparent degree of oxygen annealing. It is suggested that continuous re-polishing of the samples may have introduced this effect, since Tippell (1954) suggests that surface temperatures of glass-like samples upon optical polishing may exceed the melting point of the samples. He supports this argument with evidence that crack-filling by melting of the surface layer, and resulting flow, may occur rather than by abrasion of the surface, utilising accurate measurements to show reductions in sample length, per revolution of the polisher, of fractions of a molecular thickness.

Tippell also supports his argument with experiments which show that the relative hardnesses of the polish and sample are less important than their relative melting points in determining polishing efficiency. It was not possible to show that bulk heating of the sample, which may constitute an annealing process, was taking place on polishing, but given the high surface temperature and the thermal conductivity of MgO such a situation may occur.

4.6 Experiments on Annealed Samples

4.6(i) Introduction

Sample Cr : MgO #1 was used for these experiments. Initially, the experiments which had been performed on the as-received samples were repeated, using this sample. Secondly, further experiments were performed using the continuously-variable stressing system described in Chapter 3, section 7(i).

4.6(ii) Variation of Field Angle,

Spectra were recorded for values of θ ranging from 0° to 90°. These are shown in Figure 4.6(i). The lines U and C defined by Marshall and Rampton (1968) are clearly visible, and the variation of the position of their high-field edges with changing Θ can be seen. The isofrequency plots of H_{res} vs Θ for these lines U and C are shown in Figure 4.6(ii). This figure should be compared with the H_{res} vs Θ plots for U anc C of the as-received sample Figure 4.4.2, showing that the lines U and C are the same in both cases.

4.6(iii) Variation of Stress Using Hanging Masses

The effect on the spectrum of applied stress along the $[00\bar{1}]$ direction, (-z) using the hanging weights as in section 4.4(iii), was

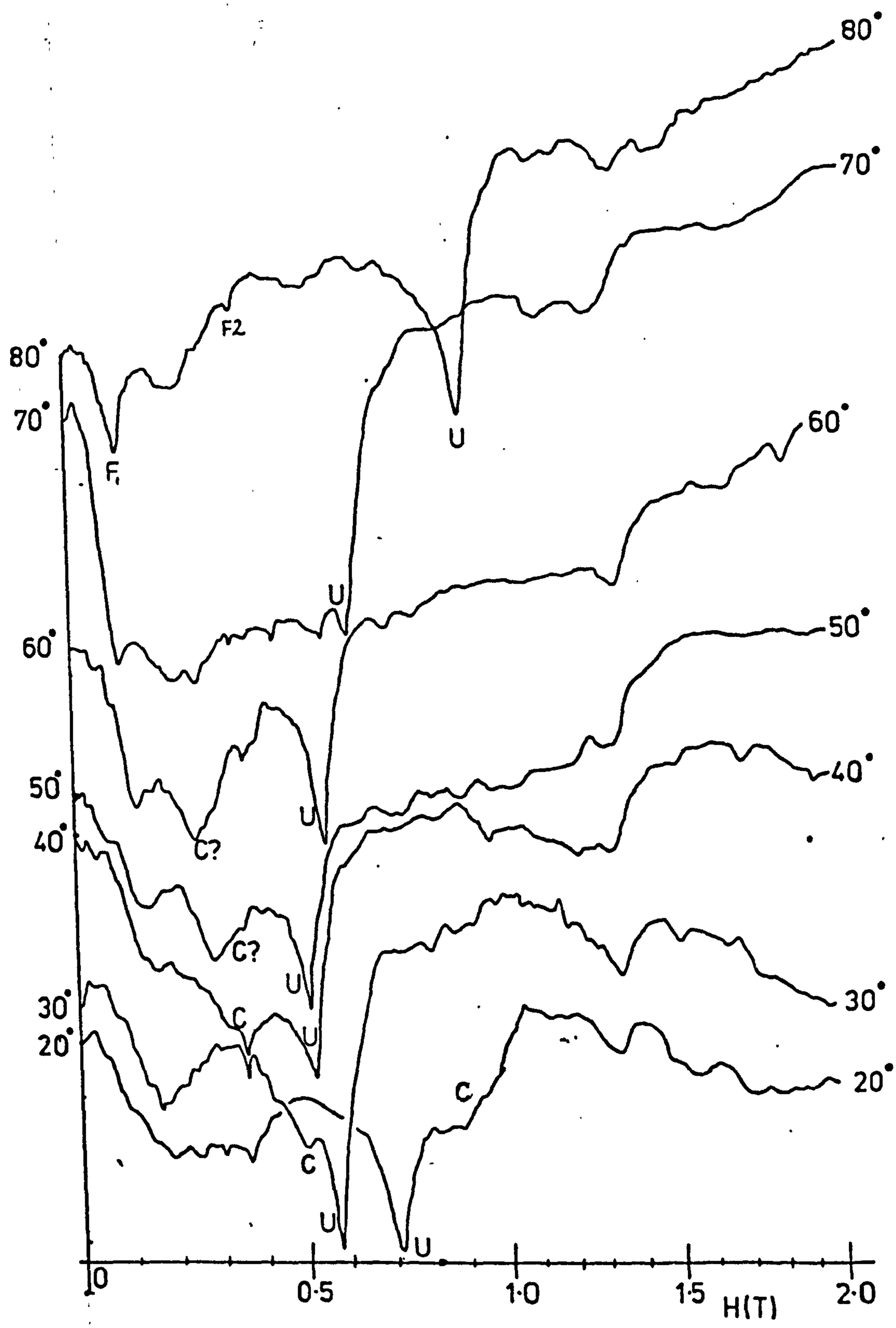

FIG.4.6.(i). Spectra of MgO:Cr N°1 afterannealing; $e_{app}=0$.
T=4.2K, f=9.5GHz.

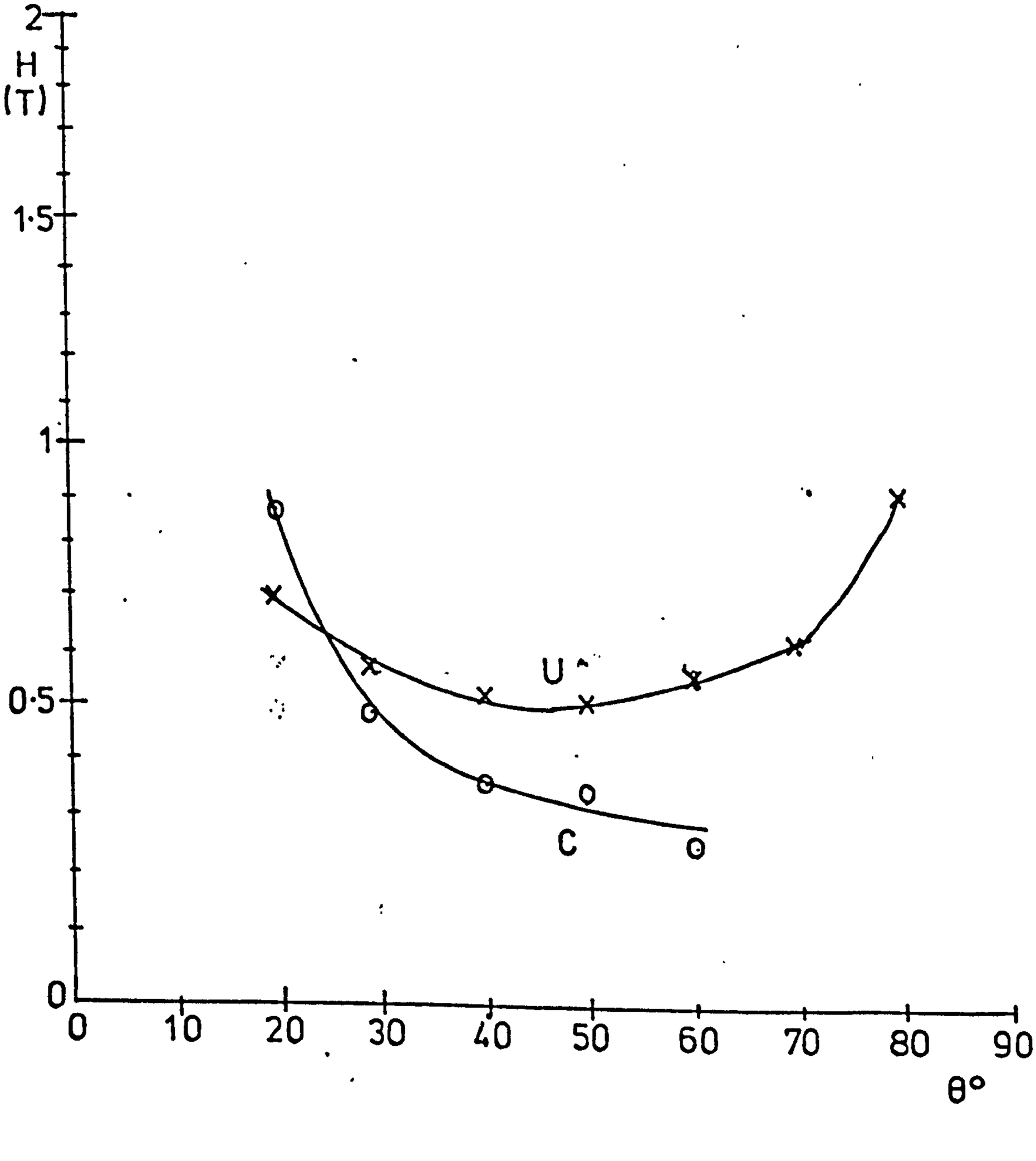

FIG. 4.6.(ii). Isofrequency curves of the lines labelled U and C on figure 4.6.(i).

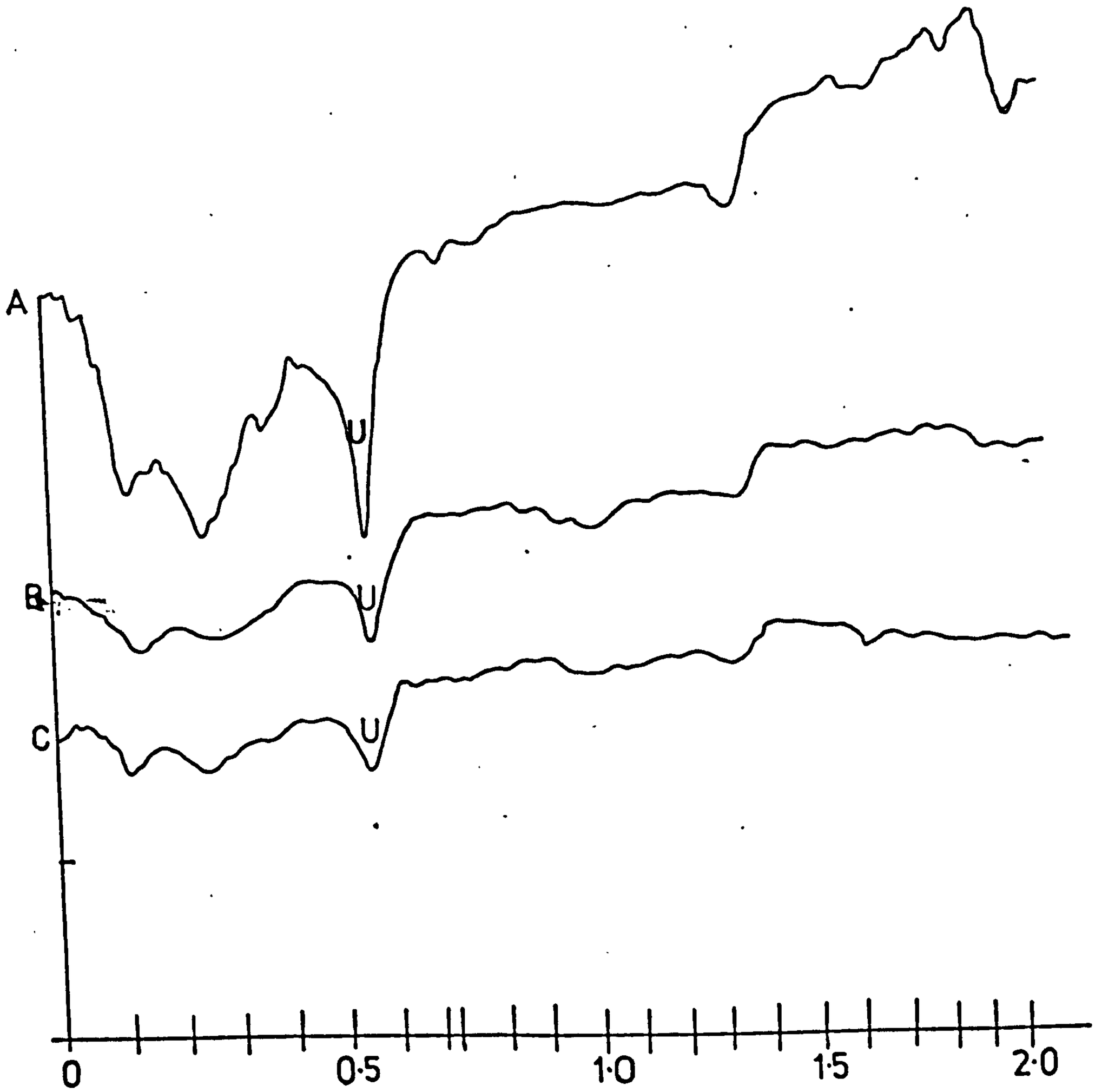

FIG.4.6 (iii) Effect of applied stress on the spectrum of MgO
:Cr N% 1 :- A: $e_{app}=0$
B $=0.93\times10^{-4}$
C $=1.86\times10^{-4}$
$\theta=60^{\circ}$, stresses applied by 'hanging mass system'.
T=4.2K f=9.5GHz.

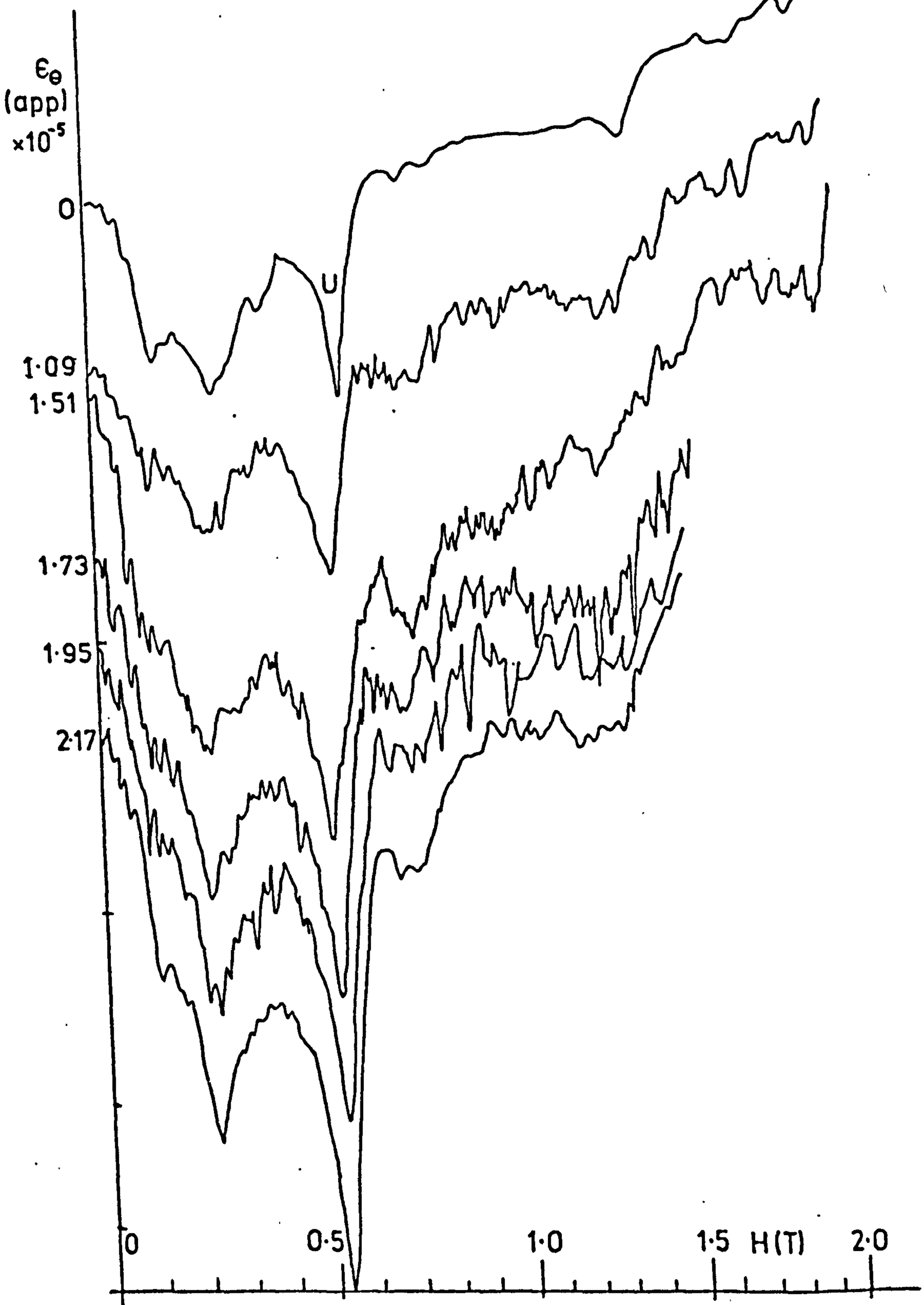

FIG 4.6 (iv). Effect of small changes in e_{app} (sliding counterweight) on the spectrum of MgO:Cr N°/1 $\theta = 60°$.
(T = 42K f = 9.46GHz)

observed. Figure 4.6(iii) shows the variation in the intensity of the spectrum when the stresses are applied (Rampton and Shellard, 1976) for $\Theta = 60^{\circ}$.

4.6(iv) Variation of Stress Using Continuous Sliding Mass

4.6(iv) (a) Reasons for Sliding Mass System

The sliding mass system was employed for two main reasons: firstly, it enables strains less than those used in the previous experiments to be introduced into the lattice,and secondly, it enabled plots to be made of the change in g-value of line C and the change in intensity of line U with applied stress. In addition to this, the use of larger sliding masses would enable similar plots to be made at higher values.of applied stress.

4.6(iv) (b) Results of Experiments

Figure 4.6(iv) shows the effect on the spectrum of the continuous change in applied stress. Since the total strain introduced into the lattice by this system is of order 2×10^{-5}, the variations in the spectrum should be less than those produced by the smaller hanging mass system. Figure 4.7(i) shows the change in g-value of line C with applied stress resulting from this experiment.

4.7 Discussions and Conclusions

4.7(i) General Features of the Spectrum

The theory of Ham, section 4.3, predicts an APR spectrum at a few degrees Kelvin, consisting mainly of two lines. These lines result from transitions within the Zeeman split doublet of a Γ_4 triplet level a few wavenumbers above a singlet ground state. Only a few of the chromium ions presentin the lattice, those at sites where the strain vectors are such that the resultant distortion is

near tetragonal and aligned with one of the crystal axes, may contribute to the resonance absorption. The symmetry of the experimental system is such that only those ions in sets A and C of Ham's analysis (Figure 4.3(ii) (a)) may contribute. The two line spectrum obtained in the experiments would agree closely with this. Ham further explains that the variation in strain at the chromium sites leads the asymmetry in the line shape, a sharp high-field-edge being expected. This edge is expected to be much sharper for a line with high-field-edge position determined by the parameter 'b' than for a line of position determined mainly by 'g'. since g varies greatly with random strain variation, whereas b is nearly independent of the details of the strain field. Consideration of the spectrum shows a much sharper high field edge on line U than on line C. The variation in position of H_{res} with field orientation of the lines is predicted by the theory as

$$h\nu = (4g^2\mu_B^2H_y^2 + 4b^2H_x^2H_z^2)^{1/2} \quad \text{---1} \quad \text{set C}$$

$$h\nu = (4g^2\mu_B^2H_z^2 + 4b^2H_x^2H_y^2)^{1/2} \quad \text{----2} \quad \text{set A}$$

In the experimental system angle is defined such that

$$Hx = H\cos\theta$$
$$Hy = H\sin\theta$$
$$Hz = 0$$

Substituting into 1

$$h\nu = (4g^2\mu_B^2H^2\sin^2\theta)^{1/2} = 2g\mu_BH\sin\theta \quad \text{---1(b)}$$

Substituting into 2

$$h\nu = (4b^2H^4\cos\theta\sin\theta)^{1/2} = \sqrt{2}\,bH^2(\sin 2\theta)^{1/2} \quad \text{--2(b)}$$

These expressions may be compared with the forms of the isofrequency H_{res} vs θ plots for lines C and U from Figures 4.4(ii) and 4.6(ii). The expressions for the C and U lines are of the form

$$H = h\nu / g_{\parallel} \mu_B \sin\theta \qquad \text{line C}$$

$$H = H_{res(min)} / (\sin 2\theta)^{1/2} \qquad \text{line U}$$

which compare with lines 1(b) and 2(b) respectively if

$$g = \tfrac{1}{2} g_{11} \qquad (1(b), \text{ line C})$$

$$|b| = h\nu / (H_{res(min)})^2 \quad (2(b) \text{ line U})$$

Marshall and Rampton (1968) noted that the position of line C varied from one sample to another, consistent with the strong strain dependence of g. This variation of position was not great in the present samples, however, since all present samples were prepared from the same melt and the impurity concentration was much higher than that of Marshall and Rampton's samples, it may be concluded that the strain fields in the samples are less varied.

4.7(ii) The Effect of Applied Stress on the Position of Line C

The position of line C is primarily determined by the value of g, according to the expression

$$h\nu = 2g \mu_B H \sin\theta \qquad \text{(Ham 1971)}$$

The value of g is, in turn, strongly dependent upon the details of the local strain distribution at the impurity ion site. It is to be expected, then, that an applied external strain of magnitude comparable with the value of the mean internal strain in the system, will change the value of g. This will be exhibited in the spectrum by a change in the position of line C. It can be shown (see section 4.7(iii) below) that the value of strain produced by the external stress system is significantly less than the value of the mean lattice strain, so the change produced in the position of line C will be expected to be small.

An expression for the variation in g to be expected for known changes in the local strain at the impurity sites, has been developed.

The triplet which contributes to the resonance splits into a doublet (which is split by the magnetic field) and a singlet. The triplet can be expressed as states $|E'x\rangle_0$, $|E'y\rangle_0$, $|E'z\rangle_0$, etc., which are combinations of the vibronic states $|E_\theta\rangle$, $|E_\epsilon\rangle$, $|A_1\rangle$, and spin states Γ_5 . (The following analysis refers to $\beta < 0$).

$$|E'x\rangle_0 = 1/2\,[\,-\sqrt{3}|E\theta\rangle - |E\epsilon\rangle\,]|\Gamma_5\rangle$$

$$|E^2x\rangle_0 = 1/2\,[\,-|E\theta\rangle + \sqrt{3}|E\epsilon\rangle\,]|\Gamma_5\rangle$$

$$|E^3x\rangle_0 = |A_1\rangle|\Gamma_5\rangle$$

{From Fletcher, 1967}

A Hamiltonian is set up which includes perturbations due to anharmonic Jahn-Teller coupling, second order spin-orbit coupling and strain coupling. This differs from that of Fletcher and Stevens (1969) in the inclusion of strain coupling. The perturbation may be expressed as:

$$\mathcal{H} = \begin{vmatrix} 2r & 0 & 0 \\ 0 & -r & 0 \\ 0 & 0 & -r \end{vmatrix} + \frac{1}{2} \begin{vmatrix} 0 & -2r & 0 \\ -2r & -2q & 0 \\ 0 & 0 & 2q \end{vmatrix} [-K(S_z^2 - 2) + V_2 e_\theta]$$

$$+\frac{1}{2} \begin{vmatrix} 0 & 0 & -2r \\ 0 & 0 & 2q \\ -2r & 2q & 0 \end{vmatrix} [-K(S_+^2 + S_-^2)] / 2\sqrt{3}$$

This Hamiltonian acts on states $|E\theta\rangle$, $|E\epsilon\rangle$ and $|A_1\rangle$. The assumption is made that the g-shift of the distorted site is the same as that in a pure cubic site, as the analysis is for a cubic site. The assumption is also made that the g-shift is predominantly linear in strain, and that higher order terms may be neglected. This latter assumption is experimentally justified by the fact that the g-shift is linear with applied strain in the range of the sliding

stress system. This linearity is shown in Figure 4.7(i). Before a solution can be obtained, the states have to be mixed to diagonalise the matrix which results from the Hamiltonian when acting on $\langle E^1x|$ etc. The method employed to do this was described by Fletcher (1967). Further state mixing occurs due to strain. Strain terms of second order develop during this analysis. These are neglected under the linearity assumption.

The original matrix is

$$\begin{array}{c|ccc} & & & \\ \langle E^1x| & -\Gamma-2qK-(V_2e_\theta/4) & -\sqrt{3}V_2e_\theta q/2 & \sqrt{3}V_2e_\theta r/2 \\ \langle E^2x| & -\sqrt{3}V_2e_\theta q/2 & -\Gamma+2qK-(V_2e_\theta)/4 & 2rK-V_2e_\theta r/2 \\ \langle E^3x| & 3V_2e_\theta r/2 & 2rK-V_2e_\theta r/2 & 2\Gamma \end{array}$$

(Spin matrix elements $\langle \Gamma_{5yz}|(S_z^2-2)|\Gamma_{5yz}\rangle = -1$

$\langle \Gamma_{5yz}|(S_+^2+S_-^2)/2\sqrt{3}\,|\Gamma_{5yz}\rangle = \sqrt{3}$)

The transformed states which diagonalise this matrix with respect to 3Γ and K are

$$|E^1x\rangle = |E^1x\rangle_0$$
$$|E^2x\rangle = \cos\beta_1|E^2x\rangle_0 + \sin\beta_1|E^3x\rangle_0$$
$$|E^3x\rangle = \cos\beta_1|E^3x\rangle_0 - \sin\beta_1|E^2x\rangle_0$$

where $\cos 2\beta_1 = \frac{1}{2}(3\Gamma-2qK)\,/\,(\frac{1}{4}(3\Gamma-2qK)^2+(2rK)^2)^{1/2}$

$$\tan 2\beta_1 = -4rK/(3\Gamma-2qK)$$

The final states which result after strain mixing are

$$|\tilde{E}^1x\rangle = |E^1x\rangle_0 + \left[\frac{\sqrt{3}/2\,V_2e_\theta(q\cos\beta_1 - r\sin\beta_1)}{3/2\,\Gamma+3qK-[\frac{1}{4}(3\Gamma-2qK)^2+(2rK)^2]^{1/2}}\right]|E^2x\rangle$$
$$+\left[\frac{\frac{1}{2}\sqrt{3}V_2e_\theta(-q\sin\beta_1 - r\cos\beta_1)}{3/2\,\Gamma+3qK+[\frac{1}{4}(3\Gamma-2qK)^2+(2rK)^2]^{1/2}}\right]|E^3x\rangle$$

(lower triplet)

$$|\tilde{E}^2x\rangle = |E^2x\rangle - \left[\frac{\sqrt{3}/2 V_2 e_\theta (q\cos\beta_1 - r\sin\beta_1)}{3/2\Gamma + 3qK - [1/4(3\Gamma - 2qK)^2 + (2rK)^2]^{1/2}}\right] |E'x\rangle_o$$

$$\text{(upper triplet)} \quad + \left[\frac{1/4\ (\sqrt{3}V_2 e_\theta (q\sin 2\beta_1 - 2r\cos 2\beta_1))}{2[1/4\ (3\Gamma - 2qK)^2 + (2rK)^2\ ]^{1/2}}\right] |E^3x\rangle$$

Other states $|\tilde{E}'y\rangle$, $|\tilde{E}^2y\rangle$ can be obtained by transforming the above under C_4 rotational symmetry.

A similar analysis may be performed for $\beta > 0$. The final step is to include the Zeeman interaction, which gives the energy splitting between the pairs of doublet levels. The very small orbital contribution to the Zeeman splitting is neglected. (Fletcher and Stevens, 1969).

$$\text{Splitting} = 2|\langle \tilde{E}'x | \mathcal{H}_z | \tilde{E}'y\rangle| \qquad \text{(lower triplet)}$$

$$\text{where} \quad \mathcal{H}_z = g\ \underline{H}.\underline{S} \qquad (g=2)$$

$$\text{or } 2|\langle \tilde{E}^2x | \mathcal{H}_z | \tilde{E}^2y\rangle| \qquad \text{(upper triplet)}$$

The splitting may also be written as

$$h\nu = 2g_m\beta H_z$$

where g_m is the effective g-value of the split doublet in the crystal environment.

A substitution can thus be made to obtain a value for g_m in terms of the strain and the other parameters of the system. The substitution was made for the results of analysis for the upper and lower triplets of cases $\beta < 0$ and $\beta > 0$. A computer programme wad devised which calculated a value of g_m in terms of strain θ and the parameter V_2/K. This programme was run for both triplets with both signs of β, and for various choices of the parameters $3\Gamma/K$, and q and r. The programme, some results for values of the parameters suggested by previous experimental results, and the exact expressions used to obtain g are included as Figure 4.7(ii). It should be noted that the programme was written and run in the

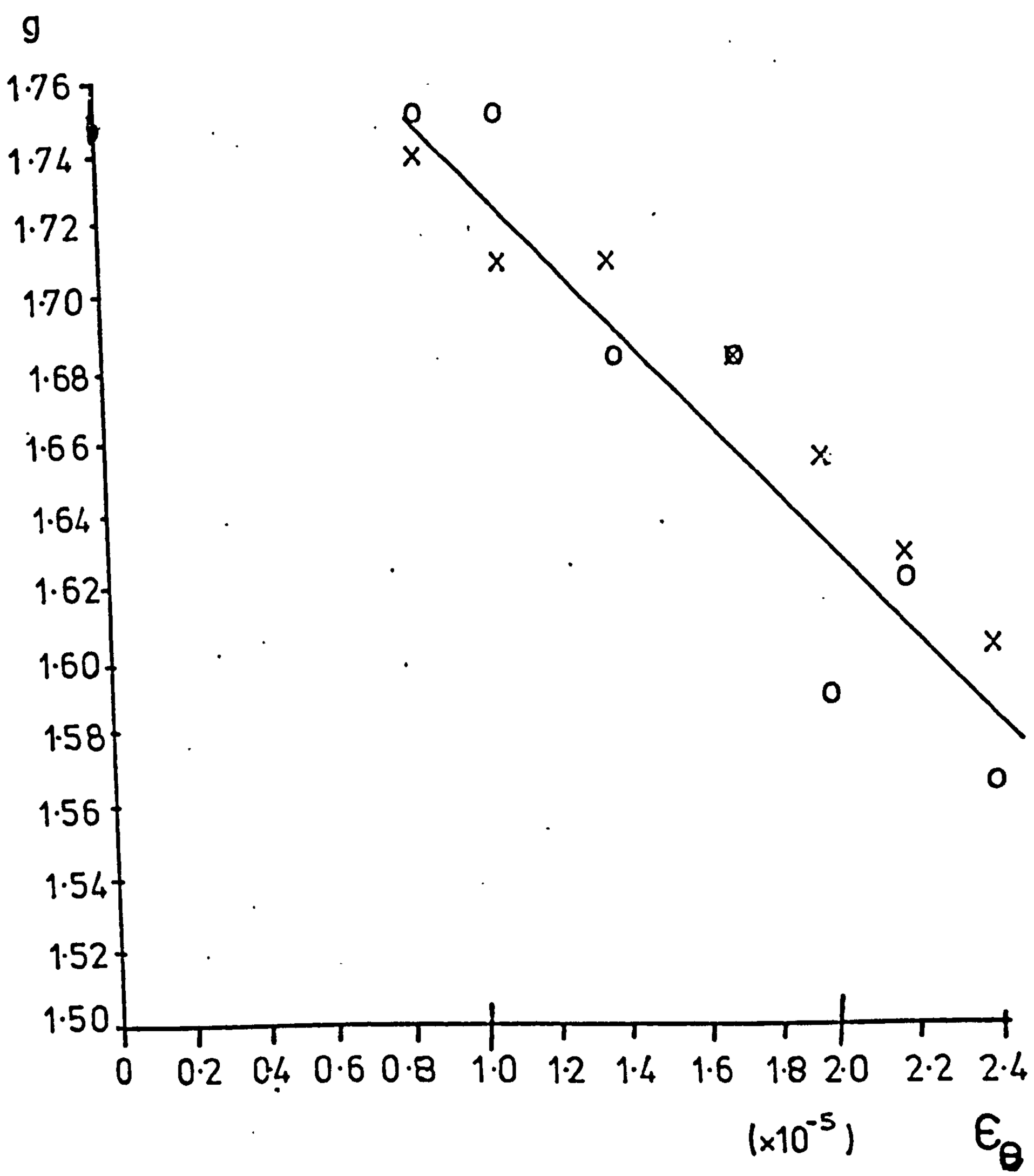

FIG 4.7.(i) VARIATION of g-VALUE of C-LINE of MgO:Cr N°1 WITH APPLIED STRAIN.

o: experiment with $\theta = 50^{\circ}$
x: experiment with $\theta = 40^{\circ}$

$$g = 1 + \frac{6V_2 e_\theta}{K}\left[\frac{1}{P}\left[\frac{q(6\Gamma/K - 2q + P) + 4r^2}{6\Gamma/K + 6q - P} - \frac{q(6\Gamma/K - 2q - P) + 4r^2}{6\Gamma/K + 6K + P}\right]\right]$$

$\beta < 0$

$$g = (1 - 3\sin^2\beta_2) - \frac{6V_2 e_\theta}{K}\left[\frac{1}{Q}\left[\frac{(6\Gamma/K - 2q + Q)q}{Q - 6\Gamma/K - 6r} - 4r^2 - \frac{4\Gamma r^2}{KQ^2}\right]\right]$$

$\beta > 0$

where $P = [(6\Gamma/K - 2q)^2 + 16r^2]^{1/2}$

$Q = [(6\Gamma/K + 2q)^2 + 16r^2]^{1/2}$

$\beta_2 = \tan^{-1}[2Kr/(3\Gamma + qK)]$

FIG 4.7.(ii)a. Expressions used to calculate the theoretical change in g with e_θ applied.

```
0100 PPINT "F1"
0110 INPUT F1
0120 PPINT "F2"
0130 INPUT F2
0140 PRINT "SLOPE OF G VS. STPAIN"
0150 PPINT "","E>0",,"E<0"
0160 PRINT "DELTA/D","LOWEP","UPPEP","LOWER","UPPEP"
0170 FOP D=1 TO 9 STEP 1
0180   GOSUB 0300
0190 NEXT D
0200 FOP D=10 TO 100 STEP 10
0210   GOSUB 0300
0220 NEXT D
0230 STOP
0300 LET P=SQR((D-F1)*(D-F1)+4*F2*F2)
0310 LET Q=SQR((D+F1)*(D+F1)+4*F2*F2)
0320 LET A1=F1*(D-F1+P)+2*F2*F2
0330 LET A2=F1*(D-F1-P)+2*F2*F2
0340 LET B1=D+3*F1-P
0350 LET B2=D+3*F1+P
0360 LET G1=4*((A1/B1)-(A2/B2))/(2*P)
0370 LET B3=(D*F2*F2)/(2*P*P)
0380 LET G2=4*((A1/B1)-B3)/(2*P)
0390 LET E1=F1*(D+F1+Q)-2*F2*F2
0400 LET E2=D*F2*F2/(3*Q*Q)
0410 LET E3=Q+3*F1-D
0420 LET E4=(F1*(D+F1-Q)-2*F2*F2)/2
0430 LET E5=D-3*F1+Q
0440 LET G3=4*((E1/E3)-E2)/(2*Q)
0450 LET G4=4*((E1/E3)-(E4/E5))/(2*Q)
0460 PPINT D,G1,G2,G3,G4
0470 PETUPN
0500 END
```

FIG 4.7(ii)b Computer programme used to obtain theoretical slope of g vs e_θ, and results for various choices of parameters.
(5 pages following)

```
F1
 ? 1
F2
 ? 1
SLOPE OF G VS. STRAIN
```

DELTA/D	B>0 LOWER	UPPER	B<0 LOWER	UPPER
2	1.6	1.51554	.526254	.83205
3	1.42857	1.38982	.624853	.77082
4	1.33333	1.32093	.693085	.779527
5	1.27273	1.27161	.741794	.799122
6	1.23077	1.23404	.777839	.818672
7	1.2	1.20479	.805395	.83596
8	1.17647	1.18158	.827055	.850791
9	1.1579	1.16286	.844485	.863449
10	1.14286	1.14748	.858788	.874285
20	1.07317	1.07502	.926869	.930896
30	1.04918	1.0501	.950773	.952585
40	1.03704	1.03758	.962918	.963943
50	1.0297	1.03006	.970262	.97092
60	1.02479	1.02505	.975179	.975637
70	1.02128	1.02147	.9787	.979037
80	1.01863	1.01878	.981348	.981606
90	1.01658	1.01669	.983411	.983615
100	1.01493	1.01502	.985061	.985226

```
STOP AT 0230
*RUN
F1
 ? 0.991
F2
 ? 1.174
SLOPE OF G VS. STRAIN
```

DELTA/D	B>0 LOWER	UPPER	B<0 LOWER	UPPER
2	1.90878	1.87084	.404466	.768838
3	1.63302	1.61324	.515234	.700201
4	1.48566	1.4815	.596519	.709216
5	1.39395	1.39773	.656705	.732652
6	1.33137	1.33831	.702323	.756961
7	1.28595	1.29377	.737779	.778951
8	1.25148	1.2592	.765984	.798106
9	1.22443	1.23166	.788882	.814632
10	1.20263	1.20925	.807804	.8289
20	1.10279	1.10535	.899337	.904869
30	1.06886	1.07013	.931999	.934492
40	1.05177	1.05252	.948685	.950096
50	1.04148	1.04197	.958804	.959711
60	1.0346	1.03495	.965591	.966222
70	1.02968	1.02994	.970461	.970925
80	1.02598	1.02618	.974123	.974479
90	1.0231	1.02326	.976977	.977259
100	1.0208	1.02093	.979267	.979495

```
STOP AT 0230
```

```
F1
 ? 0.977
F2
 ? 1.269
SLOPE OF G VS. STRAIN
```

DELTA/D	B>0 LOWER	UPPER	B<0 LOWER	UPPER
2	2.14843	2.13868	.334647	.72502
3	1.78418	1.77894	.450273	.655607
4	1.59535	1.59857	.537985	.665248
5	1.47981	1.48798	.604323	.69093
6	1.40183	1.41182	.655321	.718012
7	1.34565	1.35582	.695351	.742788
8	1.30326	1.31288	.727426	.764543
9	1.27012	1.27895	.753609	.783426
10	1.24352	1.2515	.775336	.799803
20	1.12268	1.12569	.8815	.887951
30	1.08199	1.08348	.919765	.922676
40	1.06157	1.06245	.939387	.941036
50	1.0493	1.04988	.951307	.952366
60	1.0411	1.04151	.959312	.960049
70	1.03525	1.03555	.965057	.9656
80	1.03084	1.03108	.969386	.969802
90	1.02743	1.02761	.972753	.973082
100	1.02469	1.02484	.975458	.975725

```
STOP AT 0230
*RUN
F1
 ? 0.970
F2
 ? 1.315
SLOPE OF G VS. STRAIN
```

DELTA/D	B>0 LOWER	UPPER	B<0 LOWER	UPPER
2	2.28644	2.29022	.301147	.702994
3	1.86858	1.87089	.418483	.633435
4	1.65562	1.66289	.508945	.643284
5	1.52653	1.53714	.578088	.669953
6	1.43991	1.45158	.63162	.698323
7	1.37776	1.3892	.673852	.724429
8	1.331	1.34165	.707813	.747445
9	1.29454	1.30422	.735612	.767484
10	1.26532	1.27402	.75873	.784903
20	1.13318	1.13641	.87228	.879201
30	1.0889	1.0905	.91342	.916545
40	1.06672	1.06767	.934555	.936325
50	1.0534	1.05402	.947407	.948544
60	1.04451	1.04495	.956042	.956834
70	1.03816	1.03849	.962239	.962822
80	1.03339	1.03365	.966911	.967358
90	1.02969	1.02989	.970551	.970904
100	1.02672	1.02689	.973472	.973759

```
STOP AT 0230
```

STOP AT 0230
*RUN
F1
 ? 0.969
F2
 ? 1.361
SLOPE OF G VS. STRAIN

DELTA/D	B>0 LOWER	B>0 UPPER	B<0 LOWER	B<0 UPPER
2	2.42428	2.43957	.27164	.685758
3	1.9516	1.96051	.389827	.6146
4	1.71448	1.72535	.482373	.623907
5	1.57196	1.58477	.553843	.651063
6	1.47684	1.49006	.609568	.680364
7	1.40885	1.42148	.653749	.707535
8	1.35783	1.36944	.689407	.731614
9	1.31813	1.32862	.718677	.752654
10	1.28636	1.29576	.743071	.770996
20	1.14328	1.14675	.863512	.870917
30	1.09554	1.09726	.907371	.910716
40	1.07166	1.07268	.929943	.931838
50	1.05733	1.058	.943682	.944901
60	1.04778	1.04825	.952921	.953769
70	1.04096	1.04131	.959555	.96018
80	1.03584	1.03611	.964553	.965031
90	1.03166	1.03208	.968449	.968826
100	1.02868	1.02885	.971575	.971882

STOP AT 0230
*RUN
F1
 ? 0.970
F2
 ? 1.366
SLOPE OF G VS. STRAIN

DELTA/D	B>0 LOWER	B>0 UPPER	B<0 LOWER	B<0 UPPER
2	2.43688	2.45307	.269137	.684827
3	1.95922	1.96864	.387316	.613218
4	1.71991	1.73104	.479998	.622338
5	1.57616	1.58913	.551649	.649463
6	1.48026	1.4936	.607556	.678804
7	1.41173	1.42446	.651905	.706045
8	1.36032	1.37202	.687713	.730204
9	1.32032	1.33088	.717114	.751323
10	1.28831	1.29778	.741621	.769739
20	1.14422	1.14771	.86269	.870148
30	1.09616	1.09788	.906802	.910172
40	1.07212	1.07314	.929509	.931418
50	1.0577	1.05837	.94333	.944557
60	1.04808	1.04856	.952621	.953476
70	1.04122	1.04157	.959296	.959926
80	1.03607	1.03634	.964328	.96481
90	1.03206	1.03228	.968247	.968629
100	1.02885	1.02903	.971396	.971705

STOP AT 0230

```
STOP AT 0230
*RUN
F1
 ? 0.967
F2
 ? 1.339
SLOPE OF G VS. STRAIN
                B>0             UPPER           B<0
DELTA/D         LOWER           2.37392         LOWER           UPPER
 2               2.36335        1.92108          .284199         .69192
 3               1.91487        1.69782          .402209         .62215
 4               1.68841        1.56374          .493959         .632002
 5               1.55182        1.47303          .564474         .659109
 6               1.46046        1.40718          .619274         .688097
 7               1.39505        1.35711          .66262          .71486
 8               1.34592        1.31778          .697544         .738512
 9               1.30765        1.2861           .726174         .759138
 10              1.27701        1.14214          .75001          .777093
 20              1.13878        1.09424          .867414         .874586
 30              1.09258        1.07045          .910066         .913305
 40              1.06946        1.05623          .932            .933835
 50              1.05558        1.04678          .945341         .946521
 60              1.04632        1.04005          .954311         .955132
 70              1.03971        1.03501          .960756         .96136
 80              1.03475        1.0311           .965601         .966064
 90              1.03089        1.02797          .969385         .969752
 100             1.0278                          .972421         .972718

STOP AT 0230
*RUN
F1
 ? 0.967
F2
 ? 1.352
SLOPE OF G VS. STRAIN
                B>0             UPPER           B<0
DELTA/D         LOWER           2.41612         LOWER           UPPER
 2               2.40239        1.94634          .276047         .687272
 3               1.93831        1.71541          .394257         .616982
 4               1.705          1.57714          .486564         .626646
 5               1.56462        1.48386          .557714         .653867
 6               1.47086        1.41625          .613117         .683102
 7               1.4038         1.36493          .657002         .710154
 8               1.35346        1.32464          .692398         .734096
 9               1.31428        1.29221          .721437         .754999
 10              1.28292        1.14504          .745628         .773208
 20              1.14162        1.09614          .864954         .872263
 30              1.09445        1.07185          .90837          .911671
 40              1.07085        1.05735          .930704         .932575
 50              1.05669        1.04771          .944295         .945497
 60              1.04724        1.04084          .953435         .954272
 70              1.04049        1.0357           .959999         .960615
 80              1.03544        1.03171          .964936         .965408
 90              1.0315         1.02852          .968796         .969169
 100             1.02835                         .971886         .972188

STOP AT 0230
```

```
STOP AT 0230
*RUN
F1
 ? 0.971
F2
 ? 1.371
SLOPE OF G VS. STRAIN
                B>0                                    B<0
DELTA/D         LOWER           UPPER          LOWER           UPPER
 2               2.44958         2.46667        .266643         .6839
 3               1.96689         1.97682        .38481          .61184
 4               1.72535         1.73676        .477626         .620772
 5               1.58037         1.59352        .549457         .647865
 6               1.48369         1.49715        .605545         .677246
 7               1.41463         1.42745        .650061         .704556
 8               1.36282         1.3746         .686018         .728793
 9               1.32252         1.33316        .715548         .74999
 10              1.29028         1.29981        .740171         .768483
 20              1.14517         1.14869        .861874         .869387
 30              1.09678         1.09852        .906237         .909631
 40              1.07259         1.07362        .929078         .931002
 50              1.05807         1.05875        .942985         .944221
 60              1.0484          1.04888        .952334         .953194
 70              1.04148         1.04184        .959049         .959682
 80              1.0363          1.03657        .964111         .964596
 90              1.03227         1.03249        .968053         .968437
 100             1.02905         1.02922        .971222         .971533

STOP AT 0230
*
```

Fletcher notation, but comparision to this analysis may be made by using the table of equivalence (Table 4.3(ii)).

It was noted that if a calculation of the splitting is calculated for each of the four cases, and then the assumption that $3\Gamma/K$ is large (tending to infinity) is made, the same result

$$g_m = 1 + \frac{3V_2 e_\theta}{4K}$$

is obtained for every case. Consideration of the computer results shows that g_m approaches a constant value very quickly indeed and is constant to within experimental error for $3\Gamma/K$ ratios of greater than 20.

A comparision of the results of the experiments to measure the relationship of g_m and e_θ with the results of the computer programme enables a choice of the various parameters to be made. We may write

$$g_m = 1 + \frac{3V_2 e_\theta X}{4K}$$

$$[X = 1 \pm 0{\cdot}1 \text{ for } 3\Gamma/K \geqslant 20]$$

The strain axis of Figure 4.7(i) was obtained from expressions given by Azaroff (1960) and Landau and Lifshitz (1959) relating strain along the crystal axes e_{xx}, e_{yy}, e_{zz} to applied stress. We also use the expression

$$e_\theta = e_{zz} - \tfrac{1}{2}(e_{xx} + e_{yy})$$

The values of crystal parameters for MgO were obtained from standard tables.

The points on the graph were analysed by a method of least squares computer programme. The graph is of the form

$$y = mx + c$$

where $y = g_m$, $x = \theta$ and m is given by $\frac{3V_2X}{4K}$

Values of X obtained from the main computer programme may be used in conjunction with experimentally obtained values for either

V_2 or K to predict the other. The experimental results give $m = -10.5 \pm 1.2 (\times 10^3)$. If the value of $-\sqrt{3}V_2/2$ given by Rivellin and Salce (1976) of $-1.7 \times 10^3 cm^{-1}$ is used, and X is obtained for the previously predicted values $3\Gamma/K \sim 8$, $q = \frac{1}{2}$. $r = \frac{1}{2}$, then:

$K = 3.7cm^{-1}$ $\beta < 0$

$K = 2.0cm^{-1}$ $\beta > 0$

are obtained. The results are in good agreement with other results for K (section 4.3(ix))

Conversely, it may be said that choosing the value of K as 4 for $\beta < 0$ (an experimentally obtained value (section 4.3 (ix))) predicts a strain coupling constant in good agreement with that of Rivellin and Salce. (It should be noted that the strain constant $17 \times 10^3 cm^{-1}$ obtained by these authors was the Fletcher and Stevens 'aC_1'. From Table 4.3(iii) it will be seen that V_2, obtained here, must be multiplied by $-\sqrt{3}/2$ for direct comparision).

It is believed that the present method of obtaining a value for V_2 is the most direct available, and therefore, that the good agreement between results obtained by this method and others is strong evidence for the choice of parameters given above.

Lange (197) concludes that the contributing levels are in the upper triplet. It should be noted that the results obtained from the computer programme shown in Figure 4.7(ii) are very similar for both the upper and lower triplets, and it is thus possible to fit the present experimental results equally well to the transitions in the upper triplet.

4.7(iii) The Effect of Stress on the Intensity of the APR Peaks

The effect of a variation in the local strain at an impurity site on the U-line is to change the intensity of the absorption peak, but not to change the position of the high-field edge. The

expression giving the position of the high-field edge for the U-line (Ham (1971)) is

$$h\nu = [4b_{min}^2 H_x^2 H_y^2]^{1/2}$$

Now b_{min} is nearly independent of the local values of e_θ and e_ε at the chromium site, and hence the above expression is independent of strain. (Figure 4.3(iii)).

The intensity of the absorption peak, however, depends on the value of the strain distribution around the value of strain corresponding to $b = b_{min}$. It is assumed that the random strain distribution in the lattice is smooth about the b_{min} position, and that it extends well away from b_{min}. The effect of an applied uniaxial stress results in the superimposition of uniform, static strains onto the random strain distribution. Three cases can occur:

(a) $e_{app} \ll \bar{e}_{random}$ (= mean value of random strain).

In this case the peak intensity should be independent of the value of applied stress, since the uniform strain resulting from the applied stress will only move the random distribution away from b_{min} by a very small amount, and, since the random distribution is smooth and extends well away from b_{min}, this will result in very small changes in the value of the strain distribution at b_{min}

(b) $e_{app} \sim \bar{e}_{random}$

As e_{app} approaches $\bar{e}$ random the strain distribution will be moved well away from b_{min}. This will result in a smaller number of ions having the necessary strain values to contribute to the resonant absorption, and the intensity of the absorption peak will diminish.

(c) $e_{app} \gg \bar{e}_{random}$

If sufficient applied stress could be used, it would be possible to shift the distribution to a point where no ions were able to contribute to the resonance, and hence the peak would diminish to zero.

According to Ham, if the stress is applied along the z-axis ([001]) of the crystal, line A (Figure 4.3(ii)) remains a diameter of the strain distribution, and the number of ions able to contribute to the resonant absorption from set A should be reduced less by the applied stress than the numbers from set C. Hence the C-line should reduce in intensity by a greater amount than the U-line. This effect will become more marked as $e_{app} \rightarrow \bar{e}$ random, since for small stresses line C will still be close to a diameter of the strain distribution. Marshall and Rampton (1968) observed an increase in the intensity of the U-line on pressure application. This was interpreted by Ham in terms of the population of the contributing doublet. If e_θ has a negative sign (i.e. compression) and V_2, the strain coupling constant, is also negative, then the term $x(= V_2 e_\theta / K)$ is positive. Further, as e_θ increases in a negative sense, x increases in a positive sense. Now x is related to the doublet excitation energy in such a way that as x is increased in a positive sense, the doublet excitation energy is lowered, and hence the population of the level would increase, giving a more intense resonance peak. Fletcher and Stevens interpret the increase in the U-line intensity in terms of a re-alignment of the tetragonal distortions upon pressure application.

The results of the present work (Figures 4.6(iii) and (iv)) show a decrease in the intensity of the U-line with increasing stress; opposite to the effect observed by Marshall and Rampton. The magnitude of this effect is, however, small (consistent with the idea that the magnitude of the strain resulting from the applied stress is small by comparison with the mean random internal strain). It may be inferred that e_{app} in the present experiments is very much less than e_{app} in the Marshall-Rampton experiment. (This conclusion is supported by the fact that Marshall and Rampton arrived at their applied stress

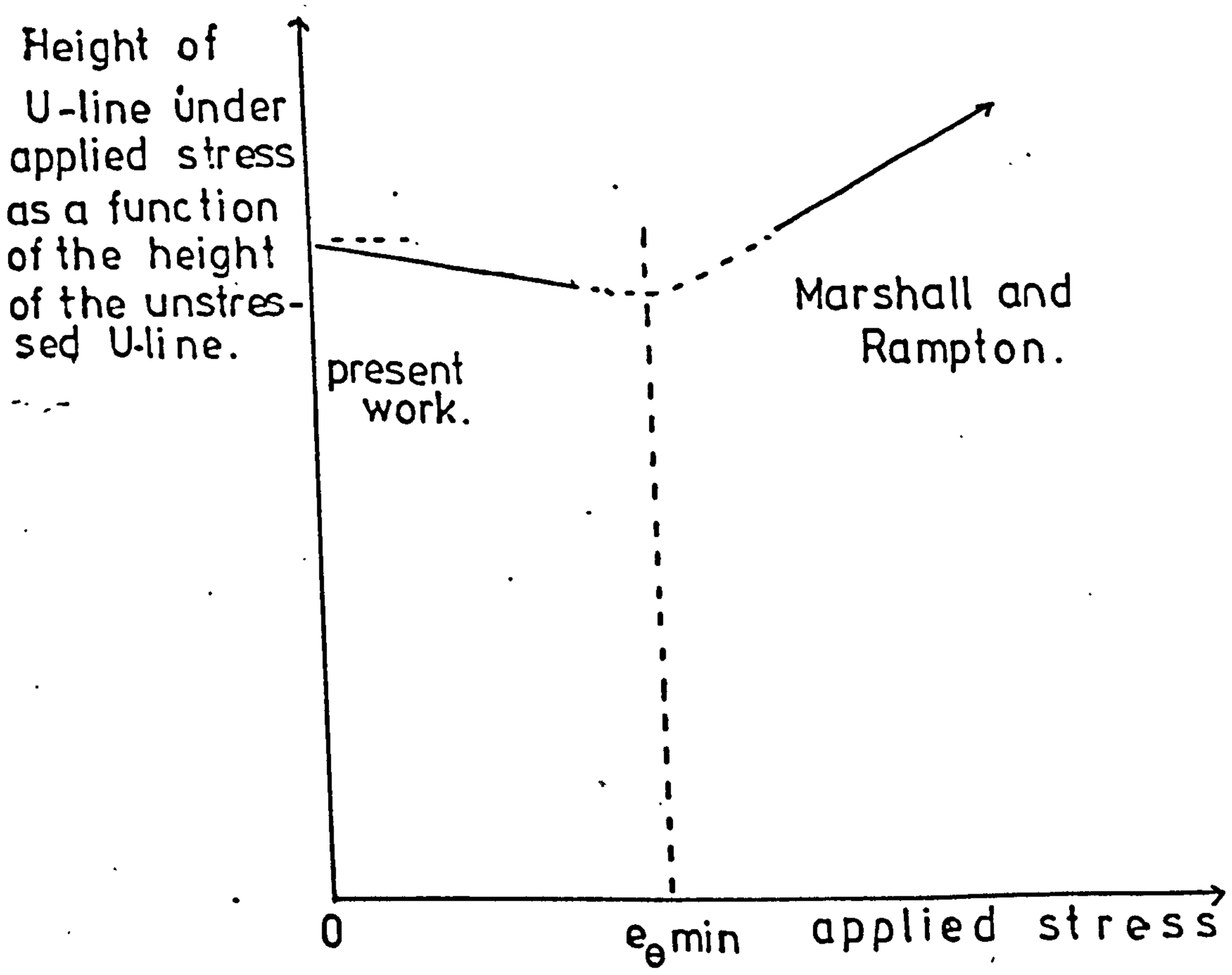

FIG 4.7 (iii) Schematic representation of the change in intensity of the U-line as a function of applied stress.

by progressive loosenings of the clamp which provided the stress until it no longer broke the sample on cooling. At no time in the present experiments did the sample suffer any damage due to the applied stress). Using these facts the results may be interpreted in terms of a random internal strain distribution as follows:-

An impurity ion sitting on a perfect cubic site undergoes no net strain in any direction. There are very few such ions, less than the number of ions which contribute to the resonant absorption under the condition of zero applied stress. As an external stress along a crystal axis is applied the random strain distribution is moved along one of the lines A, B, C in Figure 4.3(ii) (Ham 1971). Another way of viewing this is to say that the symmetry at each impurity site is changed by the applied compression. Hence a site of originally pure cubic symmetry will exhibit a gradually increasing tetragonal compression as the applied stress increases. Ions which could originally contribute to the resonant absorption will no longer be able to do so, whilst ions which could not originally contribute will begin to do so. Eventually a situation will be reached where the ions which originally exhibited perfect cubic symmetry will be the only ones contributing. There are less of those than of the mixed cubic/tetragonally strained ions, hence the intensity of the APR absorption peak will be less. If the applied stress is then further increased these ions will no longer contribute and those which were originally of mixed cubic tetragonal strain on the other side of the distribution will begin to contribute. In this case the intensity of the APR peak will begin to increase, as observed by Marshall and Rampton. (In terms of Ham's model this may be seen as moving the distribution through the zero strain position and then away on the other side).

A schematic representation of this interpretation is shown in Figure 4.7(iii). The position of the minimum, $e_{\theta min}$, corresponds to the applied strain at which the originally unstrained ions are contributing to the resonance. Conversely it can be deduced that the value of $e_{\theta app}$ at $e_{\theta min}$ is equal to the value of e_{θ} on the ions which contribute to the resonance absorption at zero applied strain.

From the present experiments, then, the following conclusions may be reached

(i) The maximum value of applied strain, $e_{\theta app}$, resulting from the sliding weight stress system, is less than the value of e_{θ} acting on the ions which contribute to the resonant absorption at zero applied stress, $e_{\theta min}$. It would appear that this is also true of the maximum value of $e_{\theta app}$ resulting from the hanging mass stress system (although with only three values of stress in this system this deduction may not be taken as proved). Hence:

$e_{\theta min} \geq e_{\theta app}$ sliding weight ($e_{\theta app}$ hanging mass)

i.e. $e_{\theta min} \geq 2.39 \times 10^{-5}$ (1.86×10^{-4})

(ii) If the assumption that the stresses used by Marshall and Rampton (1968) are greater than those used in the present experiments is correct then the stress applied by Marshall and Rampton is $> e_{\theta min}$. Unfortunately it is not possible to accurately estimate these stresses, as the system used by Marshall and Rampton does not allow this. A maximum value for these stresses may, however, be estimated from the relative thermal expansions of brass and MgO, and hence a maximum value for $e_{\theta min}$ may be obtained. This gives

$$e_{\theta min} < 10^{-3}$$

(iii) It is possible to draw some conclusions about the strain at the site of the contributing ion, corresponding to $e_{\theta min}$. The model of Figure 4.7(iii) implies that, at least for stresses $< e_{\theta min}$ the change in intensity of the U-line with applied stress is due to a change in the number of ions contributing to the resonance. Hence for $e_{\theta app} < e_{\theta min}$ a reduction in intensity of the U-line is observed for $e_{\theta n}$ positive or negative, where $e_{\theta n}$ is the net strain at the site. The resonance peak of the U-line is due to ions from set A of Ham's model, i.e. those which have their tetragonal axis aligned with the {001} axis. Hence the applied stress caused a compression along the tetragonal axis of the contributing ions, and, from this, it may be conlcuded that $e_{\theta min}$ corresponds to a compression from stable distortion of the ion. It is not possible to say whether the contributing ions are on sites which exhibit a net tetragonal compression or extension by comparison with the cube, since this will depend on the magnitude and sign of the Jahn-Teller distortions of the ion (which in turn, are connected with the parameter β), however, it can be said that ions which contribute to the resonance exhibit a net compression by comparison with the stable state.

(iv) The application of the maximum applied stress available made only a small change in the intensity of the absorption peaks. From this it may be conlcuded that the maximum value of the strain resulting from the applied stress is less than the mean value of the random strain on the lattice. This supports the previously assumed value of mean random lattice strain as $>10^{-4}$, since the maximum applied stress (hanging mass) results in a value of $e_{\theta} = 1.86 \times 10^{-4}$. It should be noted that Lange (1976) assumes a value of mean internal lattice strain of $\sim 10^{-5}$, but his samples

are very lightly doped by comparison with the 800-900 p.p.m of the present samples, and hence a lower value may be expected.

CHAPTER 5

THE CHROMOUS ION IN CaO

5.1 Introduction

Calcium oxide (CaO) in crystal form has a cubic lattice. Substitution of chromous impurity ions for the calcium ion gives a system basically similar to Cr^{2+} in MgO (Chapter 4). The lattice spacing, a, of CaO is however 2.4Å whereas that of MgO is 2.1Å, so the effects of the nearest-neighbour field will differ, and the parameters of the energy level diagram will vary from those of Cr^{2+} in MgO.

A range of crystalline samples were available, all grown in the same melt, but varying greatly in colour from pink through red, purple and green to nearly opaque black. APR experiments had been performed previously on these samples (Rampton et al (1972)) with moderate success. The observed signal to noise ratio was poor and sample echos were small. It was concluded that the difficulty in optically polishing the hydroscopic CaO to the required standard was a cause of this effect. The present experiments were performed on samples polished with oil-based polishes on a Multipol polisher, described in Chapter 3, with better results. An ESR spectrometer, described in Chapter 3.9 was constructed, and room temperature ESR experiments were performed on each sample, as well as APR experiments. The purpose of these experiments was to investigate any connection between chromous and chromic content and sample colour. No chemical analysis of the sample impurities was available.

APR experiments were performed on samples with high chromous concentrations. The experiments were of two types: (i) Variation of the angles θ and ϕ defined in Figure 3.7 (ii), to investigate

the theory of Fletcher (1971) (and section 5.3) that the resonance lines become sharper if the magnetic field is aligned with a trigonal axis. The <111> axis of the sample, which exhibits C_3 rotational symmetry, was considered as a trigonal axis.

(ii) Variation of the quantum frequency and experimental temperature to provide data for computer-fitting. To give values for the parameters 3Γ , K' and g, and hence to present an energy level diagram for the low-lying levels.

The layout of this chapter has been arranged such that all experiments of one type have been grouped together in one section. It should be noted that this was done for conciseness and does not represent the chronological order in which experiments were performed. The sections are:-

5.2 Previous work on Cr in CaO.

5.3 Theoretical background.

5.4 Experiments to determine the relationship between sample colour and chromous/chromic concentrations.

5.5 The effect on the APR spectrum of field orientation, 4.2K.

5.6 The effect on the APR spectrum of frequency and temperature change.

5.7 Discussions and conclusions.

5.2 Previous Work

(i) Rampton et al (1972) investigated the APR of Cr^{2+} in MgO, CaO and Al_2O_3. The purpose of the paper was to investigate the resonant behaviour of the systems at magnetic fields up to 5.5 T, to supplement the results available for lower magnetic fields. It was found difficult to prepare CaO samples to the required standard of polishing, and that the resonant absorption peaks were small, hence few experiments were performed on this material. The results presented for CaO have a field orientation defined by $\phi = 45^{\circ}$, $\theta = 36^{\circ}$ (Figure 3.7(ii)). This direction is close to the <111> direction of the sample. Six peaks were identifiable, all at fields less that 0.6 T. Isofrequency curves showed two-fold symmetry about the cubic axis of the crystal, and the better-defined lines fitted the expression

$$H = H_o \sec \chi$$

where Ho = resonant field of the line for $\underline{H}$ along the cubic axis.

χ = angle between $\underline{H}$ and the cubic axis.

No full fit of the data was possible, but from a preliminary attempt at a fit it was conlcuded that for Cr^{2+} in CaO $3\Gamma <$ K and $\beta > 0$, contrasting with the situation in MgO (Chapter 4).

(ii) Low and Rubins (1963) investigated the ESR of various iron group and rare earth impurities in CaO. Amongst the iron group ions considered was Cr^{3+}. Experiments were performed at room temperature, and at 77K, in liquid nitrogen. A single line of width 5 gauss was observed at room temperature and a line of width 1.5 gauss was observed at 77K. The hyperfine structure of Cr^{3+} was also observed at the lower temperature.

The basis of Low and Rubin's work was to compare the results obtained for the doped CaO with available data for the same impurities in MgO and CaF_2. It was predicted that the larger lattice spacing of the CaO group compared with MgO would produce a reduction in the g-factor of Cr^{3+} in MgO (i.e. a greater variation from the free-election value). The analysis was of the form

$$(g - ge) \alpha \frac{\lambda'}{\Delta}$$

where g = effective g-value

ge = free-electron g-value

λ' = spin-orbit coupling constant

Δ = cubic field splitting

$$\therefore \quad \frac{\lambda'}{\Delta}_{CaO} \qquad \frac{\lambda'}{\Delta}_{MgO} = \frac{(g - ge)\ CaO}{(g - ge)\ MgO}$$

The predicted value for this ratio was 1.95 (based on a point-charge model calculation). Experimentally it was found that the ratio was 1.30, and that

$$g = 1.9732 \pm 0.0005$$

(c.f. 1.9800 and 1.9803 $\pm$ 0.0005 values for Cr^{3+} in MgO)

It was concluded that the inaccuracy of the theoretical prediction was due to a symmetrical contraction of the ligand octohedron produced by the extra positive charge on the Cr^{3+} ion that replaces the Ca^{2+}. Studies of the other replacement ions led Low and Rubins to conclude that the comparison between the ESR spectra of the same ion in CaO and MgO showed that the differences were consistent with, and explicable by, a point charge model identical to that used for MgO, but with a weaker interaction due to the increased lattice separation.

Since the publication of the Low and Rubin's paper, iron-group impurities in MgO have been shown to be subject to a Jahn-Teller effect. The variations between theory and experiment in their results may be attributed to this effect not being taken into consideration in making the theoretical predictions, although Cr^{3+} is weakly coupled to the lattice and hence (Chapter 1) may not be expected to exhibit a strong Jahn-Teller effect, if any at all.

5.3 Theoretical Interpretation of Cr^{2+} in CaO

The theory of Cr^{2+} in CaO is basically similar to that of Cr^{2+} in MgO, since CaO and MgO are chemically similar materials and both exhibit cubic lattice symmetry. The lattice constant of CaO is, however, larger than that of MgO, and hence the various parameters (3Γ, K etc) may be expected to differ from those of MgO.

Fletcher (1971) investigated the relationship between lattice strain and resonant magnetic field for ions which are on sites of trigonal symmetry. When the magnetic field is along the <111> direction of a cubic system the symmetry will be trigonal. Resonance edges may be expected at turning points in the strain vs resonance field curve (Fletcher and Stevens, 1969). Fletcher was able to show that, for $\underline{H}$ along a trigonal axis, such a turning point occurs at zero strain and hence observations of unstrained sites may be made. Spectra observed under these conditions will be much sharper than those with $\underline{H}$ in the (010) plane, since the lines will not exhibit large strain-broadening. The experimental system used in this work (Figure 3.7(ii)) allowed the sample to be rotated in such a way that the field was aligned with the <111> axis of the CaO crystal. This axis exhibits three-fold symmetry (C_3 of the cube group O), and is hence a trigonal axis.

A description of Fletcher's reasoning is given by Bates (1978) in his review "Jahn-Teller Effects in Paramagnetic Crystals" pp 183-184.

The Hamiltonian which is set up is

$$\mathcal{H}_{ion} = [g_1\beta \underline{H}.\underline{S} + j\beta H_z S_z] + p[aS_z + f\beta H_z + \epsilon_E E_z] T_3$$
$$+ q[(g_2\beta E_\theta^{SH} + l\beta T_6^{SH} + V_E Q_\theta + \epsilon_E E_x) T_1$$
$$+ (g_2\beta E_\epsilon^{SH} + l\beta T_5^{SH} + V_E Q_\epsilon + \epsilon_E E_y) T_2]$$

The parameters j, a, f and l are all dependent on the trigonal field. Usually a is the most important, $j \ll g_1$ and f and $l \ll g_2$. The separation between two energy levels of $\mathcal{H}_{ion}$, Δ_o, may be written as a power series in magnetic field (Hx, Hy) and strain (e_θ, e_ε), provided these variables are small. When H is along the trigonal axis the components Hx, Hy are small, and consideration of the theory of MgO : Cr^{2+} (Chapter 4, section 3) shows that e_θ e_ε are small for ions which contribute to the resonance in that (similar) case. The series, up to third order, is given, by Bates as:

$$\Delta_0 = C_0 + C_1(H - H_0)\cos\chi + C_2 e_+ e_- + C_3 H_+ H_- + C_4 e_+ H_-$$
$$+ C_4^* e_- H_+ + C_5 e_+^3 + C_5^* e_-^3 + C_6 e_+^2 H_+ + C_6^* e_-^2 H_-$$
$$+ C_7 e_+ H_+^2 + C_7^* e_- H_-^2 \quad ----$$

where χ is the axis between H and the c-axis

Ho is the resonant field at $\chi = o = e$

$H_\pm = H \sin\chi\, e^{\pm i\psi} \sim Ho \sin\chi\, e^{\pm i\psi}$

$e_\pm = e_\theta \pm i e_\epsilon$

The series expansion may now be considered incorporating the conditions of the system:

Resonance condition $\Delta o = h\nu$ ..... (i)

Sharp resonance line (H constant for small changes in e)

$$\left[\frac{\partial H}{\partial e}\right]_{\chi,\psi,\Delta_o} = \left[\frac{\partial H}{\partial e}\right]_{\chi,\psi,\Delta_o} = 0 \text{ ..... (ii)}$$

$(\text{or} H\pm, \Delta_0)$ $(\Delta_0 H\pm)$

Also $d\Delta_0 = dH_{\pm} = 0$ ..... (iii)

Hence $dH = -(\partial H/\partial \Delta)_{H\pm, e\pm}[(\partial \Delta_0/\partial e_+)_{H_{\pm}, e_-, H} de_+ + (\partial \Delta/\partial e_-)_{H\pm e_+ H} de_-] = 0$

Now $(\partial H/\partial \Delta)_{H\pm, e\pm} \neq 0$ from (ii), above,

thus $(\partial \Delta/\partial e_+)_{H, Ht, e_-} = (\partial \Delta/\partial e_-)_{H, Ht, e_+} = 0$

These results may be substituted into the power series expansion, giving

$$0 = C_2 e_- + C_4 H_- + 3C_5 e_+^2 + 2C_6 e_+ H_+ + C_7 H_+^2$$

= complex conjugate of above

These equations may be solved in $e \pm$, giving the result that $(H - Ho)$, the change in the resonant field of the edge or sharp line, is dependent on χ and ψ only. If constant $C_2 >> C_5$

then $e_{\pm} \approx -(C_4^* / C_2) H_+$

Hence for $\chi = 0$ (H along the trigonal axis), the edge occurs for $e \pm = 0$

If $C_5 >> C_2$ then

$$e_+ = \pm b\sqrt{H_-} \qquad \text{and} \quad e_- = \pm b\sqrt{H_+}$$

Hence for both cases the resonance occurs at $e = 0$, zero strain for H along the trigonal axis. Experiments were carried out with H along, near to, and far from the trigonal (<111>) axis, such

that the effect of observing sites at zero strain could be noted. One important implication of these conclusions is that resonances observed with the field along <111> should be sample independent, as it is the change of random internal strain at the impurity site from sample to sample that makes spectra observed away from <111> sample dependent.

5.4 Experiments to Determine the Relationship Between Colour and Impurity Concentrations of the Samples : APR and ESR.

The samples were prepared from specimens of crystalline CaO doped with chromium, provided by Dr B Henderson of Keele University (now Professor of Physics, Trinity College, Dublin). The original specimens varied in colour, and samples were prepared from each identifiable colour in the material. Table 5.4 (i) shows the sample nomenclature and a description of the colours. Each sample was X-ray aligned along the <100> direction and then ground into a rectangular block. The end faces were optically polished. APR experiments were carried out on each sample, at 4.2K with various field orientations (see Figure 3.7(ii)). It was observed that the greatest absorptions occurred in the pink samples, whilst no resonant absorptions at all occurred in the green samples. (Figure 5.4(i)).

A room temperature ESR experiment was then performed on each sample. Firstly, the magnetic field was swept from zero to maximum (~ 1T) to observe the total ESR spectrum, and then the field was swept more slowly through areas of particular interest. It was observed that all samples exhibited the six sharp lines attributed to Mn^{2+}, and a smaller line between two of the Mn^{2+} lines, attributed to Cr^{3+}. No other structure was observed (Figure 5.4(ii)). In each case the second field sweep was therefore limited to the region in which the

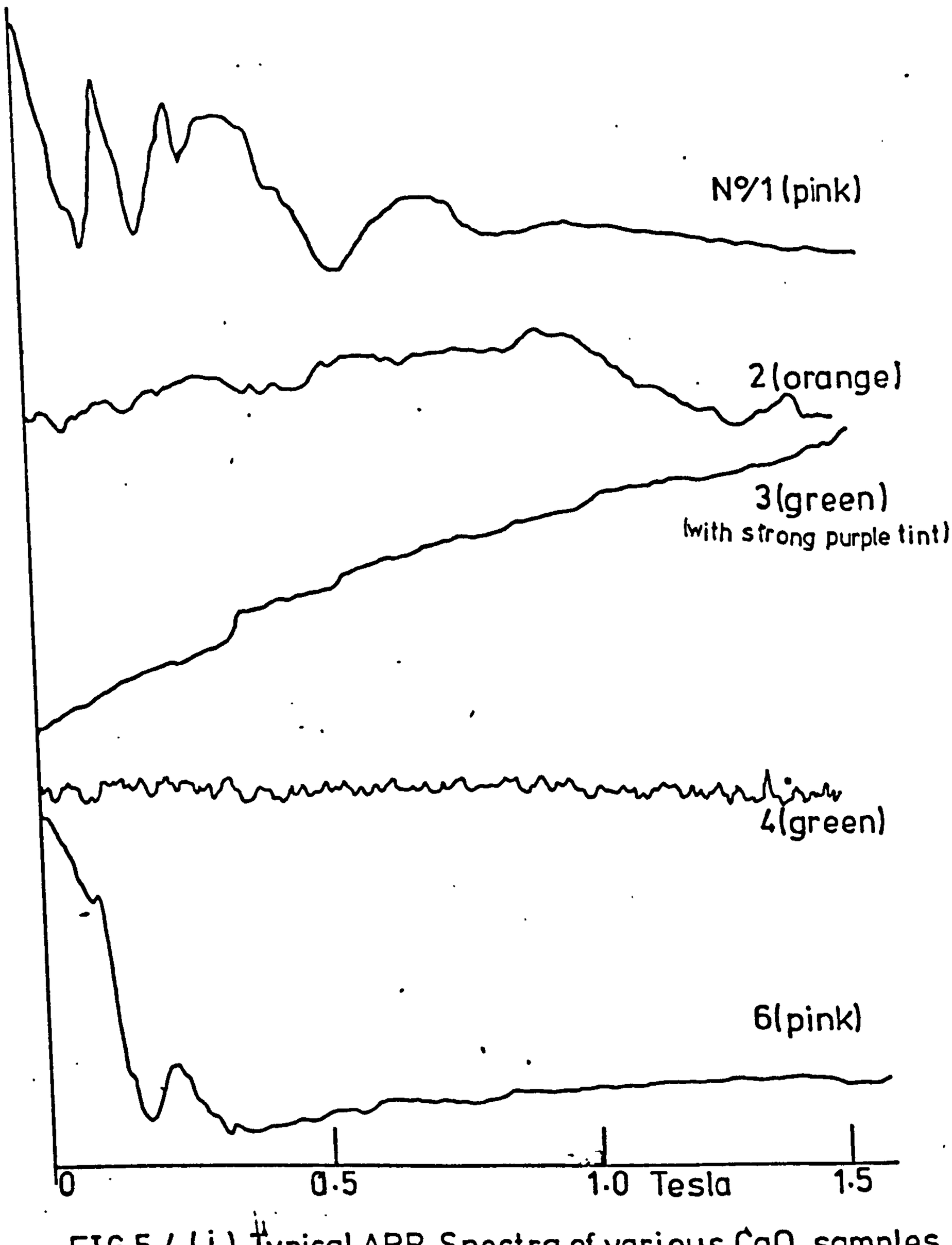

FIG 5.4.(i). Typical APR Spectra of various CaO samples 9.5 GHz, 4.2K, various orientations.

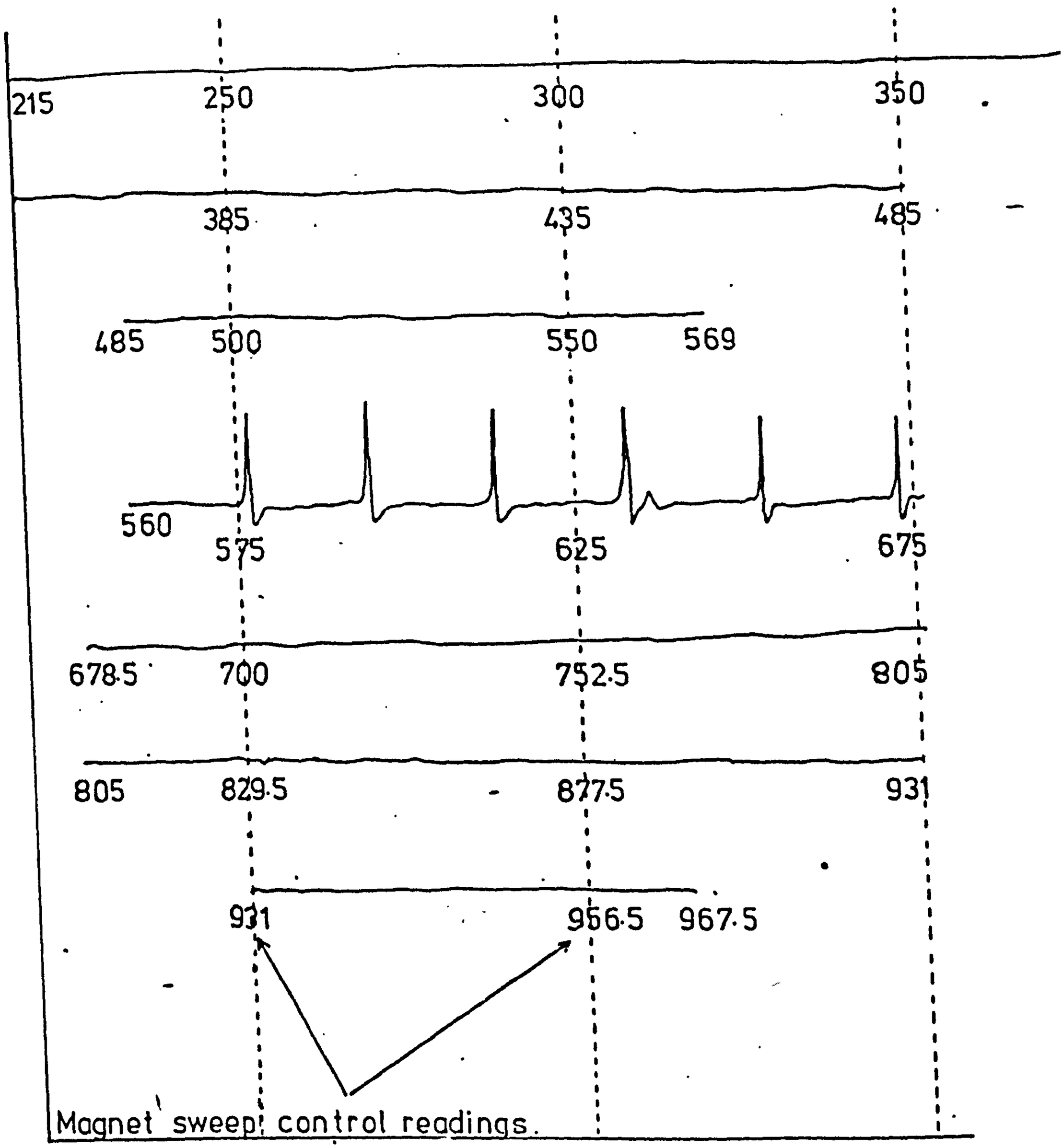

FIG.5.4.(ii). ESR trace of Cr:CaO N°1 (pink), from H=0 to maximum field (~1T). (Room temp.).

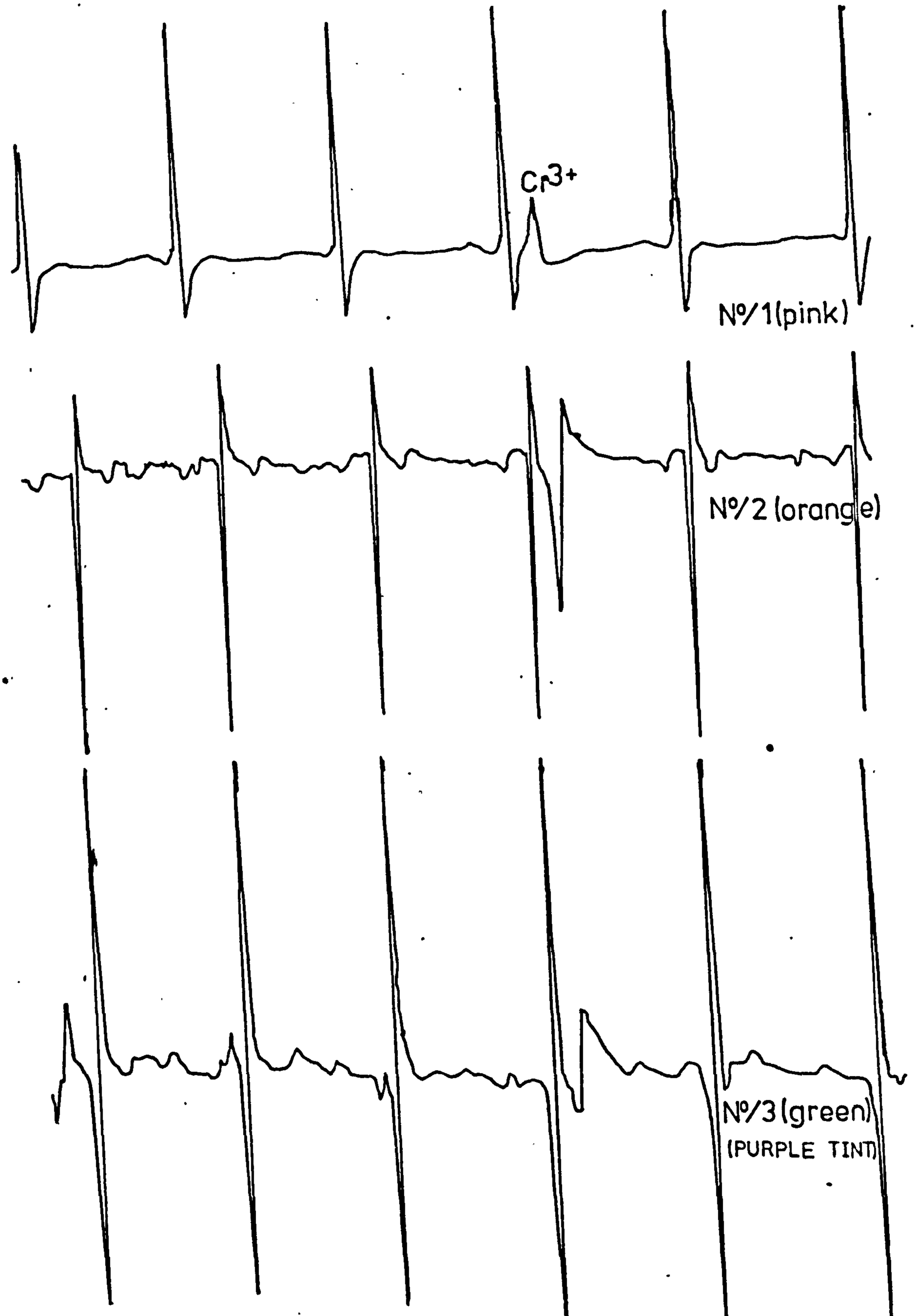

FIG 5.4(iii) ESR Spectra of CaO samples in the region of
(a) the Cr^{3+} line.

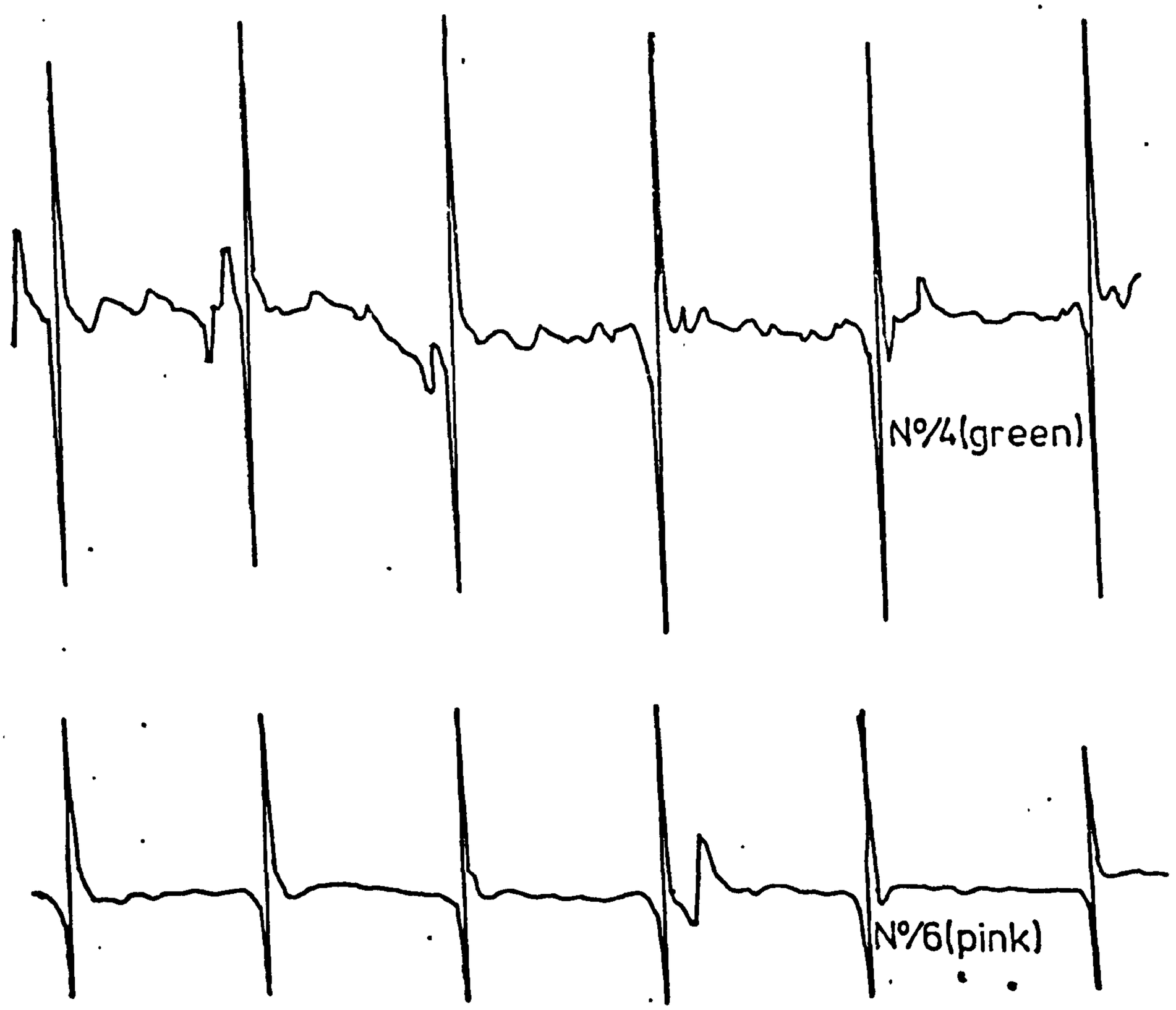

FIG5.4.(iii)(b) [all plots at room temperature, frequency in the range 9.3 to 9.6GHz]

six Mn^{2+} and the one Cr^{3+} lines appeared. It was observed that the relative heights of the Mn^{2+} and Cr^{3+} lines were sample dependent (Figure 5.4(iii)).

5.5 The Effect on the APR Spectrum of Field Orientation

Samples CaO : Cr Nos/ 1 and 6 were chosen for further experiments since these samples exhibited the best APR absorptions in the experiments of section 5.4, above. Spectra were recorded for variations of both θ (in the x-y plane of the laboratory frame, Figure 3.7(ii)) and ϕ (in the y-z plane). Observations were made at ten degree intervals of ϕ between 0° and 90° and at $\phi = 45^\circ$ for each of ten degree intervals of θ between 0° and 90°, and at $\theta = 57.5^\circ$ and 54.8°. Results are presented for variation in θ for $\phi = 0$ (Figure 5.5(i)). This corresponds to the situation of the experiments of Chapter 4, and direct comparison can be made with Figures 4.4(i) and 4.6(i). Figure 5.5(ii) shows the spectra for variation of θ for $\phi = 45^\circ$. In this case, the field is rotating between the [100] and [011] directions. Hence if $\theta = 54.8$ the field along the [111] direction. Figure 5.5(iii) compares the spectra for field along [111] and for $\phi = 45^\circ$ $\theta = 57.5$ which is near the [111] direction.

5.6 The Effect on the APR Spectrum of Frequency and Temperature Change.

To identify whether the transition giving rise to a resonant absorption was between levels which separated or closed under increasing magnetic field, experiments were performed at two different frequencies. This allows the resonance conditions to be satisfied by quanta of two energies and two resonant fields, giving both the magnitude and sign of g. Two methods were used to obtain the different frequencies:-

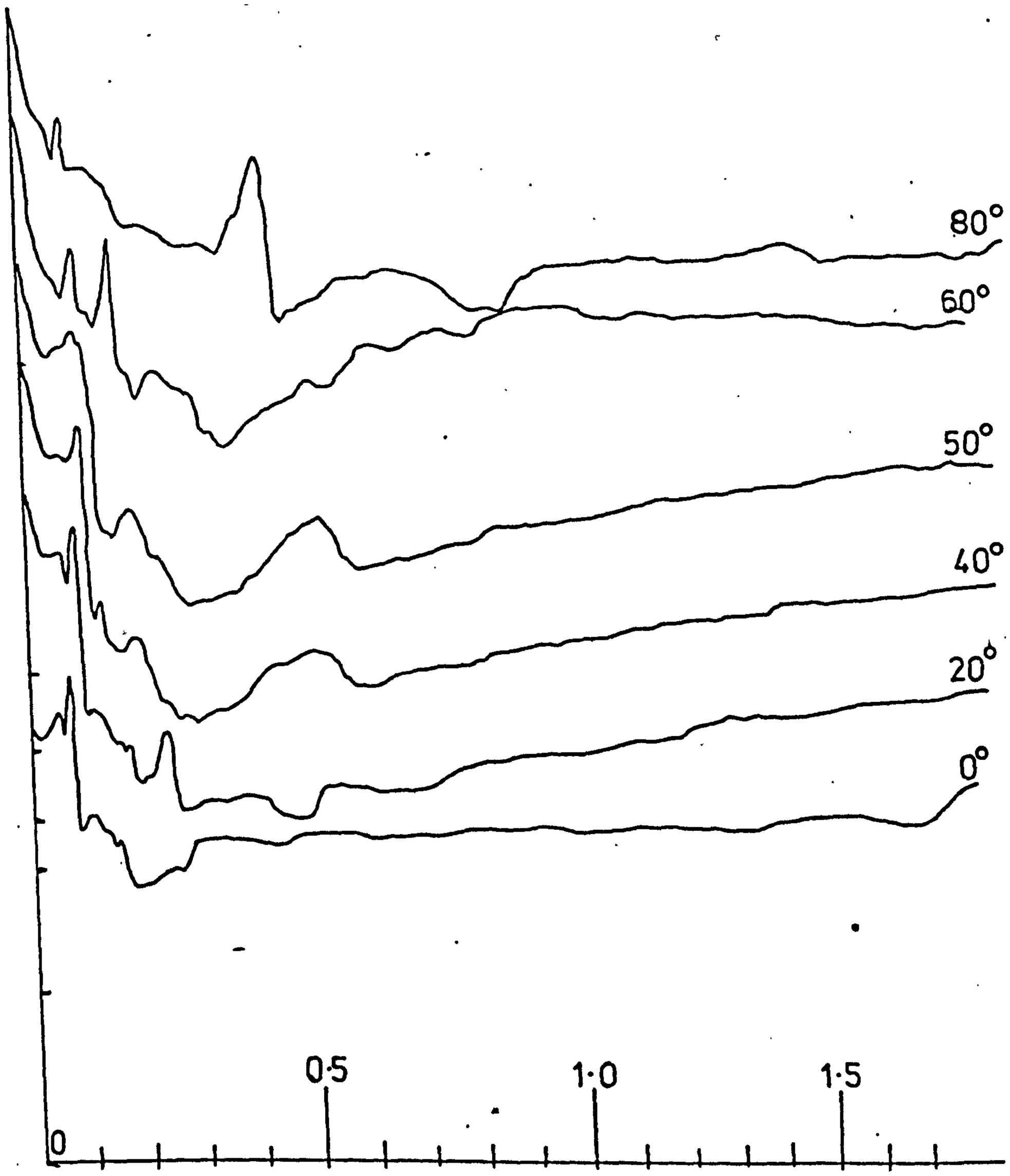

FIG 5.5.(i) Spectra of CaO:Cr N°/1, $\phi = 0°$, θ varied.
4·2K, frequency 9·5 GHz

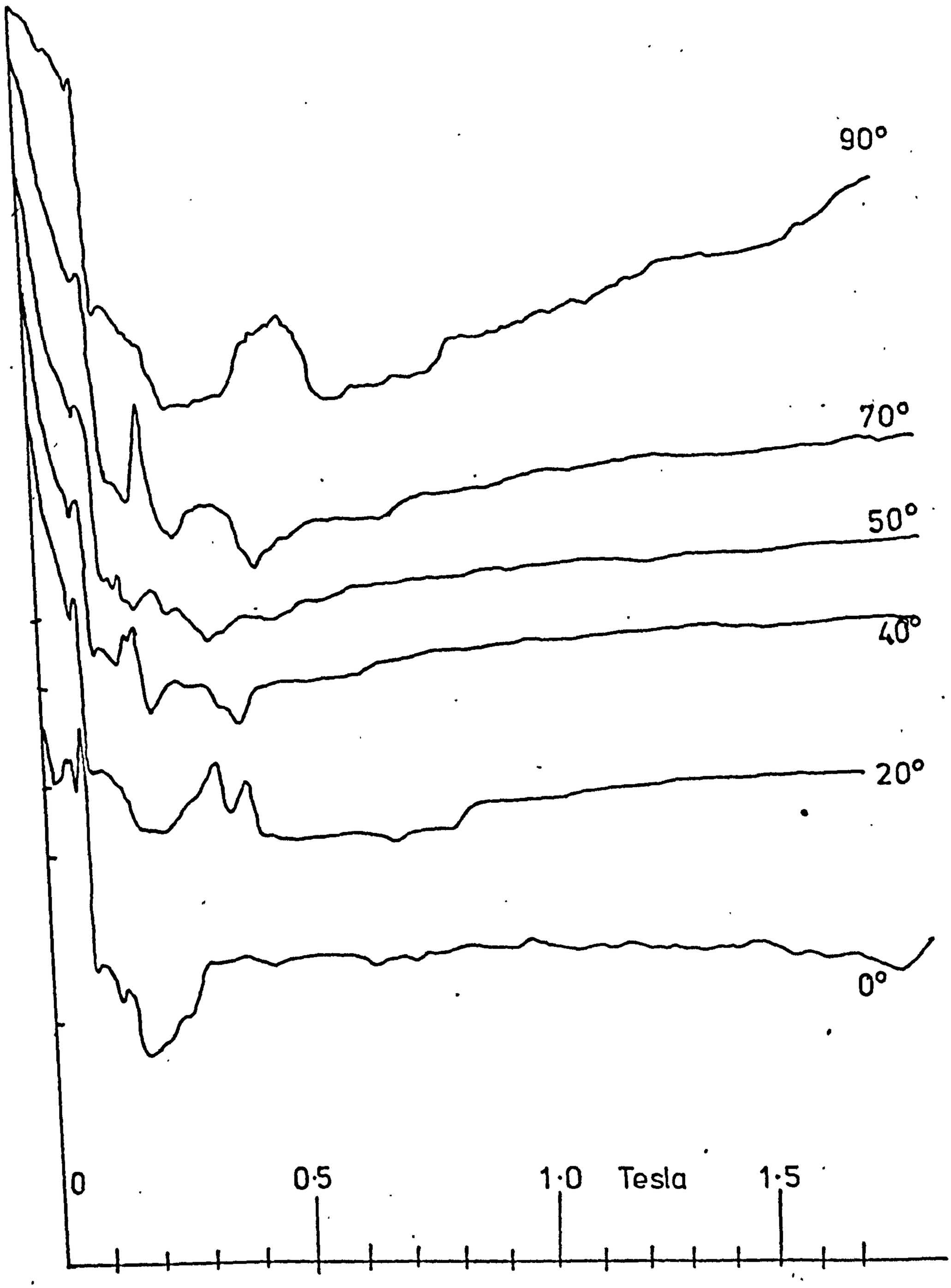

FIG 5.5(ii) Spectrum of CaO:Cr N°/1, $\phi = 45°$, θ varied from 0° to 90°. T=4.2K f=9.5GHz.

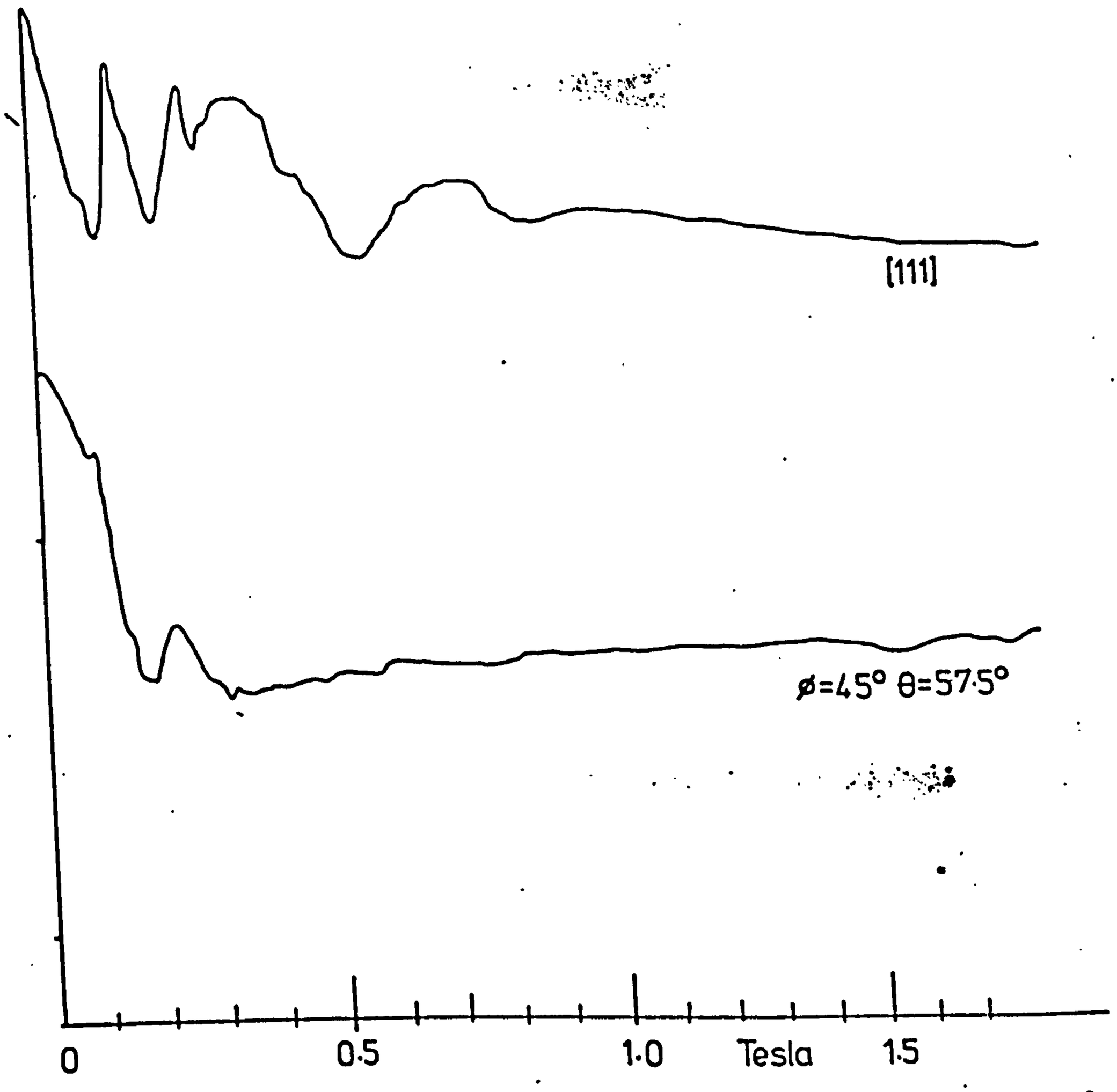

FIG 5.5.(iii). Comparison of the spectra of Cr:CaO N°1 at 4.2 K, f=9.5 GHz, for magnetic field along and close to the [111] axis.

(i) Moving the quartz rod in and out of the cavity causes the cavity resonant frequency to change.

(ii) A cryostat was constructed which had the cavity placed vertically along side the waveguide, and coupled to the microwaves via a looped wire coupler. A turning loop which could be moved from outside the cryostat by means of a threaded rod passing through an o-ring seal was fitted around the post. The range of frequency that could be obtained using this device was well beyond the tuning range of the magnetron. The design of this system, however, introduces two factors which reduce the signal. Firstly, the Q-factor of the cavity is very much lower than that of the cavity used in the other cryostats. Secondly, the length of the cavity is such that instead of the greatest part of the electric field in the cavity occuring between the post and the end face of the quartz transducer, another concentration of electric field occurs further down the cavity. For these reasons the signal echos were well down into the receiver noise. Hence the system of moving the quartz rod in the cavity and performing more than one experiment was used. The disadvantages of this system are that the system has to be brought up to room temperature to change the frequency, and that, since the cavity resonant frequency changes as it cools to 4.2K, the exact frequency of the experiment cannot be predetermined. Figure 5.6(i) shows the spectra obtained for phonons of frequency 9.5 GHz and 9.75 GHz, magnetic field along [111] axis and temperature 4.2K.

If the temperature is changed the population of the contributing levels may change, and this will be shown in the spectrum by a change in the intnesities of the absorption lines. In these experiments the temperature was lowered to 2K, since bubbling of the liquid helium on cooling, which makes observations impossible, stops when the temperature falls below the lambda point (2.18K), and the 50% change in temperature was thought sufficient for information about population densities to be obtained. Figure 5.6(ii) shows the effect on the spectra

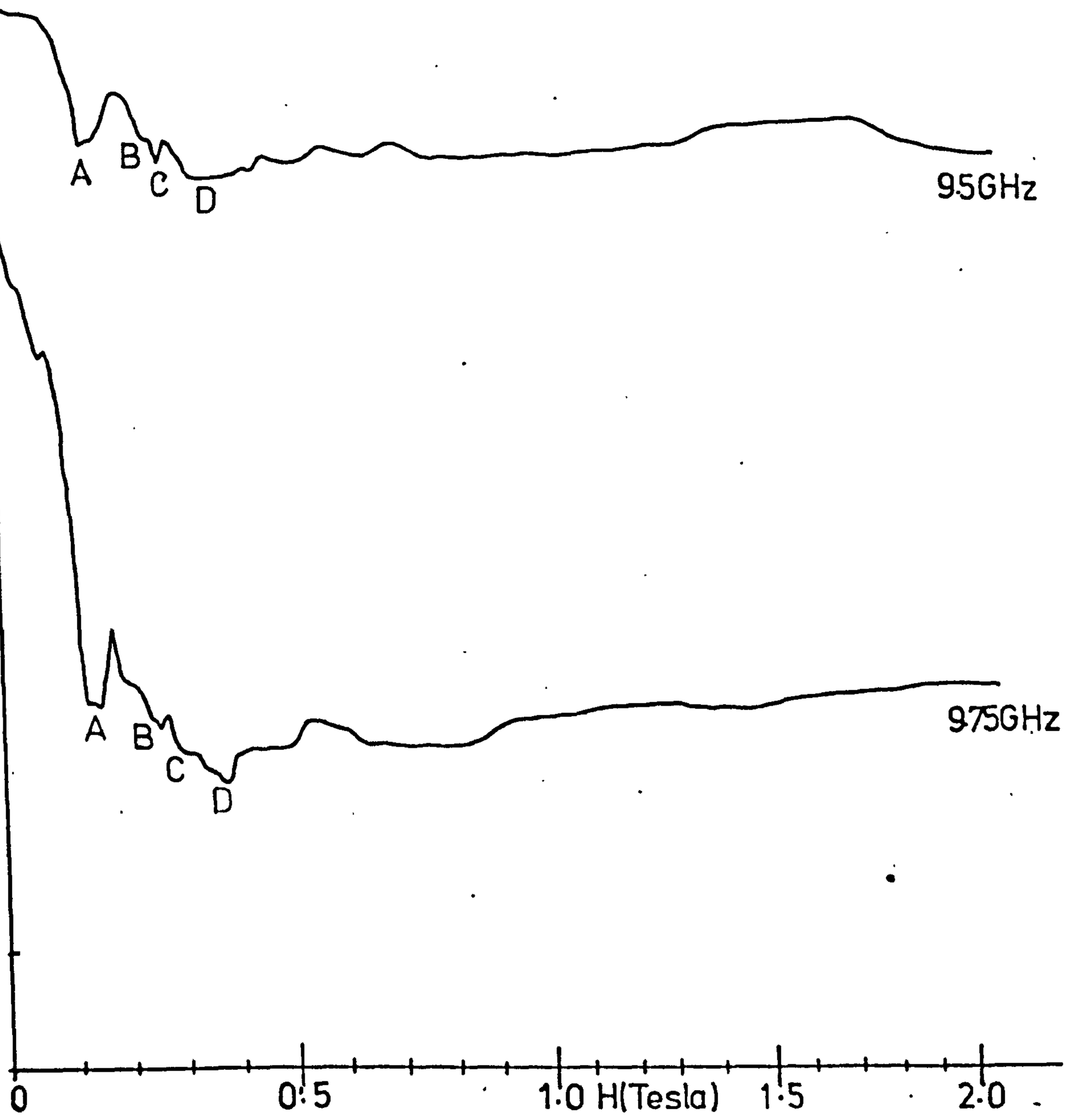

FIG 5.6.(i). Spectra of CaO:Cr N°/6 with H along [111], Temperature 4.2 K, frequencies 9.5 and 9.75 GHz

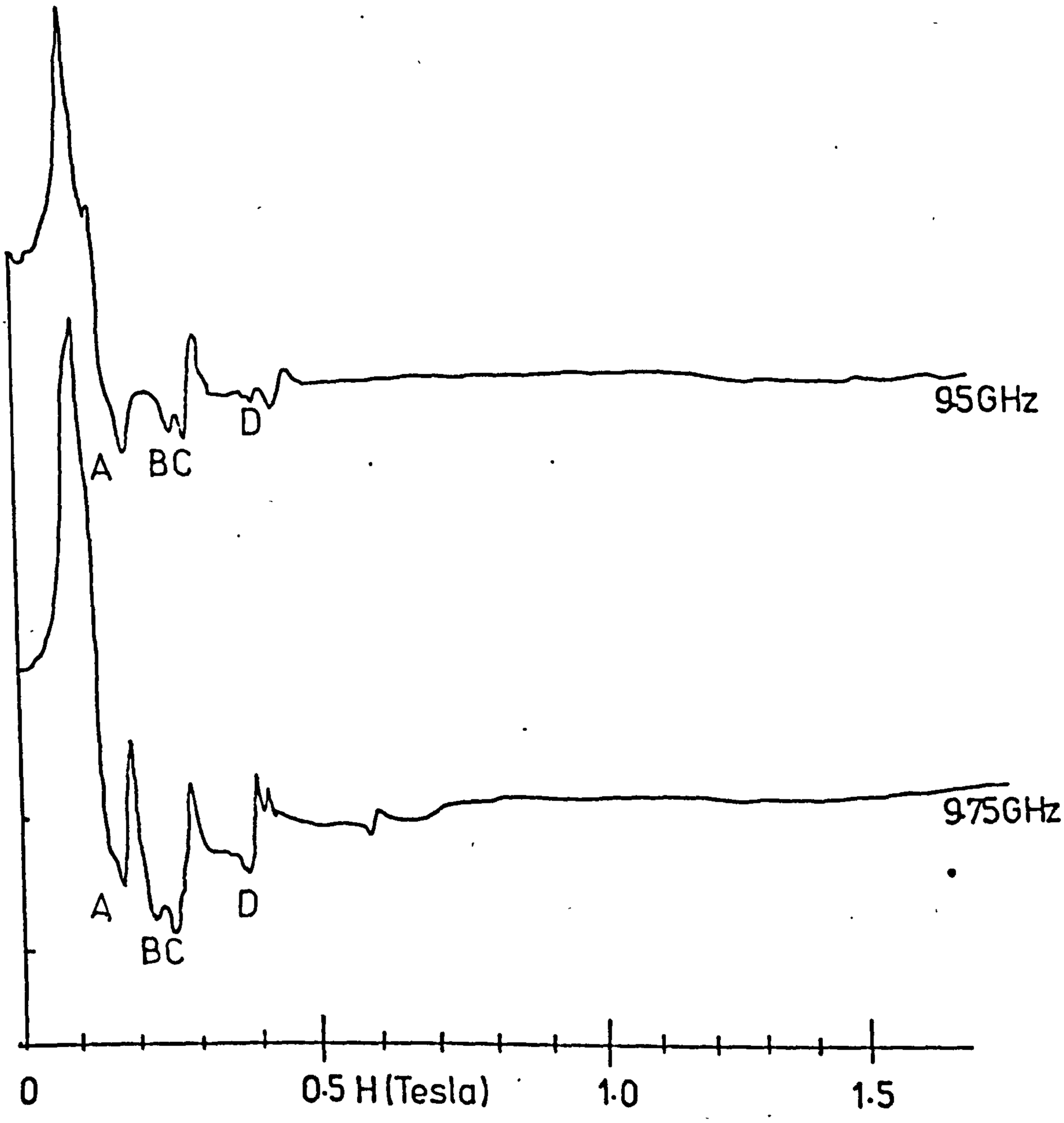

FIG 5.6.(ii) Spectra of CaO:Cr N°6 with H along [111], temperature 2K, frequencies 9.5 and 9.75 GHz.

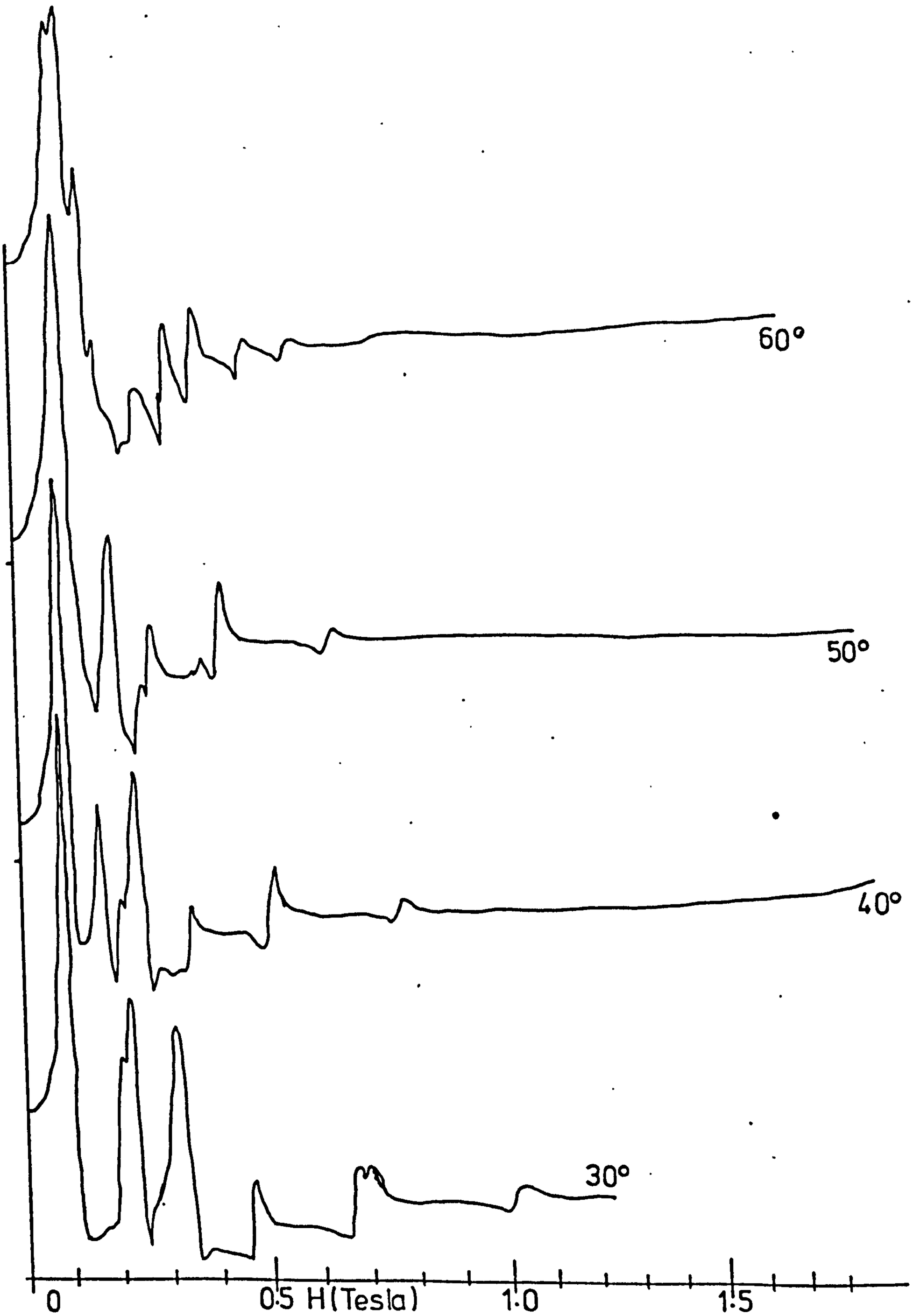

FIG 5.6(iii) CaO:Cr N°/6, 2·0K, 9·75GHz, ϕ=45° , θ varied.

of Figure 5.6(i) of changing the temperature to 2.0K.

Figure 5.6(iii) shows the effect on the spectrum of sample CaO : Cr N°/ 6 of varying θ with $\phi = 45^{\circ}$, temperature 2K and phonon frequency 9.75 GHz. The change in position of the resonance lines with θ may be compared with Figure 5.5(ii), and hence the identification of the lines checked.

Since the difference in energy between phonons of frequency 9.5 GHz and those of 9.75 GHz is small, it is very important that the resonant frequencies of the lines are accurately measured. The Hall probe used to measure magnetic field is linear in the field range of the Cr^{2+} resonances in CaO but absolute calibration accuracy between runs can only be guaranteed to about $\pm$ 1%. Hence some form of calibration check for the results is required. In these experiments the position of the line attributed to Fe^{2+} was used as this calibration point. This line was identified by its isotropy and g-factor. Knowing this g-factor and given the isotropy of Fe^{2+} resonances, the calibration of the field could be checked from run to run.

5.7 Discussion and Conclusions

5.7(i) Comparisons Between Sample Colour and Chromous Content

There are two reasons why a sample may not exhibit APR due to the chromous ion:

(i) The chromium content of the sample is very low.

(ii) Most of the chromium is in the chromic state.

No quantitative measurements could be made, since no chemical analysis of the samples was available, but comparisons could be made between the results of ESR and APR experiments on each sample. The chromous ion is strongly coupled to the lattice, and should contribute, with other weakly coupled ions, to the ESR spectrum. Comparison of

No/	COLOUR	CHROMOUS	CHROMIC*
1	PINK	Strong APR, implies high Cr^{2+} content.	0·21
2	ORANGE	Weak APR, low content of Cr^{2+}.	0.60
3	GREEN/ PURPLE	No APR, very low content of Cr^{2+}.	0.19
4	GREEN	No APR, very low content of Cr^{2+}	NO CHROMIC LINE OBSERVED
'6	PINK	Strong APR, high Cr^{2+} content.	0·31

TABLE 5.7.(i). Comparisons of Cr:CaO samples.

*height of Cr^{3+} line (ESR) ÷ height of 4th Mn^{2+} line

the results of ESR and APR experiments thus enable other impurities in the sample to be identified, and comparison of the chromic and chromous contents of the samples to be made in a qualitative way. Figures 5.4 show that strong APR absorptions were observed for samples CaO : Cr N^{os}/ 1 and 6, but not for N^{os}/ 2, 3 and 4. (NB Sample N^{o}/5 was prepared with the end faces perpendicular to <110> for use in the magnetically coupled cryostat, and thus was not included in this survey). Both samples 1 and 6 were pink in colour. Sample N^{o}/ 2 (orange-red) showed weak APR absorptions, whilst samples 3 and 4 (green) showed no APR at all. Hence it may be inferred that the pink samples contain more of the chromous ion than the other colours. The results of the ESR experiments are more difficult to interpret. The spectrum shown in Figure 5.4(ii) shows six sharp lines attributed to Mn^{2+}, and one line, close to the fourth manganese line in order of magnetic field, attributed to the chromic ion. Figure 5.4(iii) shows that this chromic line is present in all but one of the samples.

The intensity of the chromic line may be expressed as a fraction of the intensity of the adjacent (fourth) Mn^{2+} line, and, assuming the Mn^{2+} concentration in the samples to be constant, a quantitative idea of the chromic concentration in one sample compared with any other may be obtained. It should be noted that this assumption cannot be justified for two reasons:

(i) In the absence of a chemical analysis, it cannot be shown that the total manganese concentration in all samples is the same.

(ii) It cannot be assumed that, even if the total manganese concentration is sample independent, the proportion in the divalent state is always the same.

For the purposes of this analysis, however, the assumption was made, and table 5.7(i) shows the results of the sample survey. Colour, APR result (qualitative), and the intensity of the ESR chromic line as

a function of the intensity of the fourth manganous line are presented.

It was concluded that the maximum chromous concentration occurred in the pink samples, N^{os}/ 1 and 6. Sample 2 (orange) contained some chromous ions, whilst samples 3 and 4 (green) contained little or no chromous ions. The chromic concentration (making the above assumption) would appear to be nearly sample independent, except for sample N^{o}/ 4 which contains little or no chromic ions at all.

5.7(ii) The APR Spectra of Cr^{2+} in CaO

(a) Comparison of Figure 5.5(i) with the Results of Cr^{2+} in MgO

The variation of θ with $\phi = 0^{o}$ shown in Figure 5.5(i) is an identical experiment to those performed on Cr^{2+} in MgO (Chapter 4) in which external stress was not applied. Figure 5.5(i) may therefore be compared directly with Figure 4.6(i) which shows the APR of Cr^{2+} in MgO under similar conditions of temperature and phonon frequency. It is observed that only two lines attributed to Cr^{2+} occur on Figure 4.6(i) (lines U and C), whilse five lines attirubted to Cr^{2+} may be identified from Figure 5.5(i). Since the energy level diagrams of the two systems are qualitatively similar, it may be concluded that the energy separations of some of the levels of Cr^{2+} in CaO are less than those of Cr^{2+} in MgO, as more transitions are occurring.

(b) Variation of ϕ

It has been predicted (Fletcher, 1971) that if the magnetic field is aligned along the crystal <111> axis, then zero strained sites will contribute to the resonant absorption, and, thus, that strain broadening of the lines will be much less (section 5.3). The APR spectrum should become sharper under these conditions. Figure 5.5(iii) shows this effect by comparing the APR results for field along <111>($\phi = 45^{o}$, $\theta = 54.8^{o}$)

and a close orientation ($\phi = 45^{\circ}$, $\theta = 57.5^{\circ}$). It is observed that the sharpening of the spectrum does occur, and that this is extremely local to the <111> direction.

(c) Energy Level Diagram for Low-Lying Levels of Cr^{2+} in CaO

The resonance condition, which is of the form $h\nu = g\beta H_{res}$, may be satisifed for the resonant fields of the absorption lines for ν = 9.5 GHz and 9.75 GHz. The change in intensity of the resonance lines with changing temperature relates to the population of the line, and hence identifies whether it is a low or higher lying level. A computer fit of the results of Figures 5.6(i), (ii), and (iii) was made to determine the parameters of the energy level diagram. The results were:

3Γ { separation between first excited singlet and the mean energy of the spin-orbit levels, called the Jahn-Teller tunneling splitting} = $5.00 \pm 0.3 cm^{-1}$

K (spin-orbit splitting) = $1.20 \pm 0.30 cm^{-1}$

q (reduction factor) = $0.45 \pm 0.2 cm^{-1}$

Thus K' = qK (reduced spin-orbit splitting) = $0.54 \pm 0.35 cm^{-1}$

g (field splitting factor) = 1.92 ± 0.07. It was found that g could vary quite widely with little effect on the energy levels.

The resulting energy-level diagram may be seen to exhibit very low values of both spin-orbit and Jahn-Teller tunneling splitting. The results were obtained for the situation $\beta < 0$. These conclusions vary from those postulated by Rampton, et al (1971) in many ways:

(i) The suggestion that $3\Gamma < K$ has not been supported. The ratio $3\Gamma/K$ has been found to be in the range 3.13 to 5.88, with the mean value at about 4.

(ii) It was suggested that for this system $\beta > 0$. Again, this conclusion has not been supported as the present results give an

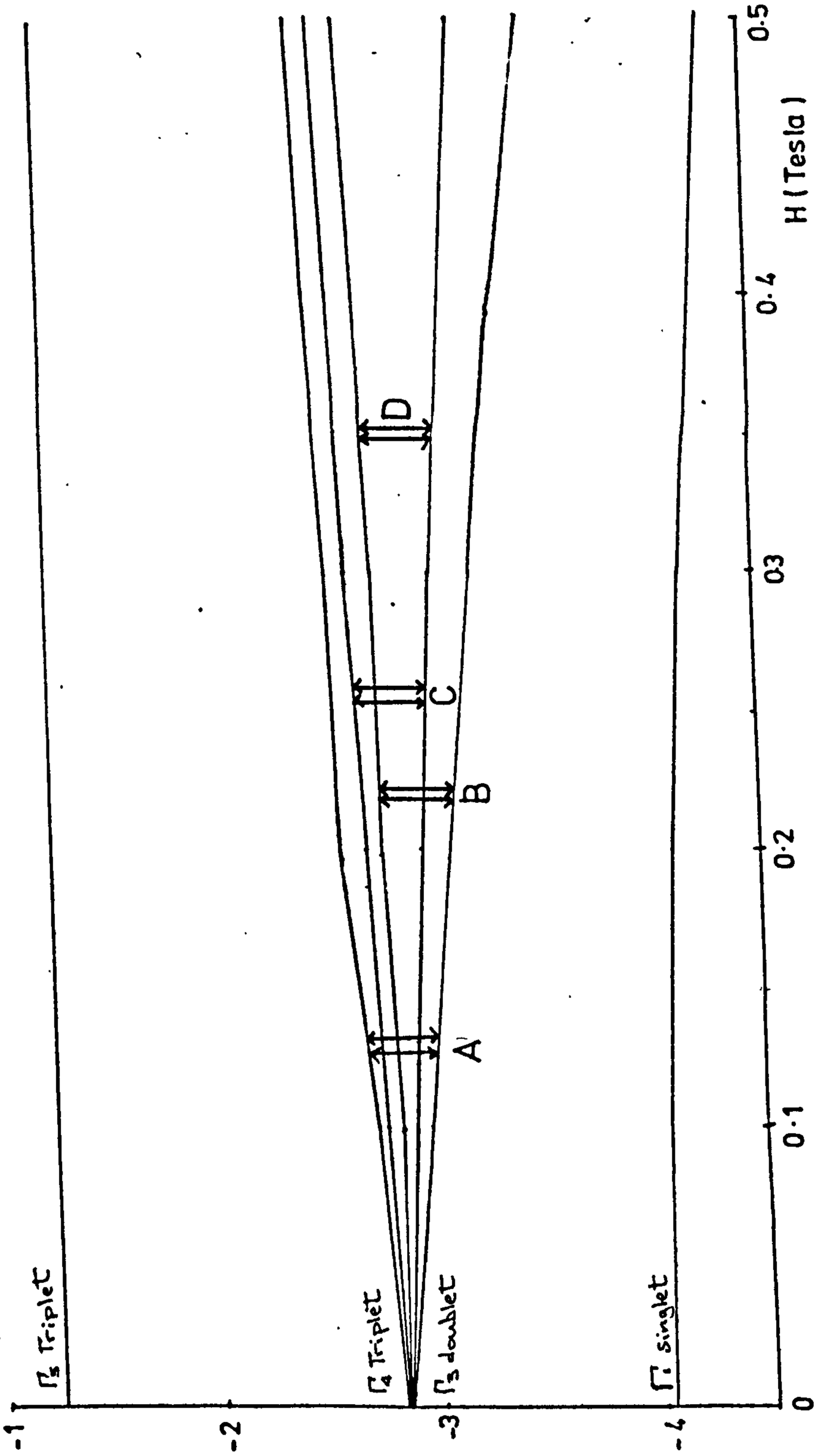

FIG 5.7.(i). Low lying energy levels of Cr^{2+} in CaO.

(drawn from computer analysis of results of sections 5.5 and 5.6. Transitions occur within the group of five levels)

energy-level diagram qualitatively similar to that of Cr^{2+} in MgO; for $\beta < 0$.

It may further be noted that the ratio $3\Gamma_5 / K \sim 4$ is similar to the prediction of the same ratio for Cr^{2+} in MgO (Chapter 4.3(ix)) supported by most results, and hence the suggestion that the systems are similar except for the increased lattice spacing would seem to be supported. It is interesting to note that these results predict $\beta < 0$, in agreement with the findings of Lange (4.3(ix)) that the data of Cr^{2+} in MgO could be better fit in this case.

The general conclusion which may be drawn is thus that Cr^{2+} in CaO is a Jahn-Teller system very similar to that of Cr^{2+} in MgO. The difference in lattice spacing a, ($a_{CaO} / a_{MgO} = 1.14$) results in a greater reduction in the energies of the low lying levels of Cr^{2+} in CaO by comparison with MgO, although the ratio of the Jahn-Teller tunneling splitting to the spin-orbit splitting is approximately the same for both systems. The g-values of both systems are similar (within experimental error) and some evidence is given to support the suggestion that the Jahn-Teller distortion corresponds to a compression along the tetragonal axis (i.e. $\beta < 0$) for both systems.

APPENDIX A

The Design of a Stockbarger-Bridgeman Furnace for Growing Single Crystals of Calcium Fluoride.

AA (i) General Introduction

The basis of the Stockbarger technique is that the crucible containing the melt is moved through a fixed temperature gradient, rather than the temperature being changed around a fixed crucible. The temperature gradient is provided by the use of a graphite heater of cylindrical bore which has walls of varying thickness. The resistance of the heater, and hence the temperature, depends on the wall thickness . The crucible is moved by an electric motor placed outside the furnace, connected to the crucible by a stainless steel driveshaft. The range of movement of the crucible is controlled by microswitches activated by stops on the driveshaft. In addition to the vertical movement, the crucible is also rotated (by a second electric motor) to ensure that the temperature distribution across the melt at any time is radially symmetric. Crystal growth is carried out under vacuum conditions. The vacuum was obtained using a Geneivac 6" diffusion pump backed by an Edwards ED220 rotary pump. An Edwards vacuum switch mounted onto the main outlet of the furnace chamber ensured that the heaters could not be switched on until a suitable vacuum had been obtained. The flow rates of cooling water needed for the vacuum pumps and the main furnace chamber were controlled by Edwards "Flowtrol" pressure switches. If the cooling water flow rate dropped below a safe value the furnace was switched off. A high-current circuit breaker enabled the furnace to be safely deactivated if the electrical power failed. The current to the heater was supplied by a motor-driven Variac, which had a manual override for setting up tests. The speeds of crucible motion and rotation were measured by calibrated tachometers, and the

vacuum pressure was measured by Pirani and Penning guages placed in the roughing/backing and main pumping lines respectively.

Single crystals of about 1cm diameter x 1.5cm length could be grown in the crucible, or, alternatively, higher numbers of smaller crystals could be grown using a crucible with more than one hole in it.

The heater was supplied ready made, with graphite for other parts to be machine in the department, by Le Carbone (GB) Ltd. Stainless steel parts for the furnace were manufactured in the department or were modified from existing equipment.

The furnace was assembled and the vacuum systems, control systems and water cooling systems and failsafes tested.

AA (ii) Furnace Data

Heater Dimensions

Length 19·5 cm

Bore 5·7cm

Thickness 2·5mm (upper) 9mm (lower)

Heater Supply

Current 115 Amps

Power 3·22kW

Cooling Flow-rates Required

Bottom Cover	2.5 L.P. Minute	(10 psi on Flowtrol)
Power Feedthroughs	0.6 L.P.M each	(∿ 3 psi)
Bell-jar Cover	5 L.P.M.	(25 psi)
Furnace Tank jacket	15 L.P.M.	(25 psi)
Pump cooling	2 L.P.M.	(18 psi)

The Flowtrol settings were determined by experiment and depend on flow-rate and the bore of the cooling water pipe.

No speeds were fixed for crucible movement and rotation, since this would be a variable parameter of crystal growth. A motion of approximately 1mm/hr was expected.

Maximum vacuum pressure obtained was of the order of 10^{-7} torr, heaters cool.

AA (iii) Acknowledgements

The furnace design was based on information provided by Dr D A Jones of Aberdeen University, and reference was made to Jones et al (1967) and the University of Aberdeen, Department of Natural Philosophy Annual Report, "Growing Pure and Doped Crystals from the Melt".

APPENDIX B

THE IMPATT DIODE

AB (i) Reasons for Use of the IMPATT Diode

There are many ways in which solid-state generators, such as the IMPATT diode can be used. The devices can be used pulsed or continuous wave (c.w.) and may be obtained in high or low power form. In the APR spectrometer used in this work three applications suggest themselves:

(a) Low power continuous wave to replace the local oscillator klystron in the receiver

It was decided not to use a solid state device here, as the receiver functioned well in its current form.

(b) Low power pulsed, to give calibration pulses.

Experiments had been carried out, in 1975 with Dr P J King into adding a calibration pulse into the spectrometer using a low powered magnetron and suitable attenuators. These were not successful for a number of reasons. It was decided that a low power, pulsed generator was required and a low power IMPATT diode was chosen.

The calibration pulse is used to measure the amount of acoustic power which is absorbed by a resonance by means of comparing the height of the calibration pulse against a sample echo. This removes any inaccuracy which may result from readings taken directly from the receiver, due to non-linearity in the receiver response under experimental conditions.

(c) High power pulsed, as a generator.

A high power IMPATT diode, in pulsed application, can deliver up to about 10 watts of power. Such a device can thus be used as a direct replacement for a magnetron as a microwave generator.

The IMPATT diode (in common with other solid-state generators) has a number of advantages over the magnetron as a generator.

(i) Size and power supply requirements. The magnetron requires a 1kV pulse to activate it. The circuit diagram of a magnetron supply is given in Figure 3.4(i). The IMPATT, however, requires a small comparatively low voltage supply. Since the magnetron is a high-voltage, low current device, its driver circuits are also high-voltage low-current valve circuits which are bulky, whereas the IMPATT is supplied by small, light-weight solid-state circuits.

(ii) Cost and availability. Both the magnetron itself and the valves required by its driver circuit are expensive and are not readily available. The IMPATT and its driver circuit components are cheaper (IMPATT $\sim$ £130, magnetron $\gtrsim$ £600) and more readily available.

(iii) Frequency range. The IMPATT, in a suitable cavity, has a greater frequency range available than the magnetron. This has obvious advantages in experiments of the type carried out in Chapter 5, and also facilitates the setting-up procedure of an experiment.

AB (ii) The Theory of the IMPATT diode

The word IMPATT is a contraction of the phrase "impact ionization avalanche transit time", which is a brief description of how the device works. Figure AB 1 is a schematic representation of a current-voltage characteristic for a typical p-n semi-conductor junction diode. When the applied voltage is negative (a reverse bias situation), a small current, known as the saturation or leakage current, (resulting from minority carrier flow) will flow through the device. If the reverse bias is increased, however, a voltage $-V_b$, known as the breakdown voltage, is reached at which a large current will flow, in a reverse direction, through the device. The slope of the graph in this region ($I_x \div (V_x - V_b)$) is large, such that large changes in

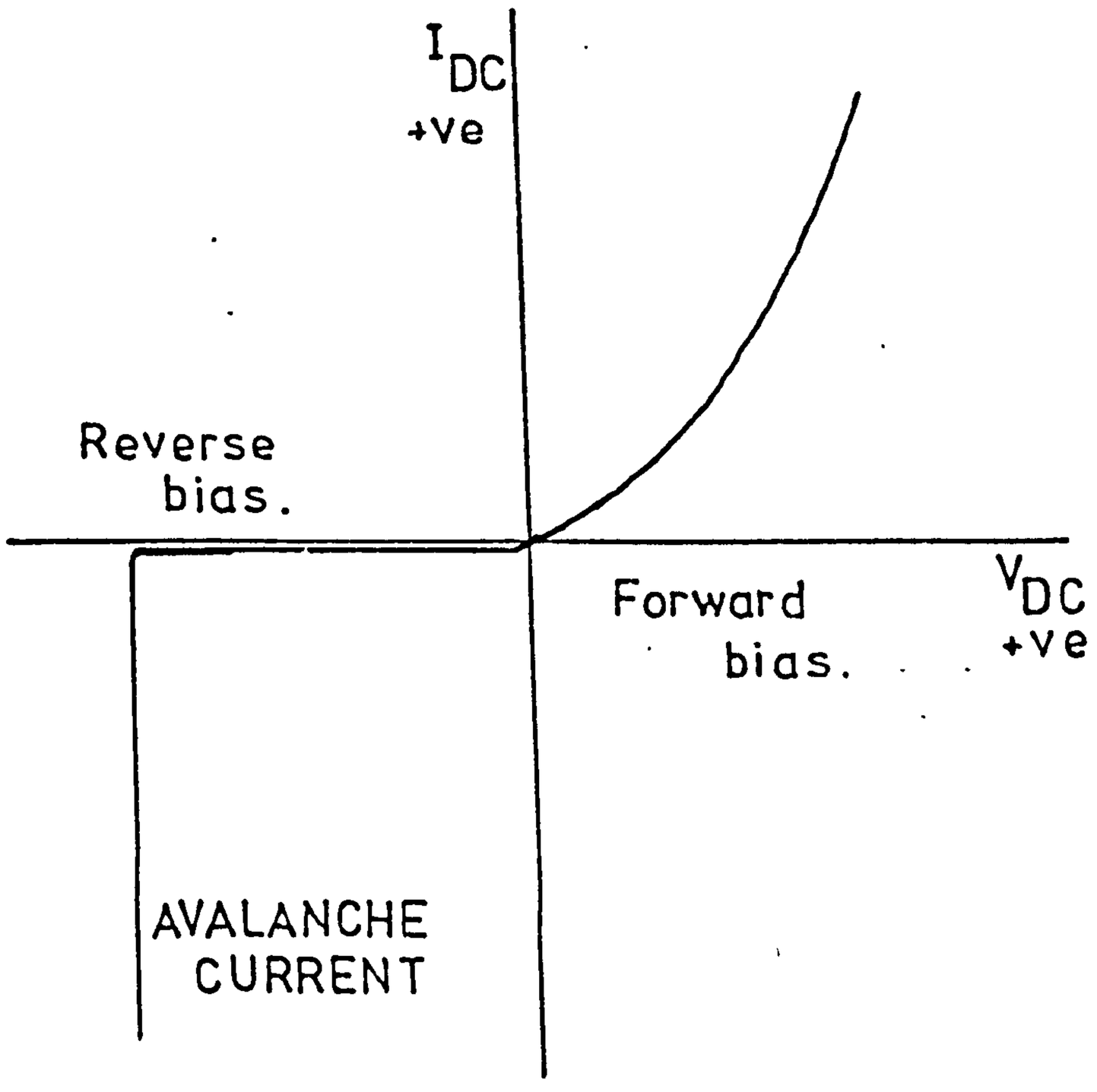

FIG. AB1. Schematic representation of the current - voltage characteristic of a typical p-n junction.

current flow result from small voltage changes. This region of the graph is known as The Avalance Breakdown Region, and it is under conditions of avalance current flow that an impatt diode is operated. Figure AB 2 shows, schematically, the situation existing in an operating impatt diode. The depletion layer at the junction formed upon the application of a reverse bias is a characteristic of all p-n junctions. If $|V_{applied}| < |V_b|$ then only the saturation current flows. This is represented on the diagram by the small number of minority carriers flowing from the cathode to the anode. Typically this current is of the order of 10 to 100 x 10^{-9} Amperes. As -Vapplied is increased the acceleration of these carriers is also increased until, at $|V_{applied}| = |V_b|$ a high probability exists of these carriers creating extra carriers in the avalanche layer by means of impact ionization. A large number of high mobility carriers (electrons) now flow into the drift zone. This situation corresponds to the avalanche region of Figure AB 1. It is now necessary to explain how this situation can lead to microwave oscillation. Suppose that, in addition to the DC bias voltage, an oscillating voltage of microwave frequency exists across the depletion layer of the diode. The total voltage is thus:

$$V_{(T)} = V_{DC} + V_o \sin wt$$

where V_o = amplitude of r.f. voltage.

w = angular frequency of r.f. voltage.

This voltage is represented in Figure AB 3 (a). Read (1958) showed that the non-linear nature of the avalance ionization process leads to a build-up of excess charge in the avalanche zone reaching a sharply-peaked maximum at the end of the positive half-cycle of the r.f voltage, $wt \simeq \pi$, Figure AB 3 (b). This charge lags the applied voltage by $\pi/2$. The resultant electrons drift across the drift zone to the anode at a constant velocity, V_e, under the influence of the DC field. The time taken for an individual electron to cross the

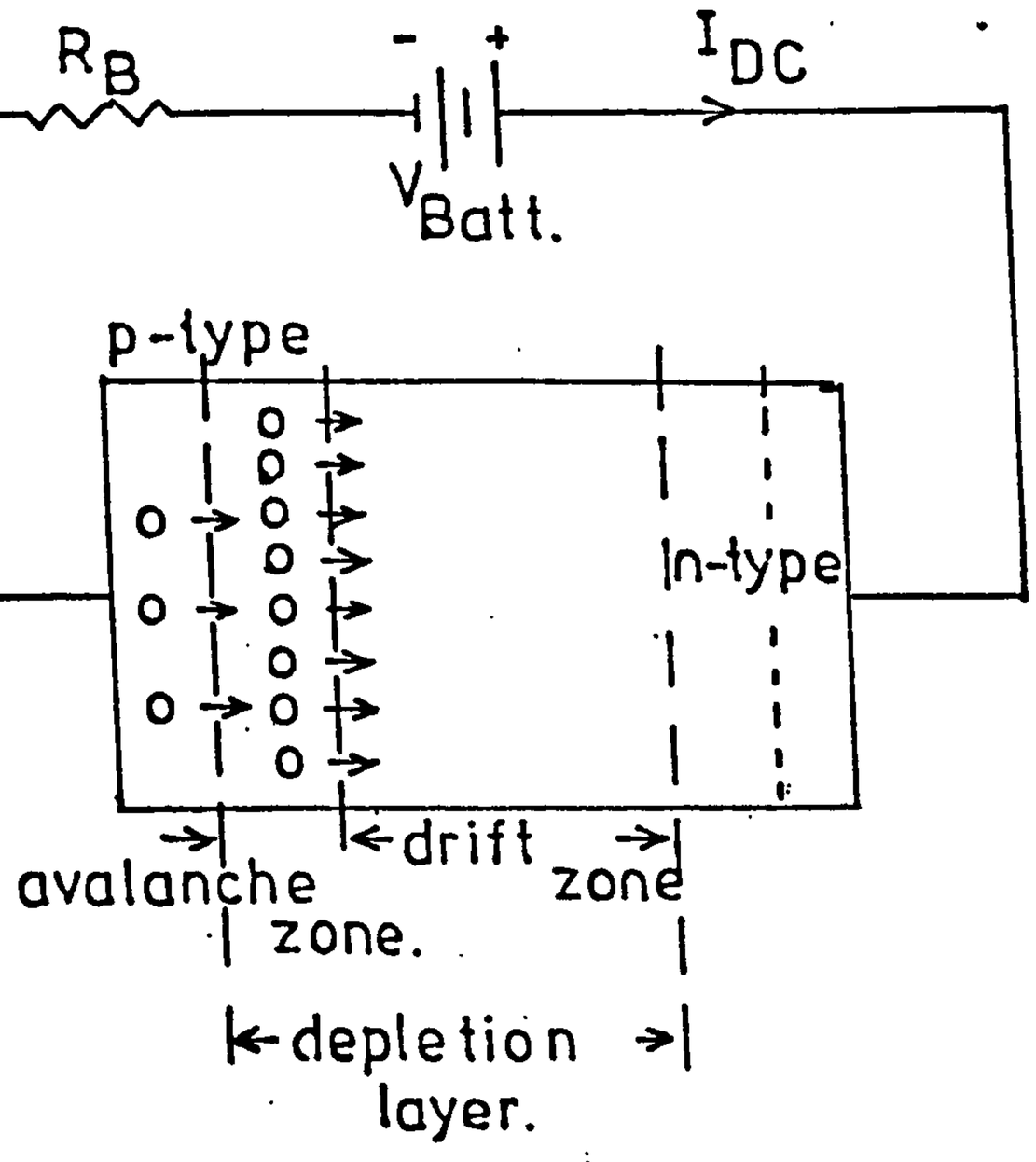

FIG.AB 2. Schematic representation of the situation in an operating IMPATT diode.

drift zone (known as the transit time, τ) is given by

$$\tau = \frac{W_o}{V_e}$$ where W_o is the width of the drift zone.

(Note that the much lower mobility positively charged carriers (or 'holes') are not considered in this argument).

The electron flow induces a current in the external circuit to which the diode is connected, which is of an approximate square-pulse form, Figure AB 3 (c). Comparison of Figures AB 3 (a) and (c) will show that a positive current is flowing in the external circuit during the negative half-cycle of the applied r.f. voltage. The junction appears to exhibit a negative resistance during this process. Maximum negative resistance occurs for w = 0.74 . The term w is referred to as the transit angle. In normal operation the expression = 0.74 is satisfied for a value of w near the centre of the desired operating frequency range. Figures AB 4 and (a) and (b) show the diode schematically as a negative resistance R_D (taking contact resistance and positive resistance of the undepleted part of the n-type region into account) and a capacitive reactance X_p. The external circuit is shown to consist of an inductive reactance X_L and a load resistance R_L. In most operational situations the impedance of the external circuit is provided by the diode package itself. Oscillator theory says that oscillation will occur if $Z_D = Z_L$, i.e. total diode impedance = total load impedance. Equating real parts, $R_D = -R_L$ and $X_D = -X_L$ (hence the inductive load reactance) In practice, the real part of the load impedance is less than R_D, and oscillations build up until $R_L = -R_D$, when the stable operating point is reached. The frequency of the oscillations is given by the expression

$$X_D = -X_L$$

$$\equiv (-)\frac{1}{wC} = (-)\ wL$$

The power delivered to the load under stable oscillating conditions is given by

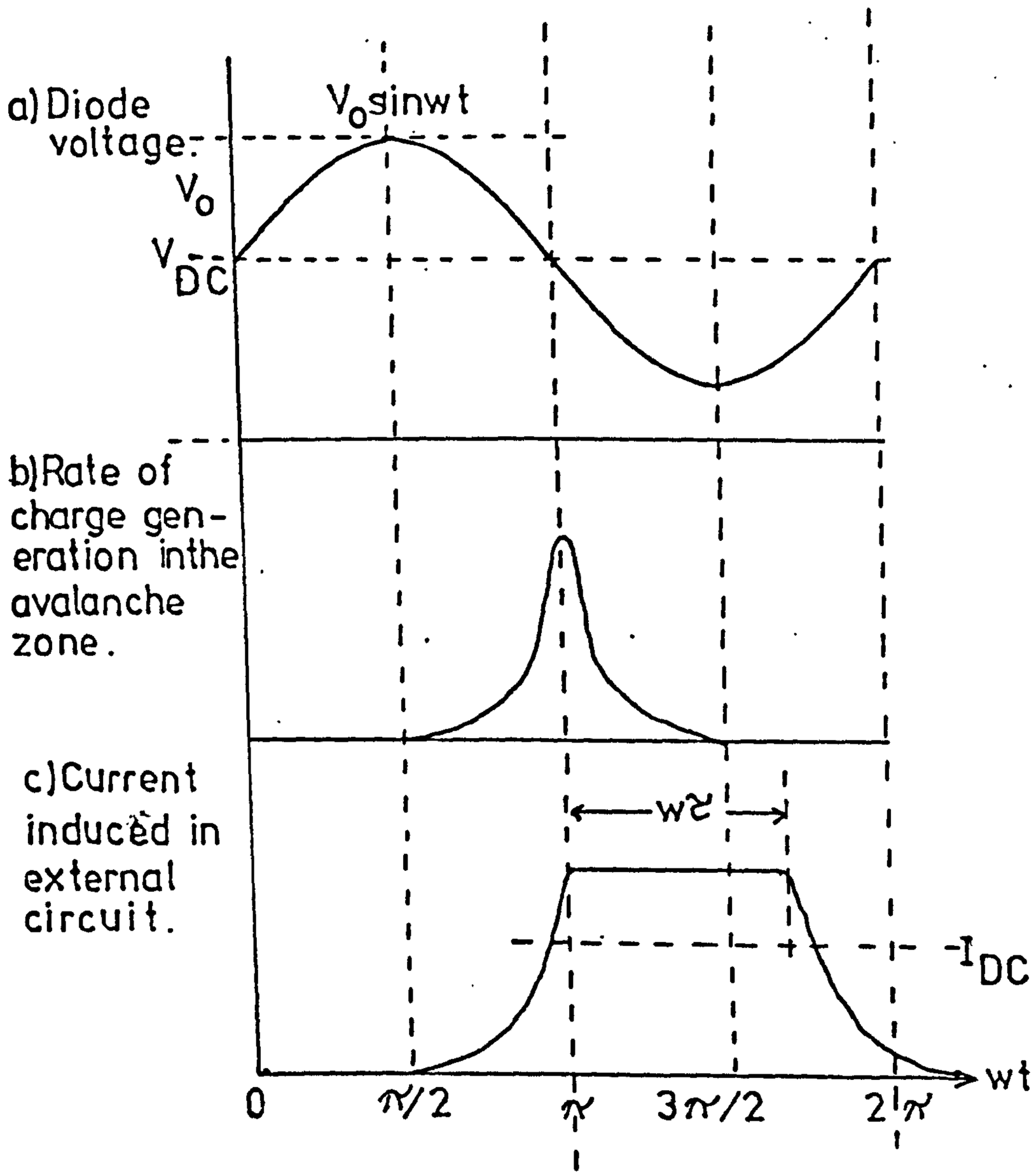

FIG AB.3. Electrical behaviour of the IMPATT diode.

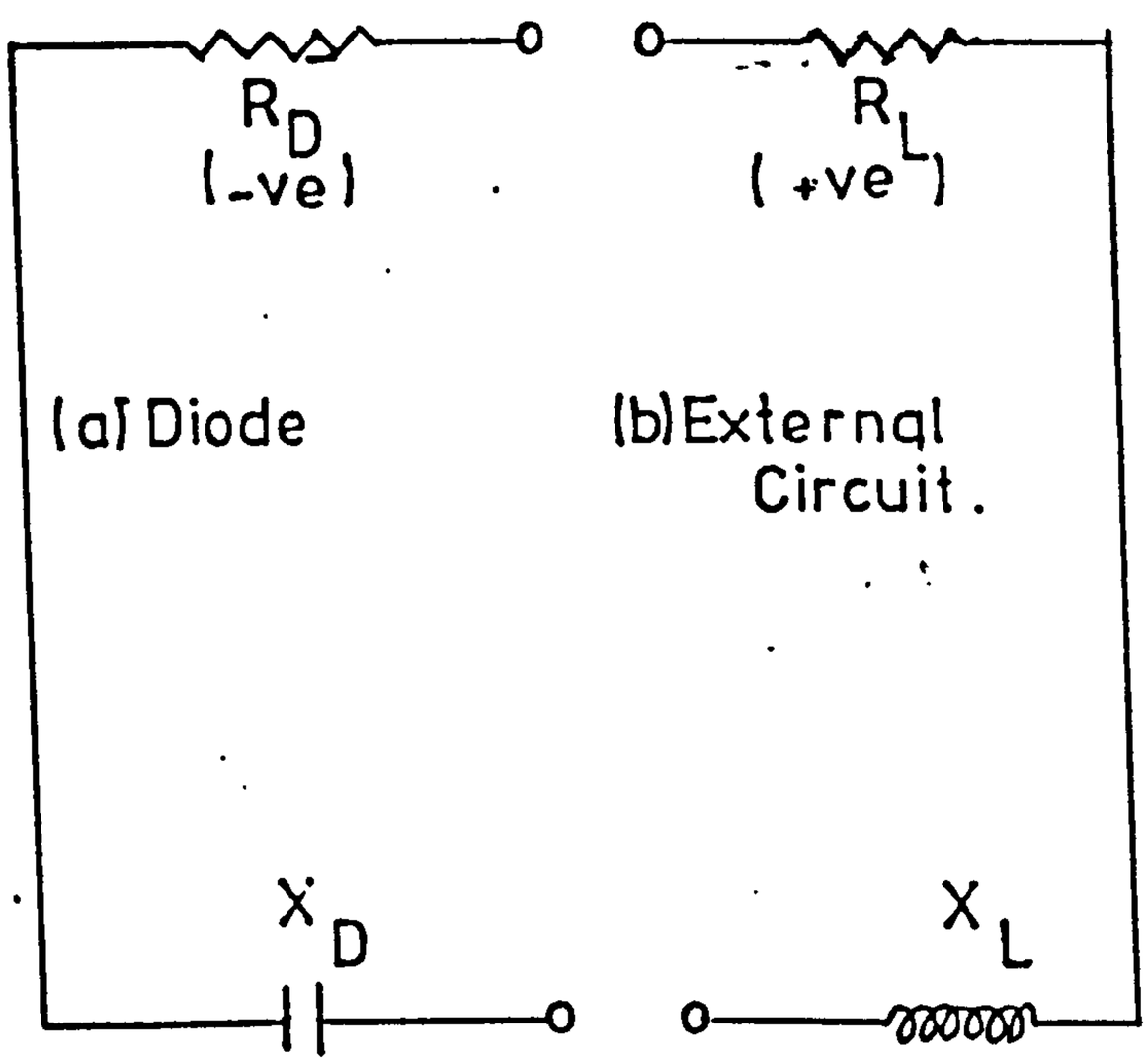

FIG A.B.4. Schematic representation of a diode as an oscillator and its external circuit.

$$P_o = \frac{1}{2} I_D^2 R_L$$

where I_D = current induced in external circuit by drifting carriers.

AB (iii) Biasing the Impatt Diode

(a) The Hewlett-Packard Pulse Amplifier and Bias Adder

According to the theory given above (AB (ii)), the voltage across an impatt diode is composed of a DC bias voltage and the (spontaneously started) r.f. voltage. If an impatt diode is to be used in pulse applications, however, Vx is not constant, but is varied in the shape of pulse to be required. For APR uses, a fast risetime pulse of duration $\sim$ 0.5 μs and pulse-repeat-frequency 1 KHz is required. The system applied to add a pulse to an impatt diode is to apply a steady DC voltage some volts below V_b for the particular diode, and then to add to this a pulse which acts as a 'switch', turning the oscillator on and off. Hewlett-Packard (Application note 961), give circuits and component valves for pulse amplifiers and DC adding circuits suitable for use in these circumstances. These circuits are given in Figures AB 5 and 6.

(b) Amplifiers Designed in the Department

Figure AB 7 shows the circuit of a fast risetime pulse amplifier designed and built for the impatt diode during the experiments. Rise-times of order 20 nS could be obtained for a 40 volt 1 μs pulse. These amplifiers were used in conjunction with the Hewlett-Packard bias adder circuit, and variable power supplies with a high degree of stabilisation were designed to provide the DC voltages.

AB (iv) Experiments on Impatt Diodes

It was not found possible to produce reliably working impatt-based generators, however, many experiments on the devices were made and the results are useful in indicating the direction of future investigation.

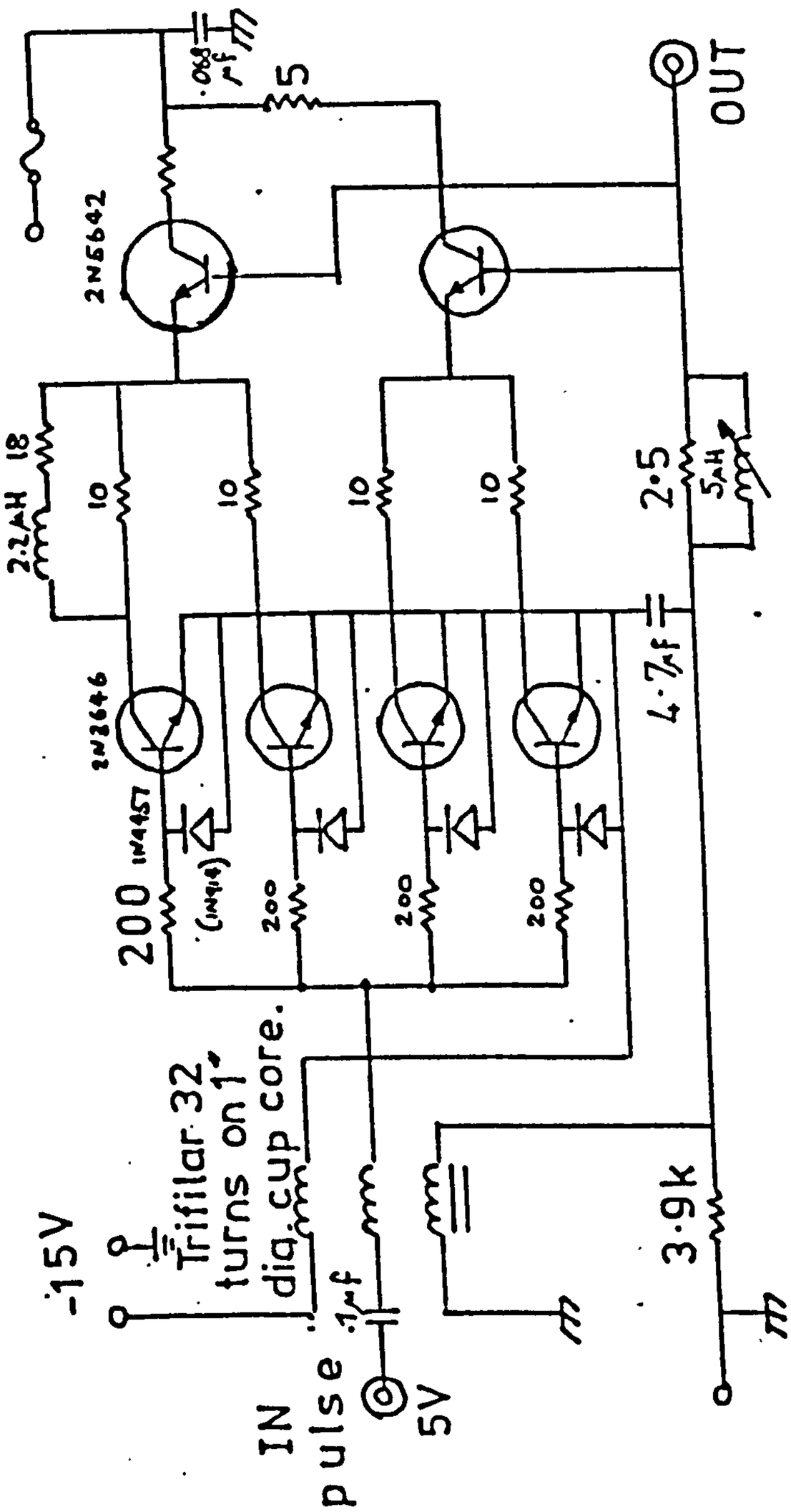

FIG. AB 5 Hewlett-Packard pulse amplier for use with IMPATT diode. (Components in brackets used where originals are unavailable.)

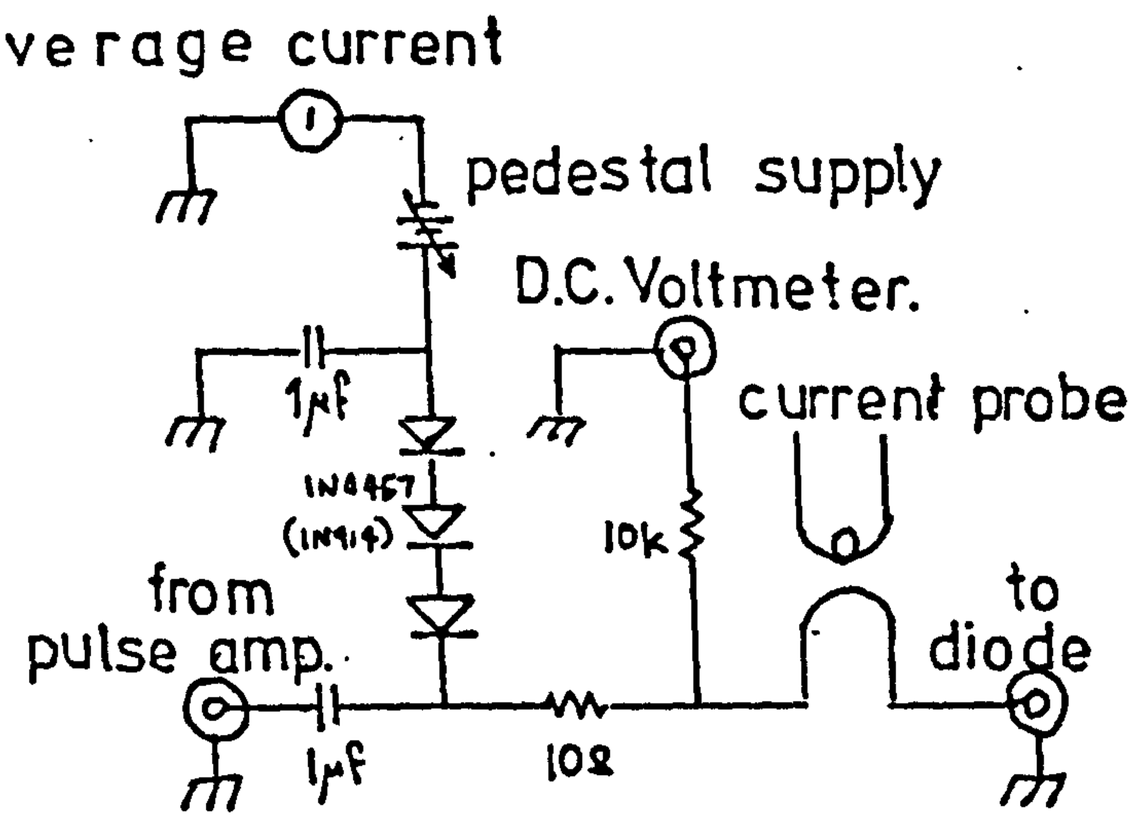

FIG.AB.6. D.C. and pulse bias adder circuit.

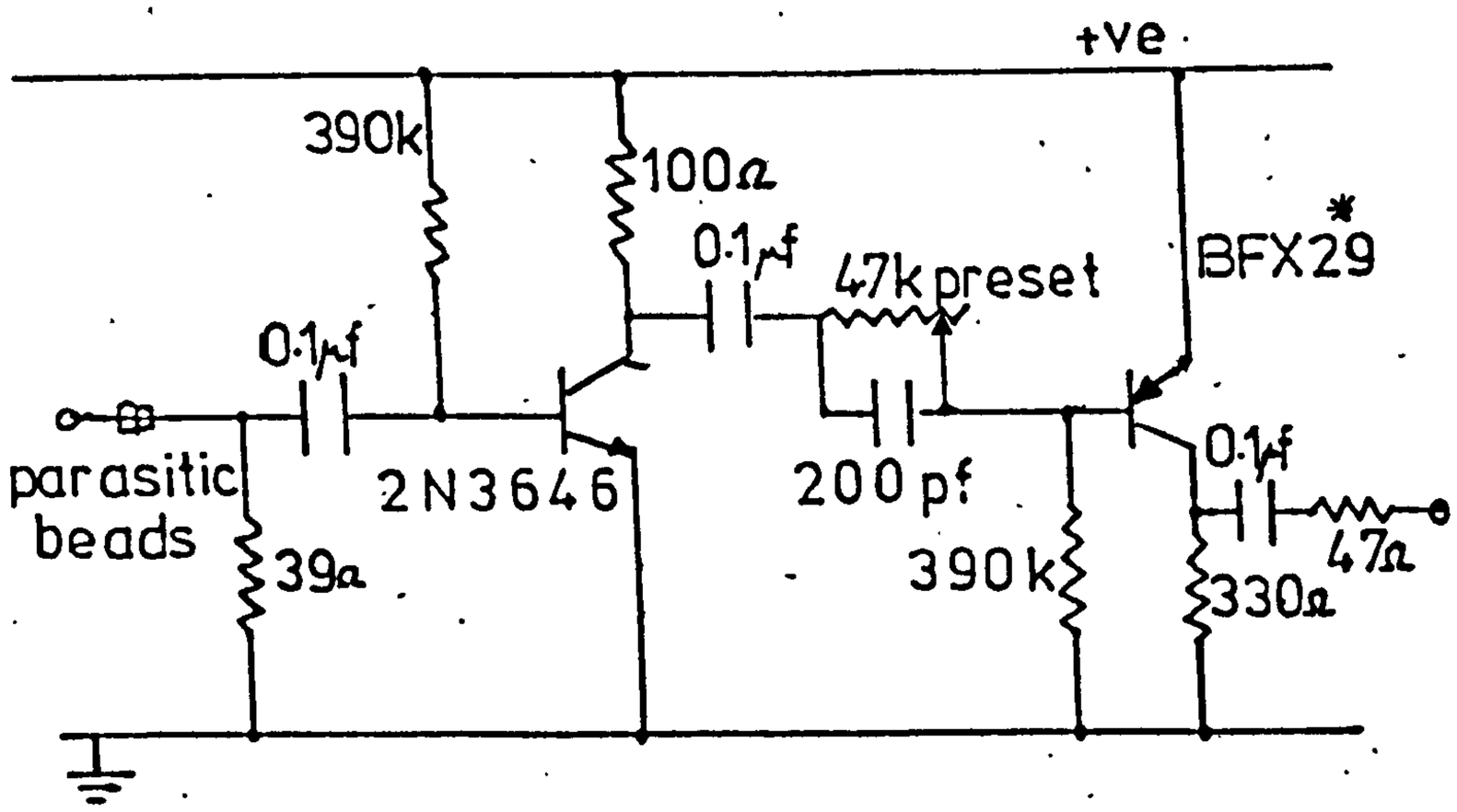

FIG AB 7. Pulse amplifier for IMPATT diode. (Designed during the experiments.)

* 2 off in parallel circuits for high-power diode.

(a) Construction of Pulse Amplifiers and Bias Adders

It was found that many of the components listed for the Hewlett-Packard fast-risetime pulse amplifier were not readily available in this country. Alternative components were selected from the characteristics of the unavailable parts and an alternative circuit constructed (The alternatives are listed on Figure AB 5). It was found that the pulses produced by the amplifier were of good shape and size into a high load, but deteriorated when presented with a loan of order 10 ohms, as a dummy of the active diode. Because of the complexity of the circuit design, especially of the pulse transformer system, it was decided to design a new amplifier for the application. Two such amplifiers were built, the design (Figure AB 7) being the same except for the larger number of output transistors used for the amplifier driving the high-power impatt diode. It was found that the pulses obtained from these amplifiers were good for loads down to 3 ohms.

(b) Testing of Impatt Diodes

The diodes were set up in a short waveguide test apparatus (Figure AB 8). Packages used were modified Gunn-diode waveguide packages supplied (in modified form) by Mid-Century Microwaves Ltd. Both low-power and high-power impatt diodes were tested using Hewlett-Packard bias adders, and the power supplies and pulse amplifiers designed in the laboratory. Pulses were supplied by a Lyons Type PG71 pulse generator. It was found that the low-power impatt diode functioned as expected, a reasonable pulse of microwave power of risetime comparable to that given by a magnetron being produced, which was tunable over the expected range of ~ 8 GHz to 11 GHz. It was noted that some improvements in pulse-shape could have been achieved and various combinations of DC bias and applied voltage pulse were tried until the best possible pulse shape was produced. The frequency spread of the microwaves in the pulse was tested by tuning a cavity wavemeter through the pulse. It was noted

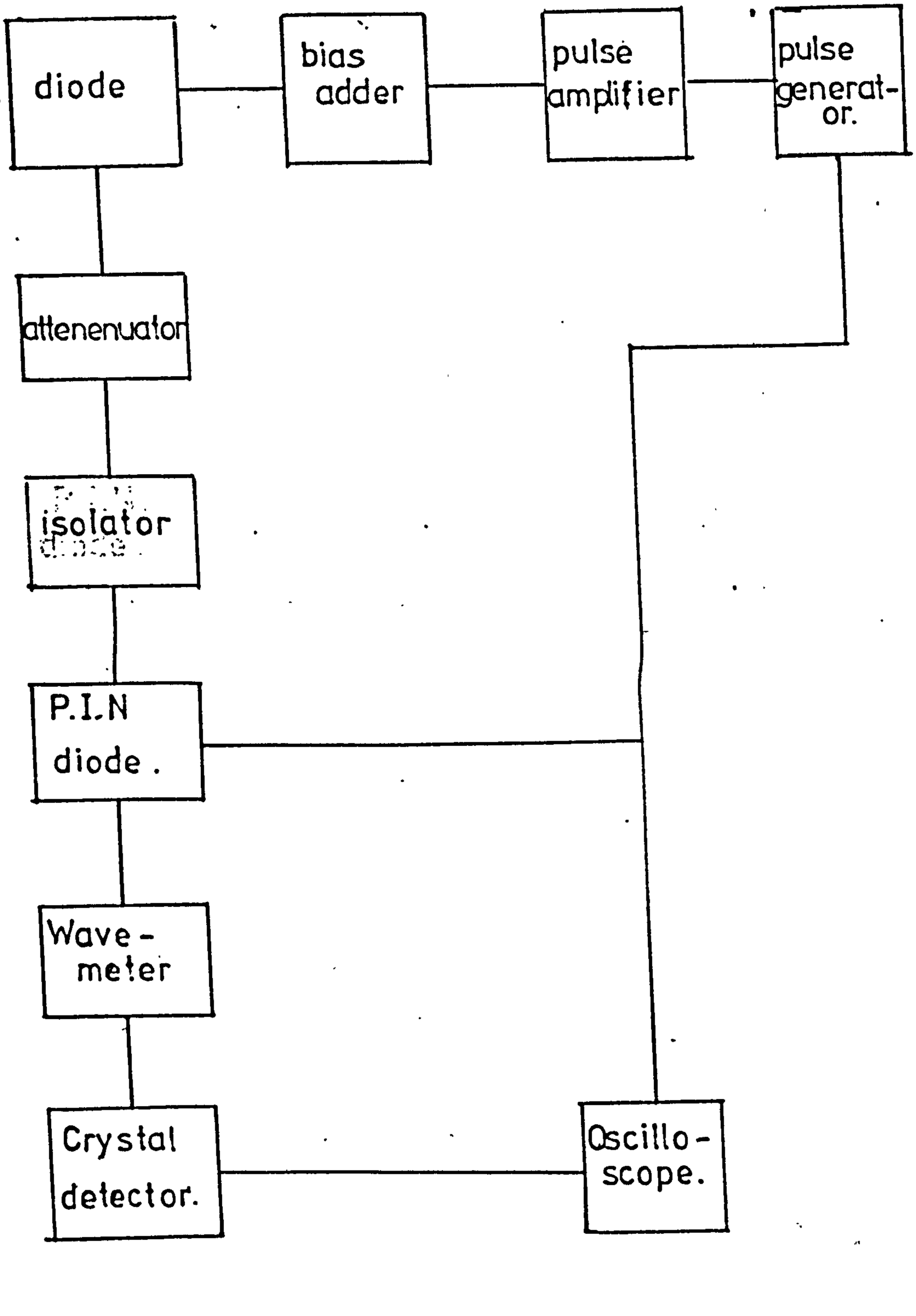

FIG AR 8 IMPATT diode test-bench (schematic).

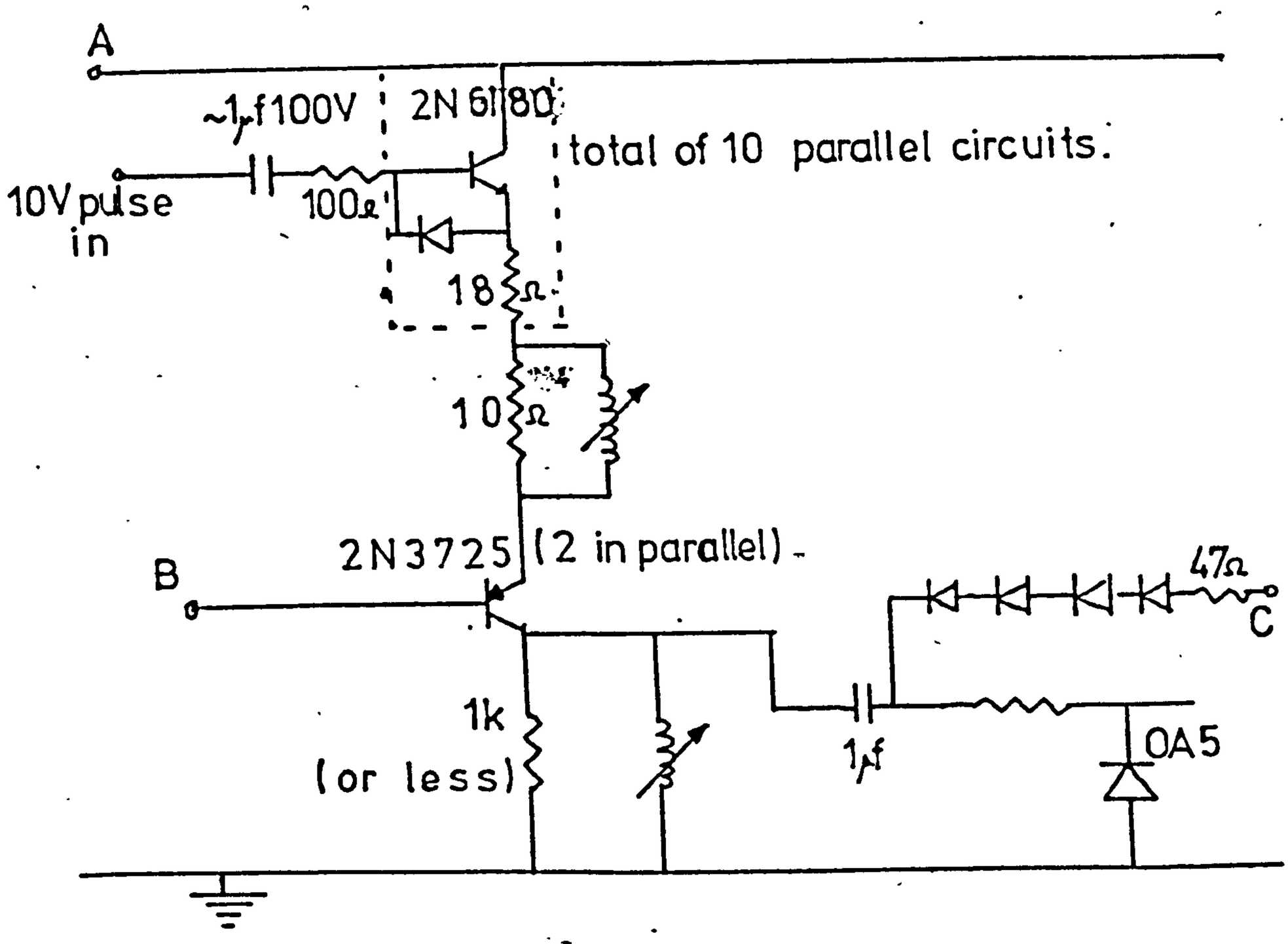

A 0 to 15V above B

B 0 to 80V

C DC bias
(diodes unspecified)

FIG AB 9 Suggested pulse amplifier for use with IMPATT diodes.

that frequency selectivity was better near the high end of the working frequency rnage. Tests on the high powered impatt-diode, however, proved unsuccessful. The diode produced a pulse of similar shape to that produced by the low-power diode, but of higher power, for a short period of time (∿ 30 minutes) and then burnt out.

(c) Conclusions from Experiments

Since no success had been achieved with this amplifier system, enquiries were amde about alternative designs. Dr P Braddock of RSRE, Malvern, Worcestershire, uses IMPATT diodes as oscillators and provided a circuit of Figure AB 9. This circuit was not testable at the time of writing. The apparent fault with the previous amplifier lay in the design of the output stage, which aimed at a square voltage pulse and a very low output impedance. Since the impatt-diode is an avalanche effect device, however, the effect impedance seen by the amplifier changes to a lower value as the device starts to work, and thus more current was drawn by the diode. It was concluded that this effect increased with time during the pulse, resulting in a current above the safe working current of the device being drawn, causing burnout. The Hewlett-Packard and RSRE designs take account of this effect by supplying a flat current pulse with a fairly high output impedance. The current supplied to the device is not dependent on the device impedance. The circuits also take account of an approximate rise in V_b of 1V per 10°C temperature rise of the device during operation, although it is believed that the 1 : 1000 duty cycle to be used in APR experiments is low enough for excess heating not to become a serious problem. A further reason for burnout may be poor hear sinking of the high-power device. The low-power screws into the cavity giving good heat sinking, whilst the high-power rest in only.

AB (v) General Conclusions

The functioning of the low-powered impatt-diode, even with the incorrectly designed pulser, was such that the possible advantages of a solid-state system discussed in section AB (i), were clearly demonstrated. Using suitably designed pulsers, and, possibly, further modified waveguide packages, it should be possible to acheive an APR spectrometer which has a far greater signal to noise ratio, much better pulse shape and wider frequency range than the magnetron-based system, as well as the advantage of the calibration pulse.

BIBLIOGRAPHY

Anderson B R, Challis L J, Stoelinga J H M and Wyder P, J. Phys C 7, 2234 (1974)

Anderson B R, Challis L J, Champion D J, Clark I A, Jay P R Woodhead S M, J. Phys C. 8, 1472, (1975)

Atkinson S M, M Phil Thesis, University of Nottingham. (1976)

Azaroff L, "Introduction to Solids" McGraw-Hill (1960)

Baranski K N, Soviet Phys, Doklady 2, 237 (1958)

Bates C A, Phys Rev, 35 (1978)

Bommel H E and Dransfeld K, Phys Rev. Letters 1, 234 (1958)

Bommel H E and Dransfeld K, Phys Rev. Letters 2, 298 and 3, 83 (1959)

Brabin-Smith, PhD Thesis, University of Nottingham (1969)

Challis L J, de Goer A M, Guckelsberger K, Slack G A, Proc Roy Soc A330, 29, (1972)

Challis, et al (1974), see Anderson et al

Fltecher, J R, J. Phys. C4. L156 (1971)

Fletcher J R and Stevens K W H, J. Phys C. 2, 444 (1969)

Ham F S Gen. Elec. (New York), Report No. 67-C-315 (1967)

Ham F S Phys. Rev. B, 4, 3854. (1971)

Hasan F I M, King P J, Murphy D T, Rampton V W, Jour. de Physique 39. C6-993 (1978)

Hewlett-Packard Components Application Note 961

Jacobsen E H, Phys. Rev. Letters 2, 249 (1959)

Jacobsen E H and Ilukor J "Physical Acoustics" (Ed Mason) V 221 Academic Press (1966)

Jones D A, Jones R V, Stevenson K W H, Conf. Cryst. Growth Supp. 1 (1967)

Kinder H, Proc 2nd Int Conf on Phonon Scattering in Solids, Plenum Press, 199 (1976)

King P J, Oates S G, Rampton V W, Shellard I J, Proc 2nd Int Conf on Phonon Scatt. in Solids, 187 (1976)

Landau L, and Lifshitz E, "Theory of Elasticity" Pergaman Press (1959)

Lange J, Phys. Rev. B (1976) Vol 14, N° 11, p 4791.

Marhsall F G, PhD Thesis, University of Nottingham (1967)

Marshall F G and Rampton V W, J. Phys C. 1 594 (1968)

Mason W P (Ed), "Physical Acoustics" IIIB, 43 (Anderson O L) Academic Press (1965)

Millet M R, IRE Trans. Microwave Theory and Tech. 56, 284 (1958)

Patel J L and Wigmore J K, J. Phys. C 10 1829 (1977)

Rampton V W. PhD Thesis, University of Nottingham. (1965)

Rampton V W, Bates C A, Fletcher J R, Jones S C and Jaussaud P C, Proc 1st Int Conf. Phonon Scatt. in Solids, [illegible] (1972)

Ringo C R, Fitzgerald J W, Hurdle B G, Phys Rev 72, 87 (1947)

Rivellin J and Salce B, Proc Zand Int Conf. Phonon Scatt. in Solids, 184 (1976) Plenmum Press

Rowell and Rampton. Phys Letters 7, 12 (1963)

Slater J C (1946) Patent listed in J. Acoust. Soc. Amer. 29, 758 (1957)

Sokolov C Ya, Uspekhi, Fiz. Nauk, 40, 3 (1950)

Stewart E S and Stewart J L, J. Acoust. Soc. Amer. 35, 913, (1963)

Tippell (translator) "Optical Workshop Principles". Dévé C. Hilger & Watts, (1954)

Weis O, Proc 2cnd Int Conf. Phonon Scatt. in Solids, 416 (1976)

Rampton V W and Shellard I J. Proc. 2cnd Int. Conf. on phonon scattering in solids. Plenum Press (1976) p. 178.